ISBN 978-82-326-1916-0 (printed ver.)
ISBN 978-82-326-1917-7 (electronic ver.)
ISSN 1503-8181

NTNU
Norwegian University of
Science and Technology

Doctoral theses at NTNU, 2016:289

Zhenwei Guo

Doctoral thesis

NTNU
Norwegian University of
Science and Technology
Thesis for the Degree of
Philosophiae Doctor
Faculty of Information Technology, Mathematics
and Electrical Engineering
Department of Electronics and
Telecommunications

Doctoral theses at NTNU, 2016:289

NTNU

Doctoral theses at NTNU, 2016:289

Zhenwei Guo

Subsurface resistivity estimation by seismic-guided inversion of marine controlled-source electromagnetic data

NTNU
Norwegian University of
Science and Technology

Zhenwei Guo

Subsurface resistivity estimation by seismic-guided inversion of marine controlled-source electromagnetic data

Thesis for the Degree of Philosophiae Doctor

Trondheim, November 2016

Norwegian University of Science and Technology
Faculty of Information Technology, Mathematics and Electrical Engineering
Department of Electronics and Telecommunications

NTNU
Norwegian University of
Science and Technology

NTNU
Norwegian University of Science and Technology

Thesis for the Degree of Philosophiae Doctor

Faculty of Information Technology, Mathematics and Electrical Engineering
Department of Electronics and Telecommunications

© Zhenwei Guo

ISBN 978-82-326-1916-0 (printed ver.)
ISBN 978-82-326-1917-7 (electronic ver.)
ISSN 1503-8181

IMT-report 2016:289

Doctoral theses at NTNU, 2016:289

Printed by NTNU Grafisk senter

Dedicated to

My beloved parents,

my wife Zhou Chonglang,

and daughter Guo Xiaoyu

青玉案·元夕

东风夜放花千树，更吹落，星如雨。

宝马雕车香满路。

凤箫声动，玉壶光转，一夜鱼龙舞。

蛾儿雪柳黄金缕，笑语盈盈暗香去。

众里寻他千百度，蓦然回首，

那人却在，灯火阑珊处。

Abstract

Marine controlled-source electromagnetic (CSEM) has been in commercial use for offshore hydrocarbon exploration for fifteen years. It is significant for geologists and geophysicists to design and interpret a marine EM survey for hydrocarbon exploration. SeaBed Logging (SBL) and towed streamer EM (TSEM) are the most popular data acquisition systems. They have their own advantages on acquisition. We compare the two different data acquisition systems by using 1D sensitivity modelling and 2D inline synthetic data inversion. In these studies, we test the effects of frequency, range, water depth, target dimensions and reservoir burial depth on the detectable capbility of the two acquisition systems. The relationship between the detectable hydrocarbon reservoir depth and water depth is discussed by anomalous transverse resistance (ATR) ratio, which is used to easily evaluate our inversion results. Moreover, the detectability is described for the two data acquisition systems in different water depth. Apparently, the SBL system has an advantage in deep water environment, but the TSEM has a similar sensitivity to the target with the SBL system in shallow water situation.

We develop an irregular sparse mesh to enhance both the speed and resolution of CSEM inversion by introducing structural geological information in the inversion algorithm. This sparse mesh is defined as a coherence-based irregular (IC) sparse mesh, which is based on vertices extracted from available geological information. Synthetic data inversion examples illustrate that the IC sparse mesh has a smaller inversion computational cost compared to the regular dense mesh. Additionally, the IC sparse mesh reduces the computational cost of the matrix operation for model updates. It also has a higher resolution than with a regular sparse mesh for the same number of estimated parameters.

Based on these IC sparse meshes, we propose an image-guided smoothing regularization method in the inversion of marine electromagnetic data. In order to enhance the resolution of marine EM inversion, incorporating seismic constraints into EM inversion is an effective approach. Compared to traditional regular dense mesh, a coherence-based irregular sparse mesh reduces computational cost. The image-guided regularization

represents an improvement of regularization and also uses the structure taken from a seismic image. In this thesis, we show that this regularization can improve the results of EM inversions with irregular sparse meshes. The image-guided regularized inversion can be applied to marine CSEM data and MT data, especially, it is able to be used for joint inversion of CSEM and MT data. Both synthetic and real data inversion examples presented in this thesis demonstrate that the proposed methods improve the quality of the resistivity image.

Acknowledgments

This thesis has been written in order to fulfill the requirements for the degree “Doctor of Philosophy” (PhD) at the Norwegian University of Science and Technology (NTNU). The work has costed over four years since 2011, at Department of Electrics and Telecommunications. And this work was financed by China Scholarship Council (CSC). The Statoil ASA provides the technique supports. I would like to express my gratitude to CSC and Statoil ASA.

Firstly, I would like to express my sincere gratitude to my supervisor Prof. Dong Hefeng for giving me the chance to study in Norway, and for the continuous support of my Ph.D study and related research, for her patience, motivation, and immense knowledge. Her guidance helped me in all the time of research and writing of this thesis. My co-supervisor, Åge Kristensen, introduced me to the Statoil Research Center. As my supervisor, he guided my scientific writing for both articles and thesis. He took much time on revising my manuscripts for publication on journal.

My sincere thanks also go to Dr. Odd Arve Solheim, Dr. Per Atle Olsen, Dr. Emmanuel Causse, and Dr. Anh Kiet Nguyen, who provided me an opportunity to join their team as intern, and who gave access to the laboratory and research facilities. Without their precious support it would not be possible to conduct this research. Especially, Dr. Emmanuel Causse taught me writing the first scientific article hand by hand. I am grateful to his guidance on both my research and writing. I also want to thank the geophysicists, Dr. Janniche Iren Nordskag and Dr. Torgeir Wiik, to give me advice and help on the research. All of these geophysicists are from Statoil Research Center in Trondheim.

I am grateful to Prof. Liu Jianxin from Central South University for guiding me on the opening the gate of Norway. I thank my friends Liu Haifei, Guo Rongwen, Mathias Lindkvist, Hu Xiangping and Liu Jiawei for the stimulating discussions on both my researches and scientific writing.

I also would like to thank the committee members Prof. Klaus Spitzer and Dr. Anwar Bhuiyan for reviewing my thesis, for their insightful comments and encouragement, but

also for the hard questions which incented me to widen my research from various perspectives.

Finally, I wish to thank the persons who mean most of all to me, my family. First of all, my wife Zhou Chonglang, who stayed patient with me through my Master's studies and my PhD. She has never lost faith in me, and when it was necessary reminded me that some things in like are more important than a PhD. Furthermore, she brought our angel, our daughter Guo Xiaoyu, to me. I would like to thank my parents, Guo Shutian and Zhang Xiaomei, for supporting me spiritually throughout writing this thesis and my life in general.

Guo Zhenwei

October 1st, 2016, Trondheim

Contents

Abstract I
Acknowledgments III
List of Figures VII
List of Tables XI
Chapter 1 Introduction 1
1.1. Marine Oil and Gas exploration and controlled-source electromagnetic method 1
1.1.1. Data acquisition 3
1.1.2. CSEM modelling and inversion 5
1.2. Outline of the thesis 9
Chapter 2 Theory of marine CSEM method 11
2.1. Marine CSEM 11
2.2. Rock physics 12
2.3. Maxwell's Equations 15
2.4. Forward problem 19
2.5. Inverse problem 23
Chapter 3 Comparison of marine CSEM data acquisition system 27
3.1. Introduction 27
3.2. Method 30
3.2.1. Sensitivity 30
3.2.2. Reservoir sensitivity index (RSI) 31
3.2.3. Occam's inversion 31
3.2.4. Transverse Resistance Ratio 32
3.3. Examples 33
3.4. Results of 1D sensitivity modelling 33
3.4.1. Case 1: Effect of frequency and offsets 35
3.4.2. Case 2: Effect of water depth 36
3.4.3. Case 3: Effect of reservoir burial depth 39
3.5. Results of 2D layers models 40
3.5.1. Case 4: Effect of water depth on RSI 42
3.5.2. Case 5: Effect of water depth on depth resolution 43
3.5.3. Case 6: Effect of reservoir depth on depth resolution 44
3.5.4. Case 7: Effect of target dimensions on sensitivity 45

3.5.5. Case 8: Effect of reservoir distance on horizontal resolution 47
3.6. Analysis of ATR ratio 48
3.6.1. ATR ratio with variation of water depth 48
3.6.2. ATR ratio with variation of reservoir depth 50
3.7. Discussion and Conclusion 52
Chapter 4 Seismic coherence driven sparse CSEM inversion 55
4.1. Introduction 55
4.2. Method 58
4.3. Synthetic marine CSEM survey examples 61
4.4. Discussion and Conclusion 74
Chapter 5 Image-guided regularized marine EM inversion 77
5.1. Introduction 77
5.2. Regularization inverse problem 80
5.3. Image-guided regularization inversion 81
5.3.1. The structure tensor fields and the metric tensor fields 81
5.3.2. Coherence-based sparse mesh 83
5.3.3. Image-guided regularization 83
5.4. Results 85
5.4.1. Case in normal regularization and normal mesh 86
5.4.2. Case in normal regularization and sparse mesh 89
5.4.3. Case in image-guided regularization and irregular mesh 93
5.4.4. Real data example 97
5.5. Discussion 100
5.6. Conclusion 101
Chapter 6 Conclusion 103
BIBLIOGRAPHY 107
Appendix: Publications during PhD study 115

List of Figures

Figure 1.1. *Typical in-line towing configuration of sources and receivers for the SBL system.* 4

Figure 1.2. *Acquisition geometry for the TSEM system surveys.* 5

Figure 2.1. *Schematic sketch of air-water-sediment geometry and receivers' layout on seabed during towing of electromagnetic source.* 11

Figure 2.2. *The geometry of CSEM dipole fields.* 12

Figure 2.3. *Resistivity varies over many orders of magnitude in Earth materials.(From course of Professor Ståle Emil Johansen at NTNU)* 13

Figure 2.4. *Resistivity log from a borehole illustrating contrasting resistivity in water bearing sediments and a hydrocarbon reservoir. (From course of Professor Ståle Emil Johansen at NTNU)* 13

Figure 2.5. *Reproduced from (Constable, 2010), seismic P-wave velocity and electrical resistivity of a porous (50%) sandstone as a function of gas saturation in the pore fluid.* 14

Figure 2.6. *A cartoon depicting the forward problem and inverse problem.* 23

Figure 3.1. *Typical in-line towing configuration of sources and receivers for the SBL system (top). Acquisition geometry for the TSEM system surveys (bottom).* 30

Figure 3.2. *Geometry of a thin resistive layer model for Case 1, Case 2 and Case 3...* 34

Figure 3.3. Sensitivities to resistive target are calculated by SBL system (a) and TSEM system (b). The frequency is 0.25 Hz. 34

Figure 3.4. *Sensitivity variation with frequency and offset for (a) SBL system and (b) Towed streamer system.* 36

Figure 3.5. *CSEM data anomalous field（solid line） and uncertainty （dashed line） varies in offsets with different water depth collected by SBL system (a) and TSEM (b).* 36

Figure 3.6. *CSEM data sensitivity variation with offsets and water depth collected by SBL system (a), (c) and TSEM (b), (d). Different curve illustrates sensitivity for different water depth. The frequency is 0.25 Hz in (a) and (b), and 0.75 Hz in (c) and (d).* 39

Figure 3.7. *The synthetic data measured by (a) SBL system and (b) TSEM system in different reservoir burial depths at 0.25 Hz.* 40

Figure 3.8. *The synthetic data measured by (a) SBL system and (b) TSEM system in different reservoir burial depths at 0.75 Hz.* 40

Figure 3.9. *Simple model with a thin resistive layer embedded in a conductive background medium.* 42

Figure 3.10. *RSI as a function of water depth for the two acquisition systems.* 43

Figure 3.11. *Inversion results of SBL system (left) and TSEM system (right) in various water depth.* 44

Figure 3.12. *Inversion results from SBL system (left) and TSEM system (right) for 300m water depth.* 45

Figure 3.13. *Inversion results from SBL (left) and TSEM (right) system.* 47

Figure 3.14. *A thin resistive layered model embedded in a conductive background medium for analyzing the horizontal resolution (Case 8).* 47

Figure 3.15. *Inversion results from SBL system (left) and TSEM system (right) for 300m water depth.* 48

Figure 3.16. *ATR ratio variation with water depth by (a) SBL system and (b) TSEM system for reservoir buiral depths.* 49

Figure 3.17. *ATR ratio variation with reservoir depth by SBL system (solid line) and TSEM system (dashed line) for water depth of 300 m (a), 500 m (b) 700 m (c) and 900 m (d).* 51

Figure 4.1. *(a) Seismic image extracted from seismic cube; (b) Seismic coherence extracted from coherence section.* 59

Figure 4.2. *Harris corner detection results on seismic gray image. Red star is the location of the nodes, which are sited as vertices of the triangles in the meshing generation. The nodes are detected from seismic coherence.* 59

Figure 4.3. *Coherence-based structured mesh generated by MARE2DEM code.* 60

Figure 4.4. True resistivity model for CSEM inversion test. The rectangle is the interesting area. White spots represent receivers' location. White triangles are the locations where the sources transmit electromagnetic waves. 62

Figure 4.5. *Building meshes of the starting model for Occam inversion by MARE2DEM. (a), RD mesh with 14600 cells. (b), RS mesh with 6700 cells. (c), IH mesh with 12900 cells. (d), IC mesh with 5900 cells.* 63

Figure 4.6. *CSEM inversion result by using (a) RD mesh, (b) RS mesh, (c) IH mesh, and (d) IC mesh. The final RMS is 1.22 for (a), (b) and (d) respectively, and 1.23 for (c). (e) True resistivity model for synthetic data.* 66

Figure 4.7. *RMS misfit variation with iterations using different meshes. Dashed lines for regular meshes and solid lines for irregular meshes.* 66

Figure 4.8. *The total time cost with CSEM data inversion iterations. Dashed lines for regular meshes and solid lines for irregular meshes.* 67

Figure 4.9. *The total time for (a) Jacobian calculation; (b) Model update; (c) forward modelling.* 68

Figure 4.10. *Main computational cost for the different meshes.* 69

Figure 4.11. *CSEM inversion result by using IC sparse mesh, but with a different number of parameters. All the final RMS misfit of inversion is approximately 1.22. IC*

mesh is generated starting from (a) 750 vertices, (b) 500 vertices and (c) 1000 vertices. 70

Figure 4.12. *The total time cost with CSEM data inversion iterations with the IC mesh 1000, 750, and 500.* 71

Figure 4.13. *CSEM inversion result by using (a) RD mesh, (b) RS mesh, (c) IH mesh, and (d) IC mesh. The final RMS is 1.14 for (b), 1.14 for (c), 1.15 for (d) and 1.14. (e) A true model of two reservoirs.* 73

Figure 4.14. *RMS misfit varies with iterations in two resistors model with the RD, RS, IH, and IC mesh.* 74

Figure 5.1. *Geometric interpretation of a structure tensor.* 82

Figure 5.2. *Seismic image (left), structure tensors field (middle), and metric tensors field (right). Red ellipses represent tensors.* 83

Figure 5.3. *Roughness calculated by (a) spatial distance; (b) non-Euclidean distance. "arrow" represents the non-Euclidean distance with the direction of the metric tensor (ellipse).* 84

Figure 5.4. *Reproduced from (Key, 2012b). The synthetic model consisting of sloping seafloor bathymetry, conductive sediments, and a thick tabular resistor representing a salt layer, a thin resistive hydrocarbon reservoir and an underlying resistive basement. The white dots are the receivers' locations with 1.32 km spacing.* 85

Figure 5.5. *(a). Fine regular dense mesh consists of 8500 free parameters for Occam's inversion. The results are the inversion of (b) CSEM data, (c) MT data and (d) joint inversion of CSEM and MT data.* 88

Figure 5.6. *The (a) rms misfit and (b) roughness with iterations for the inversion with regular dense mesh and smooth regularization.* 89

Figure 5.7. *(a). Regular sparse mesh for Occam's inversion. The results are the inversion of (b) CSEM data, (c) MT data and (d) joint inversion of CSEM and MT data.* 90

Figure 5.8. *The (a) rms misfit and (b) roughness with iterations for the inversion with regular sparse mesh and smooth regularization.* 91

Figure 5.9. *(a). Irregular sparse mesh for Occam's inversion. The results are the inversion of (b) CSEM data, (c) MT data and (d) joint inversion of CSEM and MT data.* 92

Figure 5.10. *The (a) rms misfit and (b) roughness with iterations for the inversion with irregular sparse mesh and smooth regularization.* 93

Figure 5.11. *(a). Irregular sparse mesh for image-guided regularized inversion. The results are the image-guided regularized inversion of (b) CSEM data, (c) MT data and (d) joint inversion of CSEM and MT data.* 95

Figure 5.12. *The (a) rms misfit and (b) roughness with iterations for the inversion with irregular sparse mesh and image-guided regularization.* 96

Figure 5.13. *(a) Irregular dense mesh for MT data inversion. The result of MT data inversion with (b) traditional regularization and (c) image-guided regularization.* 97

Figure 5.14. *Initial model for the 2008 Troll data set with the horizons. The triangles located on the sea floor indicate the receiver locations.* 98

Figure 5.15. *Inversion results using normal smooth regularization for the 2008 Troll data set. Triangles denote the receiver positions; white notes are the shots of transmitters. (a) Vertical resistivity, (b) Horizontal resistivity.* 99

Figure 5.16. *Inversion results using image-guided regularization for the 2008 Troll data set. Triangles denote the receiver positions; white notes are the shots of transmitters. (a) Vertical resistivity, (b) Horizontal resistivity.* 100

Figure 5.17. *(a) RMS misfit and (b) Roughness for the two different regularizations inversions.* 100

List of Tables

Table 2.1 Electromagnetic wave propagation in the 1 Ωm medium. 19
Table 2.2 Electromagnetic wave propagation in the 100 Ωm medium. 19
Table 3.1 Cases for sensitivity and resolution comparison. 33
Table 3.2 Model parameters of the CSEM acquisition systems 41
Table 4.1 Resistivity in test model 62
Table 4.2 Comparison of the different meshes 74
Table 5.1 Model parameters for the synthetic model. 85
Table 5.2 Cases for the different meshes and regularizations 86

Chapter 1 Introduction

1.1. Marine Oil and Gas exploration and controlled-source electromagnetic method

Marine oil and gas explorations were developed from land-based oil exploration. The whole development of marine oil and gas exploration is a process from simple to complex, from shallow water to deep water. In 1887, the offshore oil exploration opened in the coastal waters of California, where the first offshore exploration well was drilled in the shallow water (Mastrangelo, 2005).

In marine geophysical exploration, remote sensing techniques record variations in physical parameters for instance acoustic or electric properties. Although marine seismic sounding is the most common tools of hydrocarbon (HC) exploration, the marine electromagnetic (EM) methods has been developed rapidly in the last 15 years to overcome the limitations of seismic data in direct predication of pore fluid composition (Constable, 2010). To give the interpretation of a structural geometry which may fill porous sedimentary rocks with HC, the remaining uncertainty of seismic method mainly focus on whether the pore space is filled with saline water or HC. For this reason only 10-30% of exploration wells penetrate commercial oil or gas reserves in many areas (Johansen *et al*., 2005). Therefore, marine EM methods are dedicated as a valuable tool for offshore HC reservoir detection.

Several researches achieved by Baba (2005), Edwards (2005), Constable (2010) and Key (2012a) have reviewed the development of marine EM methods. The history of marine controlled-source electromagnetics (CSEM) sounding was closely linked to the history of the marine magnetotelluric (MT) method, for the similar techniques of studying seafloor resistivity by electric and magnetic fields. The first publication about the marine CSEM measurements was given by Bannister (1968), which presented seafloor-to-seafloor dipole-dipole measurements theory in frequency-domain to determine seabed resistivity. In the past, it was difficult to update the seafloor measurements from theory to practice. Until the late 1990s, Statoil researchers developed the use of the CSEM method for remote identification of hydrocarbons in a marine setting (Eidesmo *et al.,*

2005). In November 2000, the first practical demonstration of the technique was successfully completed by Statoil for a known shallow hydrocarbon reservoir offshore Angola (Eidesmo *et al.,* 2002; Ellingsrud *et al.,* 2002). The method was applied into the offshore hydrocarbon exploration for a few years (Constable, 2010). It is found that the HC explorations by the CSEM method was hampered due to the lack of statistically significant calibration data. Then new equipment was developed to open the way for improving acquisition, processing and interpretation of CSEM data, which was tested in 2003 by the Troll CSEM data collected by EMGS. These data were the first irrefutable evidence for direct detection of a deeply buried hydrocarbon accumulation by subsea CSEM sounding. The technique has later returned very good results when applied correctly in the prospecting work flow. These results have opened a new frontier in HC exploration.

The CSEM methods could employ electric or magnetic dipole transmitters. Chave (2009) discussed theoretical formulations for all electric and magnetic source geometries in HC exploration. The four fundamental source types of CSEM are the horizontal and vertical electric dipoles (HED and VED), the horizontal and vertical magnetic dipoles (HMD and VMD). The primary CSEM method for HC exploration uses a mobile horizontal electric dipole (HED) source and an array of seafloor electric field receivers. The transmitting dipole emits a low frequency electromagnetic signal that diffuses outwards into the overlying water column and downwards into the seabed. The array of sea floor receivers measures both the amplitude and the phase of the received signal that depends on the resistivity structure beneath the seabed. The detailed descriptions of marine CSEM are given by MacGregor and Sinha (2000), Edwards (2005), and Constable and Srnka (2007).

However, relatively high acquisition costs have represented a significant obstacle to widespread adoption of conventional CSEM technology, particularly in frontier basin and infrastructure-led exploration. Ziolkowski *et al*., (2010) presented field tests of a novel towed streamer approach where both the transmitters and a streamer array of receivers were towed by a ship, thereby allowing for continuous data coverage. The system has been developed and tested in the North Sea (Linfoot *et al.*, 2011a; Zhdanov, 2012). Although there are many successful case studies presenting the ability of CSEM

to detect HC reservoirs, marine CSEM method has not been completely accepted by the industry as an exploration tool. A successful case showed that towed EM data were suitable for characterization of the subsurface using resistivity in the Troll field, North Sea (Linfoot *et al.*, 2011a).

A method using stationary vertical electric transmitters has also been tested by industry, where the vertical current resulting from a vertical transmitter is sensitive to horizontal resistive layers (Holten *et al*., 2009a; 2009b). However, the merit of resolution over the conventional deep-towed horizontal transmitter and seafloor receivers were not readily apparent.

1.1.1. Data acquisition

In the hydrocarbon reservoir exploration, an HED source emits a low frequency (0.1-10 Hz) signal which is recorded by receivers or streamers. Low frequency EM signals decay exponentially with distance. The distance required to attenuate an EM signal by the factor e^{-1} (≈ 0.37) which is defined as the skin depth ($\approx 503\sqrt{\rho/f}$ (m)). The reason of detectable limitations in using CSEM is the diffusive nature of the electromagnetic field in conductive media. For the strong diffusive electromagnetic field in seawater, HED source is towed as close to the seafloor as possible to maximize the electromagnetic energy for transmitting into subsurface. However, the HED source close to surface offers an improved operational efficiency and a faster towing speed (Shantsev *et al.*, 2012). A streamer receivers offer a fast data collection approach and it is impossible to gather the large amount of data by SBL system. Besides, it is indispensable that uncertainties in the HED source and streamer receivers positioning are reduced since the equipment is at fixed depth and accurately measure their lateral position by GPS.

A typical CSEM survey is sketched in Figure 1.1, which is normally called Sea Bed Logging (SBL) data acquisition system. The model consists of an air half space, a sea water layer, a sediment layer, a thin resistive reservoir, a sandstone layer, and an underlying resistive basement. The resistivity of the sediment is larger than the sea water layer. The thin layer as a hydrocarbon reservoir is more resistive than the surrounding sand stone media.

In Figure 1.1, a vessel is towing a horizontal electric dipole source over the seafloor. In order to reduce the energy lost in sea water, the HED source should be towed close to the seafloor around 30 m. The transmitter injects a current of 1250 A in the seawater from a 270 m long horizontal electric dipole source, creating magnetic and electric fields that propagate diffusively into the seafloor. An array of seafloor electric field receivers is located at the sea floor to measure the signal.

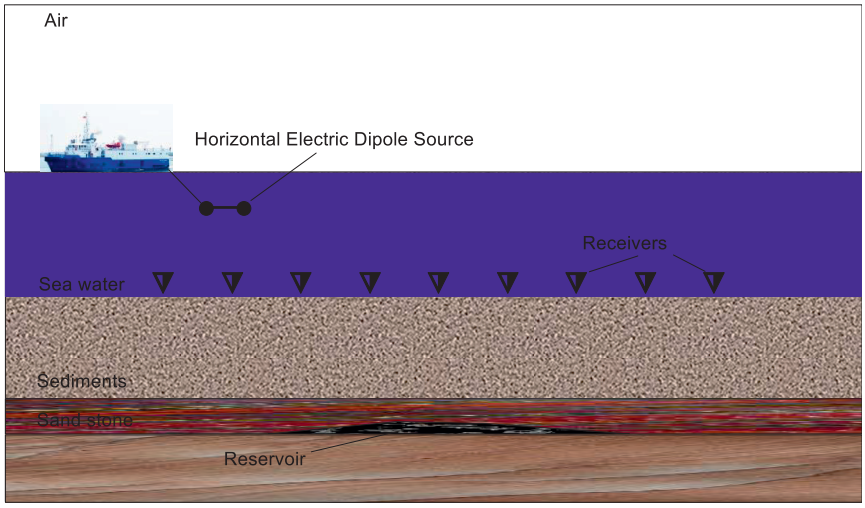

Figure 1.1.*Typical in-line towing configuration of sources and receivers for the SBL system.*

Comparing with SBL system, towed streamer electromagnetic (TSEM) system has a high efficient data acquisition. A TSEM survey is shown in Figure 1.2, where the same resistivity model is employed as Figure1.1. The vessel is towing not only the HED source but also a streamer with receivers. Normally, the inline HED source is towed at 10 m depth and the streamer cable at up to 100 m depth with the offsets usually between 500 m and 8000 m. The source bi-pole in this system is 800 m long with a signal current of 1500 A as normal (Folke *et al*., 2012). The HED source injects current into the water and the response of electric field is measured along the streamer. A hydrocarbon reservoir in the subsurface can result in an anomaly in the field which can be detected in the received data.

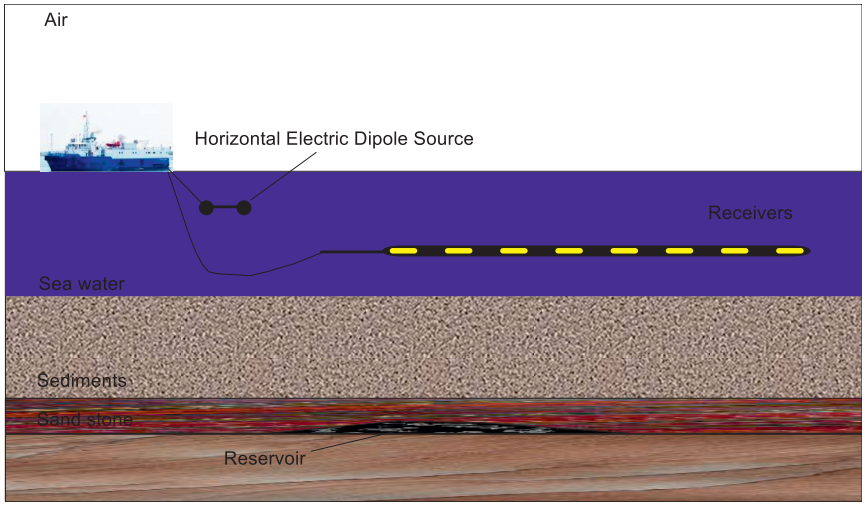

Figure 1.2. *Acquisition geometry for the TSEM system surveys.*

Some strongly resistive targets can be seen directly from the raw data, for instance, gas reservoir. Moreover, data processing, modelling and inversion methodologies are also applied to extract more information and determine resistivity and depth of sub-bottom structures.

1.1.2. CSEM modelling and inversion

In marine EM commercial investment, modelling and inversion techniques are necessary to provide more information for the marine CSEM interpretation. For 2D and 3D modelling, numerical techniques are applied by using the finite difference, finite element and integral equation methods.

Weiss and Constable (2006) introduced the concept of a control volume and computed the frequency-domain finite-volume solution to solve the governing curl-curl. Li and Key (2007) developed an adaptive finite-element algorithm for forward modelling of the frequency-domain, marine CSEM response of a 2D conductivity structure that is excited by a horizontal electric dipole source. For multisource and multi-frequency CSEM modelling, Plessix *et al*., (2007) discussed a practical approach which consists of an efficient iterative multigrid-based solver and an automatic gridding procedure. Abubakar *et al*., (2008) developed a forward algorithm based on a finite-difference approach in which a multifractal LU decomposition algorithm simulates

multisource experiments at nearly the cost of simulating one single-source experiment for each frequency of operation. Mittet (2010) used the corresponding principle for wave and diffusion fields to implement highly efficient finite-difference time-domain (FDTD) schemes to simulate marine CSEM data. Key and Ovall (2011) presented a parallel goal-oriented adaptive finite element method that can be used to rapidly compute highly accurate solutions for 2.5D controlled-source electromagnetic (CSEM) and 2D magnetotelluric (MT) modelling problems.

The purpose of the marine CSEM inverse problem is to find a resistivity model fit to the given dataset. Solving the electromagnetic inverse problem was well described by Parker (1980; 1994), and Zhdanov (2002). The geophysical inverse problem is a non-unique problem. Constable *et al.,* (1987) used Occam's inversion method to solve the regularized problem by searching for the smoothest model to fit the data. It was applied for 1D CSEM data inversion by Key (2009).

Gribenko and Zhdanov (2007) presented the results of the application of the preconditioned nonlinear conjugate-gradient inversion method to the interpretation of synthetic 3D MCSEM data. Commer and Newman (2008) also employed a nonlinear conjugate gradient algorithm for the inversion scheme, and enhance image by model parameter transformation functions.

2.5D and 3D inverse CSEM problems in frequency domain are successfully solved in many publications. Abubakar *et al*., (2008) has employed an inversion algorithm with a regularized Gauss-Newton minimization approach by a multiplicative cost function. The algorithm was equipped with two regularization cost functions that allow us to reconstruct either a smooth or sharp conductivity image. They also presented synthetic and field data inversion results for cross well and controlled-source EM measurements.

Bayesian inversion approaches which required a huge computational cost were applied on marine CSEM data by Ray and Key (2012). They parametrized simple model and characterized model uncertainty by the reversible jump Markov Chain Monte Carlo (RJ-MCMC) method for marine CSEM data.

Although it is possible to identify leads using just CSEM scanning surveys, some papers mainly focus on how the CSEM inversion can be reducing the risk profile of prospects by considering with others geophysical data. One of the earliest applications focused on joint inversion of marine CSEM and seismic data in order to improve estimates of reservoir properties (Hoversten *et al.*, 2006). Concerning joint inversion, the cross-gradient regularization joint inversion approach was defined and developed for geophysics by Gallardo and Meju (2003), and it was tested on marine CSEM data and seismic data by Hu *et al.* (2009).

It is expensive to invert both marine CSEM and seismic data by joint inversion methods. In order to combine the resolution of seismic data and the sensitivity of marine CSEM data, a standard CSEM inversion algorithm constrained by seismic structure was published by Brown *et al.,* (2012). Brown incorporated seismic constraints into EM inversion through the use of special regularization weight. The simple method utilized constraints EM inversion by using special regularization weights. However, CSEM data are not sensitive to all the normal layers if the difference of resistivity between the two layers is small.

In order to solve the ill-posed problem or to prevent overfitting problem of the CSEM inversion, regularization involving a process of introducing additional information is often used for EM inversion. A classic regularization example was the roughness penalty applied in Occam's inversion (Constable *et al*., 1987), in which the solution model varied to the smooth reference model. But in some cases, the preferred models were much sharper and more focused geological features than the traditional smooth models.

However, in image-guided interpolation, Hale (2009a; 2009b) provided a method to compute the tensor field and coherence from structure tensors of seismic image. This approach has only been applied for the full waveform inversion of seismic data (Ma *et al.,* 2012) in which the structural information was used to impose structural constraints in the inverse problem. In Ma *et al*., (2012), the size of model space was reduced by a gather-scatter process where the sparse space could be back to the model space by image-guided

interpolation per iteration. The key issue is how to effectively incorporate this high resolution seismic image into an EM inversion.

Zhou *et al*. (2014a; 2014b) inverted the electrical resistivity data by using image-guided Gauss-Newton inversion method. This approach extracted the structural information from the guiding image (GPR section) and incorporated to the direct current (DC) resistivity data. In Zhou *et al*. (2014a; 2014b), the structural information is assumed to be well-known. Stochastic image-guided structure-constrained inversion approach was developed by Zhou *et al.* (2016), in which the structural information could be updated by Markov-chain Monte Carlo (MCMC) sampler and the adaptive metropolis algorithm (AMA).

The marine CSEM modelling works have promoted the development of marine EM exploration. In this thesis, the research is focusing on the EM inversion which is based on the MARE2DEM code. A parallel goal-oriented adaptive finite element method is used to compute highly accurate solutions for the CSEM modelling by MARE2DEM (Key and Ovall, 2011). The forward modelling is significant to this research. However, it is not discussed in the thesis because my study is focusing on the inversion part.

We have proposed a coherence-based irregular sparse mesh for EM inversion which is based on the vertices and segments from seismic coherence (Guo *et al*., 2015; Guo *et al.*, 2016). The method consists of three major steps: (1) the seismic coherence section is created to detect the structured features of interest. (2) Extract corner nodes and horizons for triangle mesh generation. (3) Create irregular sparse meshes based on these nodes and segments by using MARE2DEM. The seismic coherence driven sparse mesh provides significant geological information for improving the marine CSEM inversion results and reduces the computational costs.

The metric tensors field of seismic image can be extract to build a new regularization for the CSEM inversion. The developed regularization approach is based on the coherence-guided irregular mesh. This regularization approach incorporates seismic constraints into EM inversion by using a non-Euclidean distance defined from the metric tensor field.

1.2. Outline of the thesis

In this section we briefly outline the work in each chapter contained in this thesis. The thesis consists of six chapters. In the following the chapters are introduced in more details, and each chapter emphasizes on different topics.

This chapter reviews the development of the marine CSEM methods including marine CSEM data acquisition systems, and both the forward and inverse problems.

Chapter 2: We introduce the theory of marine CSEM principle. Moreover, we present the rock physics theory. Based on the difference of resistivity between the water-bearing sediments and hydrocarbon-bearing reservoir, this difference of the resistivity makes the electromagnetic methods as powerful tools in the detection of the resistive anomaly. The electric and magnetic fields propagate following the Maxwell's Equations. The marine CSEM forward problem is derived from the Maxwell's Equation. The forward problem is solved by adaptive finite element method which is detailed by Key and Ovall (2011). The inverse problem is a mathematic problem to estimate the parameters of a system. In this chapter, we give brief overview of the Occam's inversion (Constable *et al.,* 1987; Key, 2009). Additionally, we develop a regularization algorithm to smooth the model following the geological features.

Chapter 3: We compare the two popular marine CSEM data acquisition systems (SBL and TSEM). In order to investigate the effects of frequency, offset, water depth, target dimensions and reservoir burial depth on the CSEM data, we test the sensitivity and resolution variation by studying synthetic data.

Chapter 4: We develop an irregular sparse mesh generation method. This sparse mesh is based on the vertices extracted from seismic coherence and the segments extracted from seismic image. So the sparse mesh is defined as coherence-based irregular mesh. Coherence-base irregular mesh has tiny triangles near the seafloor and other features; therefore, enough parameters are needed in order to describe the model. The size of triangle is large at the flat area. So the model has fewer parameters for CSEM inversion than fine regular mesh. This coherence-based irregular mesh reduces the computational cost and physics memory.

Chapter 5: We developed an approach for incorporating seismic constraints into EM inversion by using a non-Euclidean distance defined by a metric tensor field. The metric tensor field is computed from not only seismic image but also the geological structural image. By using these constraints, low depth and horizontal resolution of EM data can be improved. This image-guided regularization method smooths the model along the features. We perform complex models in both magnetotelluric (MT) and CSEM data which are inverted by Occam's inversion. This approach is an improvement of the irregular sparse mesh introduced in Chapter 4 to enhance the resolution of the EM inversion. The image-guided regularization method we proposed is an easy tool which can be used to the existing inversion methods.

Chapter 6: We summarize the results of the research work during the Ph.D. period.

Chapter 2 Theory of marine CSEM method

In this chapter, the theory of marine CSEM principle is introduced. Due to the difference of rocks properties, CSEM data have high sensitivity to resistive HC fluids embedded in saline pore fluids. Based on the Maxwell's equations, we induce the CSEM forward and inverse problem. We propose the image-guided regularized inversion method which is developed from Occam's inversion.

2.1. Marine CSEM

In hydrocarbon exploration, marine CSEM is also referred to Seabed Logging (SBL) (Ellingsrud *et al*., 2002). SBL method (Figure 2.1) was described as an application of marine CSEM sounding, which could detect and characterize hydrocarbon bearing reservoirs in deep water areas. In marine CSEM sounding a horizontal electrical dipole is towed close to the seabed emitting a low frequency (0.1-10 Hz) signal which is recorded by stationary seabed receivers (Figure 2.1). Seabed receivers measure the EM responses as a combination of energy pathways including signal transmission directly through seawater, reflection and refraction via the seawater-air interface, refraction and reflection along the seabed, and reflection and refraction via possible high resistivity subsurface layers (Løseth, 2007). Black arrows denote refracted transmission of electromagnetic signals via the air water interface. Green arrows denote direct transmission of electromagnetic signals through water and by refraction along the seabed. Red arrows denote guided transmission of electromagnetic signals via a buried high-resistivity layer (hydrocarbon reservoir).

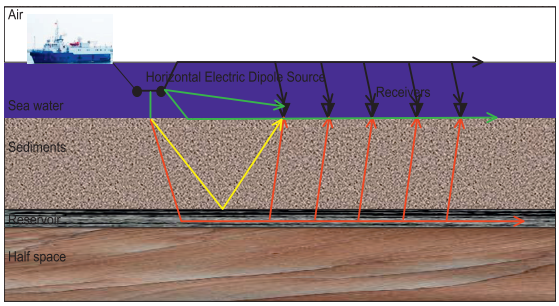

Figure 2.1. *Schematic sketch of air-water-sediment geometry and receivers' layout on seabed during towing of electromagnetic source.*

The CSEM sources include the horizontal electric dipole (HED), vertical electric dipole (VED), horizontal magnetic dipole (HMD) and vertical magnetic dipole (VMD). The transmitter azimuth is the angle of the dipole measured clockwise from the 2D strike direction x. Thus, typical inline electric dipole CSEM data have a transmitter azimuth of about 90° (or 270°), while broadside data have a transmitter azimuth of 0° (or 180°). The geometry of CSEM dipole fields is shown in Figure 2.2. Along the polar axis of the dipole transmitter, the field is purely radial. Along the equatorial axis, the field is purely azimuthal. At other azimuths the received fields are a trigonometric mix of both modes (Constable and Weiss, 2006).In this thesis, we are focusing on the inline CSEM data.

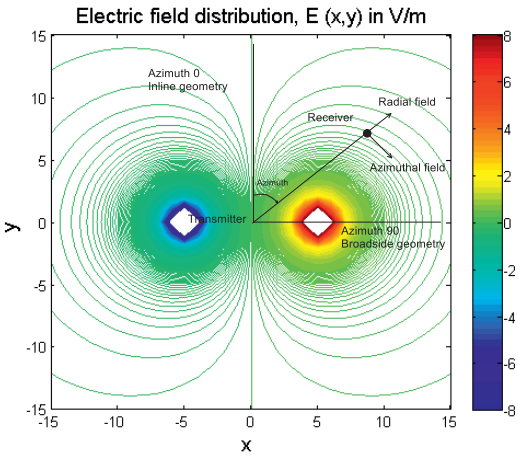

Figure 2.2. *The geometry of CSEM dipole fields.*

2.2. Rock physics

The electrical resistivity of Earth's materials varies over many orders of magnitude. It depends upon many factors including rock type, porosity, connectivity of pores, and permeability of the rocks, the pore fluid conductivity, and metallic content of the solid matrix. The resistivity of reservoir rock is largely dependent on its porosity and the resistivity of the fluid in the pore space. Figure 2.3 shows some materials resistivity on the earth.

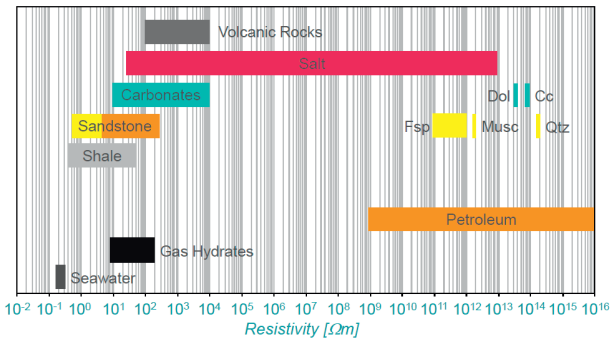

Figure 2.3. *Resistivity varies over many orders of magnitude in Earth materials.(From course of Professor Ståle Emil Johansen at NTNU)*

The electrical properties of rocks are required to interpret the electric field data measured at the earth's surface. The water-bearing sediments are typically a few Ωm; the hydrocarbon reservoirs have much high resistivity of a few tens of Ωm or higher. Figure 2.4 illustrates contrasting resistivity in water bearing sediments and a hydrocarbon reservoir. The resistivity of seawater, usually around 0.3 Ωm, is indicated in the upper part of the log curve. This difference of resistivity between the water-bearing sediments and hydrocarbon-bearing reservoir makes the electromagnetic methods powerful tools in the detection of the resistive anomaly.

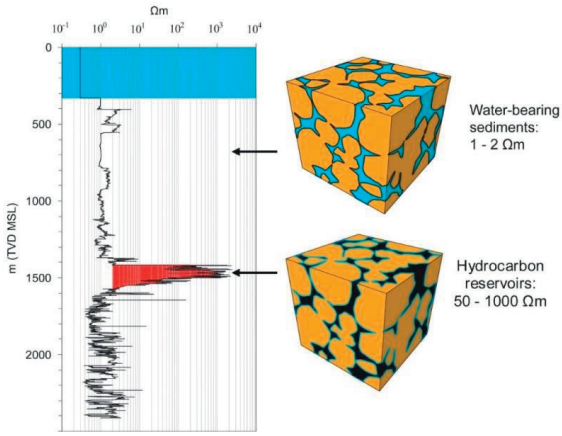

Figure 2.4. *Resistivity log from a borehole illustrating contrasting resistivity in water bearing sediments and a hydrocarbon reservoir. (From course of Professor Ståle Emil Johansen at NTNU).*

For the lack of sufficient information on pore microstructure, an empirical law is proposed by Gus Archie of Shell Oil (1942). In terms of the brine saturated formation resistivity and hydrocarbon saturation, the true resistivity is calculated by:

$$\rho_t = \frac{\rho_0}{(1-S_{HC})^n}, \tag{2.1}$$

where ρ_t is the true resistivity; ρ_0 is brine saturated formation resistivity; S_{HC} is hydrocarbon saturation. Typically $n=2$ is used when no log or core calibration is available. The electrical resistivity of reservoir rocks has a high sensitivity with hydrocarbon saturation. Electrical resistivity of a porous sandstone as a function of gas saturation in the pore fluid increasing for high gas saturation. The risk can be reduced by combining CSEM with seismic exploration.

The resistivity of the reservoir is primarily controlled by the rock porosity, saturation, water, oil, gas, and other fluids in the rock are crucial factor information (Jean-Louis et al., 1996).

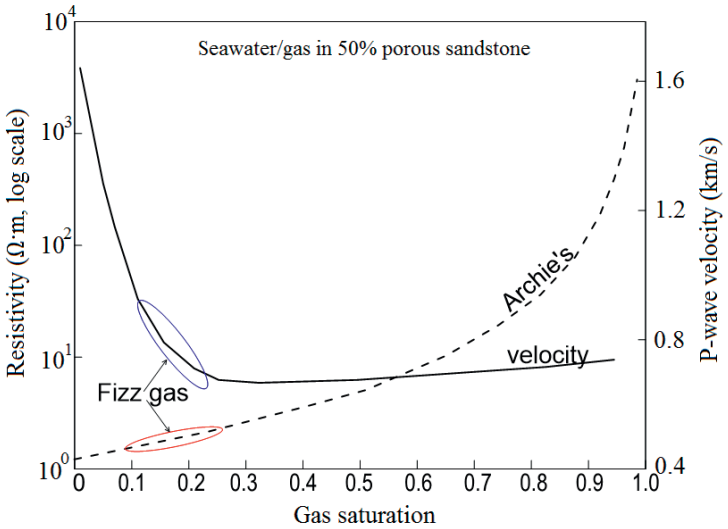

Figure 2.5. *Reproduced from (Constable, 2010), seismic P-wave velocity and electrical resistivity of a porous (50%) sandstone as a function of gas saturation in the pore fluid.*

2.3. Maxwell's Equations

The world of electromagnetic can be described by a set of complicated equations, Maxwell's Equations. These equations describe how electric and magnetic fields propagate and interact, and how they are influenced by objects. Maxwell's Equations interpret four electromagnetic phenomena: Gauss's law for electric fields, Gauss's law for magnetic fields, Faraday's Law and Ampere-Maxwell Law. The Maxwell's Equations are written in differential form as:

$$\nabla \cdot \vec{D} = q \,, \tag{2.2}$$

$$\nabla \cdot \vec{B} = 0 \,, \tag{2.3}$$

$$\nabla \times \vec{E} = -\partial_t \vec{B} \,, \tag{2.4}$$

$$\nabla \times \vec{H} = \vec{J} \,, \tag{2.5}$$

where $\vec{D}$ is electric displacement; $\vec{B}$ is magnetic induction; $\vec{E}$ is electric field; $\vec{H}$ is magnetic field; $\vec{J}$ is current density; q is electric charge density; t is time.

Linear material equations are given as follows:

$$\vec{D} = \varepsilon \vec{E} \,, \tag{2.6}$$

$$\vec{B} = \mu \vec{H} \,, \tag{2.7}$$

$$\vec{J} = \varepsilon \partial_t \vec{E} + \sigma \vec{E} + J^{source} \,, \tag{2.8}$$

where ε is electric permittivity in *F/m*; μ is magnetic permeability in *H/m*; σ is conductivity in *S/m*. The other normal material property is resistivity ρ in Ωm, which is the reciprocal of conductivity. In the isotropic media, ε and μ are scalars; however, they are tensors of rank 2 in the anisotropic media.

The Maxwell's Equations can be simplified as Faraday's law and Ampere's law. The simplifications can be shown as follows:

$$\nabla \times \vec{E} = -\mu_0 \partial_t \vec{H} \,, \tag{2.9}$$

$$\nabla \times \vec{H} = \varepsilon \partial_t \vec{E} + \sigma \vec{E} + J^{source} \,. \tag{2.10}$$

The two constants are the electric permittivity of free space ε_0 and the magnetic permeability of free space μ_0.

$$\varepsilon_0 = 8.854187817 \times 10^{12} F/m \approx 8.85 \times 10^{12} F/m \text{ , } (2.11)$$

$$\mu_0 = 4\pi \times 10^{-7} H/m \text{ .} \quad (2.12)$$

With the given magnetic permeability and electric permittivity values given, the speed of light c can be calculated by:

$$\mathrm{c} = \frac{1}{\sqrt{\mu_0 \varepsilon_0}} = 2.998 \times 10^8 m/s \text{ .} \quad (2.13)$$

By Fourier transform, the Faraday's law and Ampere's law in frequency domain can be represented as:

$$\nabla \times \vec{E} = i\omega\mu_0 \vec{H} \text{ ,} \quad (2.14)$$

$$\nabla \times \vec{H} = -i\omega\varepsilon_r\varepsilon_0 \vec{E} + \sigma\vec{E} + J^{source} \text{ ,} \quad (2.15)$$

where ω is the angular frequency of the field; ε_r is the relative electric permittivity.

Compared with σ, $\omega\varepsilon_r\varepsilon_0$ is the displacement term, which dominates at high frequencies in a nonconductive medium. σ is the conduction term which dominates at low frequencies in a conductive medium. The equations are applied in Ground penetrating radar (GPR) sounding when the frequencies are high in the range of 10 MHz to 1 GHz.

Now we consider the problem of wave propagation in the quasi-static limit, which is described by Zonge and Hughes (1991). In the CSEM exploration, the sedimentary rocks can be considered as non-magnetic medium, where $\vec{\mu}$ equals μ_0. The seawater electric permittivity ε_{sea} is 80 *F/m; and* ε_r for sedimentary rocks is smaller than 80 *F/m*. When the frequency f is 1 *Hz*, $\omega\varepsilon_r\varepsilon_0$ is 4.4×10^{-9} *S/m* which is much less than the seawater conductive σ (3.2 *S/m*). So it is reasonable to neglect the displacement current for CSEM frequency band.

$$\nabla \times \vec{E} = i\omega\mu_0 \vec{H} \text{ ,} \quad (2.16)$$

$$\nabla \times \vec{H} = \sigma\vec{E} + J^{source} \text{ .} \quad (2.17)$$

In these low frequencies and conductive medium, the Maxwell's equations can be put in a diffusive system. The typical diffusive system has very strong absorption and dispersion. So the electromagnetic energy is lost during the diffusion and the different frequencies electromagnetic waves propagate with different velocities.

Concerning 1D solution in frequency domain, we assume earth invariant in *x* and *y* directions. We also assume source invariant in *x* and *y* directions, and no vertical current. As a consequence, electric and magnetic fields are invariant in *x* and *y* directions.

$$\begin{bmatrix} J_x^s + \sigma E_x \\ J_y^s + \sigma E_y \\ 0 + \sigma E_z \end{bmatrix} = \begin{bmatrix} \overrightarrow{e_x} & \overrightarrow{e_y} & \overrightarrow{e_z} \\ \partial_x & \partial_y & \partial_z \\ H_x & H_y & H_z \end{bmatrix} = \begin{bmatrix} \partial_y H_z - \partial_z H_y \\ \partial_z H_x - \partial_x H_z \\ \partial_x H_y - \partial_y H_x \end{bmatrix} = \begin{bmatrix} -\partial_z H_y \\ \partial_z H_x \\ 0 \end{bmatrix}, \quad (2.18)$$

$$\begin{bmatrix} i\omega\mu_0 H_x \\ i\omega\mu_0 H_y \\ i\omega\mu_0 H_z \end{bmatrix} = \begin{bmatrix} -\partial_z E_y \\ \partial_z E_x \\ 0 \end{bmatrix}. \quad (2.19)$$

Combine two sets of the equations that describe two different polarizations:

$$\begin{cases} \partial_z H_y + \sigma E_x = -J_x^s \\ \partial_z E_x - i\omega\mu_0 H_y = 0 \end{cases}, \quad (2.20)$$

$$\begin{cases} \partial_z H_x + \sigma E_y = -J_y^s \\ \partial_z E_y + i\omega\mu_0 H_x = 0 \end{cases}. \quad (2.21)$$

Equations for both polarizations:

$$\partial_z^2 E_x + i\omega\mu_0\sigma E_x = -i\omega\mu_0 J_x^s, \quad (2.22)$$

$$\partial_z^2 E_y + i\omega\mu_0\sigma E_y = -i\omega\mu_0 J_y^s. \quad (2.23)$$

It is sufficient to concentrate on x-polarization to understand the physics. We assume a function without any current sources,

$$\partial_z^2 E_x + i\omega\mu_0\sigma E_x = 0. \quad (2.24)$$

The propagation constant or wave number k_ω is defined as:

$$k_\omega^2 = i\omega\mu_0\sigma. \quad (2.25)$$

The Equation (2.24) can be rewritten as:

$$\partial_z^2 E_x + k_\omega^2 E_x = 0. \tag{2.26}$$

For the horizontal electric field component Ex, the general form of solutions along z axis can be represented as:

$$E_x = Ae^{ik_\omega z} + Be^{-ik_\omega z}. \tag{2.27}$$

The factors A and B are determined by the source(s) and reflection/transmission properties of the medium. The propagation constant can be written in complex form as:

$$k_\omega = \sqrt{i\omega\mu_0\sigma} = (1+i)\sqrt{\frac{\omega\mu_0\sigma}{2}}. \tag{2.28}$$

The phase and attenuation constants are given as $\omega/c(\omega)$ and $1/\delta(\omega)$, respectively.

The skin depth δ is defined as:

$$\delta(\omega) = \sqrt{\frac{2\rho}{\mu_0\omega}}. \tag{2.29}$$

The phase velocity c is defined as:

$$c(\omega) = \sqrt{\frac{2\rho\omega}{\mu_0}}. \tag{2.30}$$

The causal solution is given as:

$$E_x = Ae^{ik_\omega z} = Ae^{-\frac{z}{\delta(\omega)}}e^{i\frac{\omega}{c(\omega)}z}. \tag{2.31}$$

Then the field absorption is frequency dependent. The phase velocity is also frequency dependent.

Angular frequency ω is related to linear frequency of the signal f by:

$$\omega = 2\pi f \tag{2.32}$$

and then,

$$\delta(f) = \sqrt{\frac{\rho}{\mu_0\pi f}} \approx 503\sqrt{\frac{\rho}{f}}, \tag{2.33}$$

$$c(f) = \sqrt{\frac{4\pi f \rho}{\mu_0}} \approx 3160\sqrt{\rho f}\ . \tag{2.34}$$

The wavelength of the signal: $\lambda = 2\pi\delta$. (2.35)

The skin depth δ describes the travel distance where the magnitude of the EM signal is reduced by a factor $e^{-1} \cong 0.37$. A propagation distance of 4.5 skin depths results in an amplitude decay of approximately a factor 100. The phase velocity increases with frequency and resistivity.

The propagation distance depends on two parameters: the resistivity of the material of the earth and the frequency of the signal. The penetration of the EM signal is deeper and further with increasing resistivity and decreasing frequencies. Table 2.1 and 2.2 show the skin depth, phase velocity, and wavelength in a sediment 1 Ωm and 100 Ωm medium, respectively.

Table 2.1 Electromagnetic wave propagation in the 1 Ωm medium.

Frequency *f(Hz)*	**Skin depth δ(m)**	**Phase velocity *c(m/s)***	**Wavelength λ(m)**
0.01	5030	316	31588
0.25	1006	1580	6318
1.0	503	3160	3158.8
4.o	251.5	6320	1579.4

Table 2.2 Electromagnetic wave propagation in the 100 Ωm medium.

Frequency *f(Hz)*	**Skin depth δ(m)**	**Phase velocity *c(m/s)***	**Wavelength λ(m)**
0.01	50300	3160	315884
0.25	10060	15800	63180
1.0	5030	31600	31588
4.o	2515	63200	15794

2.4. Forward problem

The forward problem is important to as inverse problem. In this thesis, we considered a secondary field approach to simulate the distribution of the electric field and magnetic field in a conductivity model.

Consider the isotropic 2D electrical resistivity model (y, z) with strike direction x and some imposed electric sources J_s. Assuming the time variation $e^{-i\omega t}$, the governing equations for the frequency domain electric field $\boldsymbol{E}$ and magnetic field $\boldsymbol{H}$ are given by equations (2.16) and (2.17). The electromagnetic fields are calculated dividedly two parts with the primary fields ($\boldsymbol{E}^p$ and $\boldsymbol{H}^p$) and the secondary fields ($\boldsymbol{E}^s$ and $\boldsymbol{H}^s$). The primary fields are induced by an HED in a 1D layered structure with primary conductivity $\sigma_p(z)$ and the secondary fields are caused by heterogeneities with anomalous conductivity $\sigma_s = \sigma - \sigma_p(z)$. The primary fields will be calculated to get an analytical solution. The total field will be a high accuracy. The secondary fields follow the equations:

$$\nabla \times \vec{E}^s = i\omega\mu_0 \vec{H}^s \,, \tag{2.36}$$

$$\nabla \times \vec{H}^s = \sigma \vec{E}^s + \sigma_s \vec{E}^p \,. \tag{2.37}$$

From equations (2.36) and (2.37), we can get

$$\nabla \times \vec{E}^s = \begin{bmatrix} \vec{i} & \vec{j} & \vec{k} \\ \frac{\partial}{\partial x} & \frac{\partial}{\partial y} & \frac{\partial}{\partial z} \\ E_x^s & E_y^s & E_z^s \end{bmatrix} = i\omega\mu_0 [H_x^s \quad H_y^s \quad H_z^s] \begin{bmatrix} \vec{i} \\ \vec{j} \\ \vec{k} \end{bmatrix}, \tag{2.38}$$

$$\nabla \times \vec{H}^s = \begin{bmatrix} \vec{i} & \vec{j} & \vec{k} \\ \frac{\partial}{\partial x} & \frac{\partial}{\partial y} & \frac{\partial}{\partial z} \\ H_x^s & H_y^s & H_z^s \end{bmatrix} = \sigma [E_x^s \quad E_y^s \quad E_z^s] \begin{bmatrix} \vec{i} \\ \vec{j} \\ \vec{k} \end{bmatrix} + \sigma_s [E_x^p \quad E_y^p \quad E_z^p] \begin{bmatrix} \vec{i} \\ \vec{j} \\ \vec{k} \end{bmatrix}. \tag{2.39}$$

Then we have six equations:

$$\frac{\partial E_z^s}{\partial y} - \frac{\partial E_y^s}{\partial z} = i\omega\mu_0 H_x^s \,, \quad \frac{\partial E_x^s}{\partial z} - \frac{\partial E_z^s}{\partial x} = i\omega\mu_0 H_y^s \,, \quad \frac{\partial E_y^s}{\partial x} - \frac{\partial E_x^s}{\partial y} = i\omega\mu_0 H_z^s$$

$$\frac{\partial H_z^s}{\partial y} - \frac{\partial H_y^s}{\partial z} - \sigma E_x^s = \sigma^s E_x^p \,, \quad \frac{\partial H_x^s}{\partial z} - \frac{\partial H_z^s}{\partial x} - \sigma E_x^s = \sigma^s E_x^p \,, \quad \frac{\partial H_y^s}{\partial x} - \frac{\partial H_x^s}{\partial y} - \sigma E_x^s = \sigma^s E_x^p \,.$$

(2.40)

When the structure follows along the strike direction x in 2D equations, Fourier transformation can be applied to transfer the equation in x direction.

$$\hat{F}(k_x, y, z) = \int_{-\infty}^{+\infty} F(x, y, z) e^{-ik_x x} dx \quad , \tag{2.41}$$

where k_x is the wavenumber in x direction. $\hat{F}$ denotes the value in the wavenumber domain. Transforming the equations group (2.40):

$$\frac{\partial \hat{E}_z^s}{\partial y} - \frac{\partial \hat{E}_y^s}{\partial z} = i\omega\mu_0 \hat{H}_x^s \quad , \tag{2.42}$$

$$\frac{\partial \hat{E}_x^s}{\partial z} - ik_x \hat{E}_z^s = i\omega\mu_0 \hat{H}_y^s \quad , \tag{2.43}$$

$$ik_x \hat{E}_y^s - \frac{\partial \hat{E}_x^s}{\partial y} = i\omega\mu_0 \hat{H}_z^s \quad , \tag{2.44}$$

$$\frac{\partial \hat{H}_z^s}{\partial y} - \frac{\partial \hat{H}_y^s}{\partial z} - \sigma \hat{E}_x^s = \sigma^s \hat{E}_x^p \quad , \tag{2.45}$$

$$\frac{\partial \hat{H}_x^s}{\partial z} - ik_x \hat{H}_z^s - \sigma \hat{E}_x^s = \sigma^s \hat{E}_x^p \quad , \tag{2.46}$$

$$ik_x \hat{H}_y^s - \frac{\partial \hat{H}_x^s}{\partial y} - \sigma \hat{E}_x^s = \sigma^s \hat{E}_x^p \quad . \tag{2.47}$$

The Fourier transformation derivation is given as following with the form of equation (2.43),

$$\int_{-\infty}^{+\infty} \left(\frac{\partial E_x^s}{\partial z} - \frac{\partial E_z^s}{\partial x} \right) e^{-ik_x x} dx = \int_{-\infty}^{+\infty} \left(i\omega\mu_0 H_y^s \right) e^{-ik_x x} dx \quad . \tag{2.48}$$

The left-hand side of equation (2.48)：

$$
\begin{aligned}
&\int_{-\infty}^{+\infty}\left(\frac{\partial E_x^s}{\partial z}-\frac{\partial E_z^s}{\partial x}\right)e^{-ik_x x}dx \\
&=\frac{\partial \hat{E}_x^s}{\partial z}-\int_{-\infty}^{+\infty}\frac{\partial E_z^s}{\partial x}e^{-ik_x x}dx \\
&=\frac{\partial \hat{E}_x^s}{\partial z}-\int_{-\infty}^{+\infty}e^{-ik_x x}dE_z^s \\
&=\frac{\partial \hat{E}_x^s}{\partial z}-E_z^s e^{-ik_x x}\Big|_{-\infty}^{+\infty}+\int_{-\infty}^{+\infty}E_z^s de^{-ik_x x} \\
&=\frac{\partial \hat{E}_x^s}{\partial z}-E_z^s e^{-ik_x x}\Big|_{-\infty}^{+\infty}-\int_{-\infty}^{+\infty}ik_x E_z^s e^{-ik_x x}dx \\
&=\frac{\partial \hat{E}_x^s}{\partial z}-ik_x\int_{-\infty}^{+\infty}E_z^s e^{-ik_x x}dx \\
&=\frac{\partial \hat{E}_x^s}{\partial z}-ik_x\hat{E}_z^s
\end{aligned}
,
$$

and the right-hand side：

$$
\int_{-\infty}^{+\infty}\left(i\omega\mu_0 H_y^s\right)e^{-ik_x x}dx=i\omega\mu_0\hat{H}_y^s
.
$$

If the $\widehat{E_x^s}$ and $\widehat{H_x^s}$ fields which are along the strike-parallel direction given all the fields $\widehat{E_y^s}$ and $\widehat{H_y^s}$, $\widehat{E_z^s}$ and $\widehat{H_z^s}$ can be calculated.

Combining equations (2.42) – (2.48), we can get two partial differential equations for the $\widehat{E_x^s}$ and $\widehat{H_x^s}$ fields.

$$
\begin{aligned}
&\nabla\cdot\left(\frac{\sigma}{\gamma^2}\nabla\hat{E}_x^s\right)-\sigma\hat{E}_x^s-\frac{\partial}{\partial y}\left(\frac{ik_x}{\gamma^2}\frac{\partial\hat{H}_x^s}{\partial z}\right)+\frac{\partial}{\partial z}\left(\frac{ik_x}{\gamma^2}\frac{\partial\hat{H}_x^s}{\partial y}\right) \\
&\quad=-\frac{\partial}{\partial y}\left(\frac{ik_x\sigma_s}{\gamma^2}\hat{E}_y^p\right)-\frac{\partial}{\partial z}\left(\frac{ik_x\sigma_s}{\gamma^2}\hat{E}_z^p\right)+\sigma_s\hat{E}_x^p
\end{aligned}
, \tag{2.49}
$$

$$
\begin{aligned}
&\nabla\cdot\left(\frac{i\omega\mu_0}{\gamma^2}\nabla\hat{H}_x^s\right)-i\omega\mu_0\hat{H}_x^s-\frac{\partial}{\partial y}\left(\frac{ik_x}{\gamma^2}\frac{\partial\hat{E}_x^s}{\partial z}\right)+\frac{\partial}{\partial z}\left(\frac{ik_x}{\gamma^2}\frac{\partial\hat{E}_x^s}{\partial y}\right) \\
&\quad=-\frac{\partial}{\partial y}\left(\frac{i\omega\mu_0\sigma_s}{\gamma^2}\hat{E}_z^p\right)+\frac{\partial}{\partial z}\left(\frac{i\omega\mu_0\sigma_s}{\gamma^2}\hat{E}_y^p\right)
\end{aligned}
, \tag{2.50}
$$

where $\gamma^2 = k_x^2 - i\omega\mu_0\sigma$. The differential equations (2.49) and (2.50) are coupled through the last two terms on the left-hand sides. Hence, these equations must be solved simultaneously for $\widehat{E_x^s}$ and $\widehat{H_x^s}$.

2.5. Inverse problem

In geophysical exploration, inverse problem means making inferences about geophysical systems from real data. Three different issues are required, which are the parameters, the data and the geophysical system model. Predicting data by estimated parameters using the physical theory is called forward problem, by contrast, prediction of parameters from measured data by using mathematical model is called inverse problem. Figure 2.6 illustrates the relationship between the forward and inverse problem.

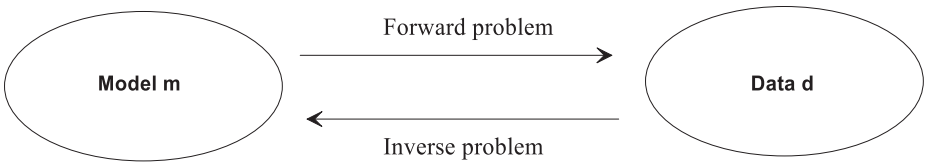

Figure 2.6. *A cartoon depicting the forward problem and inverse problem.*

Taking the first point of view, to solve a 'forward problem' means to predict the error-free values of the observable data ***d*** that would correspond to a given model ***m***. This theoretical prediction can be denoted

$$\boldsymbol{d} = \boldsymbol{F}(\boldsymbol{m}) , \tag{2.51}$$

where $\boldsymbol{d} = \boldsymbol{F}(\boldsymbol{m})$ is a short notation for the set of equations $d_i = F_i(m_1, m_2, \ldots)$ (i = 1, 2, . . .) . The operator ***F*** is called the forward operator.

The 'inverse problem' is to predict a best model ***m*** to fix the observed data ***d***. We will describe two fundamentally different strategies for solving inverse problems in the context of CSEM inversion. Occam's inversion approach is presented by Constable *et al.* (1987). It is successful to be applied 1D marine CSEM by Key (2009). A regularized Gauss-Newton minimization approach described by Rodi and Mackie (2001) has been applied to solve the CSEM inverse problem by Liu and Li (2015).

Solving the inverse problem is generally a very difficult task because it is often an ill-posed problem. It is difficult to find unique and stable solution which exists. Tikhonov regularization may be the most widely applied regularization technique to make the ill-posed problem stable (Tikhonov and Arsenin, 1977). Based on Tikhonov regularization, the inverse problem is formulated as the minimization of the following objective function:

$$\phi = (\phi_d - \phi_d^*) + \lambda\phi_m, \tag{2.52}$$

ϕ_d is the minimization of the data misfit between F(**m**) and **d**. And its inclusion illustrates that minimizing ϕ does not necessarily find the best fitting model, but rather a smooth model that is within the specified target misfit ϕ_d^* (Key, 2009). ϕ_m is the minimization of the model difference between the predicted model **m** and the priori preference model $\mathbf{m_0}$. The factor λ is Lagrange multiplier which trades off the data misfit term and the model misfit term. The factor λ controls the trade-off between the two terms.

The data misfit is expressed as:

$$\phi_d = \|\boldsymbol{W_d}(\boldsymbol{d} - \boldsymbol{F}(\boldsymbol{m}))\|^2. \tag{2.53}$$

The data weighted matrix $\boldsymbol{W_d}$ is a diagonal matrix (Grayver 2013),

$$W_d = diag(1/s_i), \tag{2.54}$$

where s_i is the standard error of ith datum. In other words, W_d weights the relative contribution of each datum to the misfit based on its uncertainty.

The approximate uncertainty model is given by the following expression (Maaø and Nguyen, 2010; Mittet and Morten, 2012):

$$\delta d = \sqrt{(\alpha d_i)^2 + N^2}\,. \tag{2.55}$$

Factor α is the relative error of the ith datum. N is the noise floor of the field data. Thus, data with large errors are scaled to limit their influence, whereas data with small errors will have a larger impact on the misfit budget.

The regularization term is defined by

$$\phi_m = \|\boldsymbol{Rm}\|^2 + \left\|\boldsymbol{P}(\boldsymbol{m} - \boldsymbol{m_{ref}})\right\|^2. \tag{2.56}$$

The first term is a norm of the model roughness and is computed by applying an operator $\boldsymbol{R}$ to the elements of the model vector $\boldsymbol{m}$. $\boldsymbol{P}$ is a diagonal matrix of prejudice weights. For models considered here, $\boldsymbol{m}$ is a vector of $\log_{10}\sigma$ for each parameter; $\boldsymbol{m}_{ref}$ is a priori preference model; and $\boldsymbol{R}$ is chosen to be a matrix calculated by the model differences between parameter cell and the neighbor cells which have the same edge or nodes.

$$\|\boldsymbol{Rm}\|^2 = \sum_{i=1}^{np}\sum_{j=1}^{nb}\frac{A_j}{A_{sum}}\left(\frac{\Delta m_{ij}}{\Delta r_{ij}}\right)^2, \tag{2.57}$$

where np is the number of free parameters; nb is the number of neighbor cells; A_j is the area of the neighboring cell; A_{sum} is the sum of areas of the neighbor cells. Δr_{ij} is the distance between centroid and adjacent cells.

However, in many cases the smooth inversion models are insufficient when the geological structure is expected to vary sharply. From seismic image, a non-Euclidean distance is introduced for a metric tensor field.

The non-Euclidean distance $\Delta\hat{r}_{ij}$ is defined as:

$$\nabla d_s(x)\cdot D(x)\nabla d_s(x) = r_{ij}^2, \tag{2.58}$$

where $d_s(x)$ means the minimum non-Euclidean distance from centroid of center element to centroid of neighbor cells; $D(x)$ is a metric tensor field from seismic image (Hale, 2009a; 2009b); and r_{ij} the distance is between centroid of center element and centroid of adjacent cells.

We replace the distance Δr_{ij} in the equation (2.57) by the non-Euclidean distance $\Delta\hat{r}_{ij}$ which is solved by equation (2.58). Then, the roughness penalty is given as:

$$\|\boldsymbol{Rm}\|^2 = \sum_{i=1}^{np}\sum_{j=1}^{nb}\frac{A_j}{A_{sum}}\left(\frac{\Delta m_{ij}}{\Delta\hat{r}_{ij}}\right)^2, \tag{2.59}$$

where $\Delta\hat{r}_{ij}$ is the non-Euclidean distance from adjacent cell j to the center cell i.

The advantage of non-Euclidean distance is that it is related with the tensor field which illustrates the direction of the feature.

In the Occam's inversion approach, the Lagrange multiplier λ is selected by finding the model $\boldsymbol{m_{k+1}}(\lambda)$ with the best fit to the data, which initially will probably be greater than the target misfit.

For the model updated, linearizing the nonlinear derivative of $\boldsymbol{F(m)}$, and giving an initial model $\boldsymbol{m_k}$, the equation for the updated model in the sequence $\boldsymbol{m_{k+1}}$ is

$$\boldsymbol{m_{k+1}} = [\lambda(\boldsymbol{\partial^T \partial} + \boldsymbol{PP}) + (\boldsymbol{W}\mathbf{J}_{\boldsymbol{k}})^T \boldsymbol{W}\mathbf{J}_{\boldsymbol{k}}]^{-1}[(\boldsymbol{W}\mathbf{J}_{\boldsymbol{k}})^T \boldsymbol{W}\hat{\boldsymbol{d}} + \lambda \boldsymbol{P}\boldsymbol{m_{ref}}], \quad (2.60)$$

where $\hat{\mathbf{d}} = \boldsymbol{d} - \boldsymbol{F}(\boldsymbol{m_k}) + \boldsymbol{J_k}\boldsymbol{m_k}$, (2.61)

$\boldsymbol{J_k}$ is the Jacobian matrix, or the linearized model response gradient. $\boldsymbol{W}$ is the model weight matrix.

where ∂ is the $np \times np$ finite-difference derivative matrix

$$\partial = \begin{bmatrix} -1 & 1 & 0 & 0 & \cdots \\ 0 & -1 & 1 & 0 & \cdots \\ \cdots & \cdots & \ddots & \ddots & \cdots \end{bmatrix}$$

$$\boldsymbol{J_k} = \nabla_m \boldsymbol{F}(\boldsymbol{m_k}), \quad (2.62)$$

where the elements of $\boldsymbol{J_k}$ is

$$J_{ij} = \frac{\partial F_i(m_k)}{\partial log_{10}\sigma_j}, \quad (2.63)$$

where $i=1, 2, \ldots, n$, $j=1, 2, \ldots, m$, and n is the number of data and m is the number of model parameter. In other words, $\boldsymbol{J}$ is a sensitivity matrix containing the derivative of each field component with respect to $\log_{10}\sigma$ in each parameter. A method for efficiently computing $\boldsymbol{J}$ for 1D CSEM was given by Key (2009).

During the inversion process, we define the root mean squared (RMS) misfit to be the criteria of the inversion.

$$\text{RMS} = \sqrt{\frac{1}{n}\sum_{i=1}^{n}\left(\frac{d_i - F_i(m(\lambda))}{\delta E_{x_i}}\right)^2}, \quad (2.64)$$

If the data uncertainty (δE_{x_i}) is well known, a good fitting model has RMS 1.0.

Chapter 3 Comparison of marine CSEM data acquisition system

In Chapter 2, we have introduced the principle of the CSEM survey. In this chapter, the marine CSEM data acquisition systems are introduced by the most popular systems, SBL and TSEM systems. To find out the difference of the two systems, we study the sensitivities and resultions in different enviornments, in which the synthetic data are calculated by both SBL and TSEM systems.

3.1. Introduction

Marine CSEM method uses the high electrical resistivity of hydrocarbon-saturated rocks to discover subsurface rocks that are filled with, such as, gas and oil. The EM field propagates through the water layer and into the subsurface, and the measurements at the receivers can be used to determine the resistivity at different locations and depths (Eidesmo *et al*., 2002; Ellingsrud *et al*., 2002). The method was originally viewed as a deep water technique because of the strong contribution to the electromagnetic field due to the air-water interface in shallow water depths.

Several methods for attenuating the airwave components have been proposed to extend deep water to shallow water (Amundsen *et al*., 2005; Maaø *et al*., 2010; Chen and Alumbaugh, 2011). Some of these methods require a good knowledge of the subseafloor resistivity distribution, because the airwave signal is a function of subseafloor resistivity. Normally, marine CSEM data were analyzed by plotting electric field amplitude versus source-receiver offset. The normalized amplitude was defined as the electrical field amplitude measured over a hydrocarbon prospect divided by the corresponding amplitude measured over a similar non-hydrocarbon bearing area.

In hydrocarbon exploration, marine CSEM is commonly applied as SBL (Ellingsrud *et al*., 2002). SBL method was described as an application of marine CSEM sounding, which used a mobile HED source and an array of receivers that typically measured both horizontal components of the electric and magnetic field (Figure 3.1(top)). The HED source emits a low frequency electromagnetic signal that diffuses outwards both into the overlying water column and downwards into the seabed. The HED source is towed approximately 30 m over the seafloor. The receiver arms are 10 m long, and the distance

bewteen receivers is typically in the range of 1 – 3 km. MacGregor and Tomlinson (2014) discussed the receiver spacing by unconstrained inversion of inline synthetic data.

A TSEM data acquisition system has been developed and tested in the North Sea since 2010 (Linfoot *et al*., 2011a; Zhdanov *et al*., 2012). Although there were many successful case studies presenting the ability of CSEM of detecting hydrocarbon reservoirs, marine CSEM method has not been completely accepted by the industry as an exploration tool. A successful case showed that the TSEM data were suitable for characterisation of the subsurface using resistivity in the Troll field, North Sea (Linfoot *et al*., 2011b). The TSEM system looks very similar to a towed streamer seismic layout (bottom panle in Figure 3.1), which deploys a receiver cable at 100 m depth and a powerful (1500 A) 800 m long horizontal dipole source at 10m depth with an average offset interval of 160 m over offset ranges of 500 m – 7595 m (Key *et al.*, 2014). The towed receiver antenna bipoles lengths are around 200 m – 1100 m increasing with offsets, providing high sensitivity measurements.

Mittet (2008) presented an analysis approach of the effect by water depth using a modified version of normalized amplitude ratio. This ratio is calculated using both the amplitude and the absolute phase of the electromagnetic fields so that it is possible for this method to be used in very shallow water. Using the modified normalized amplitude ratio, Mittet transformed the phase change to an anomalous amplitude. He also gave three differenet water depths model to analyze the effect of water depth. Using the up-down decomposition, the sensitivity to the subsurface resistors could be enhanced by the modified normalized amplitude ratio (Amundsen *et al*., 2005).

A measure of sensitivity to resistive target in marine CSEM was defined by Mittet and Morten (2012). This sensitivity is considered not only normalized magnitude but also the phase and data uncertainty. A hydrocarbon reservoir can be detected in shallow water, which was successfully represented by Mittet and Morten (2013). They also analysed the effect of water depth by the sensitivity to the target model. However, most of the researches focus on study of the SBL data acquisition system.

Shantsev *et al.,* (2012) compared two approaches for acquiring marine CSEM surveys: on towing the horizontal electric dipole transmitter close to the seafloor, and the

other on towing the antenna just below the sea surface, while the receivers are located on the seafloor. They analysed the sensitivity changes with frequency, target depth, navigation uncertainties in various water depth. Because of the attenuation of the EM signal in the seawater, the sensitivity will be different between deep towing and surface towing. As a conclusion, the advantage of the deep towing is that EM energy is less attenuation than that in the surface towing method, and it is preferred at larger water depths. But in the very shallow water depth, less than 250 m depth, the surface towing is likely to become the standard operation. At the shallow water depth, both surface and deep towing give good results in terms of sensitivity and inversion. The analysis is based on the setup with a towed source and seabed receivers described by Shantsev *et al.,* (2010). However, they havn't considered the receivers are towed as a streamer following the transmitter.

In this Chapter, we compared the SBL and TSEM systems. In order to investigate the effects of frequency, offset, water depth, and reservoir burial depth on the CSEM data, synthetic data with different models will be simulated and inverted by 1D modelling and 2D Occam's inversion. Firstly, we establish a measure that allows us to quantitatively compare the sensitivity to a buried thin resistor for different frequencies and offsets. Secondly, we compare the sensitivity to a buried thin resistor for different target depths by using the synthetic data measured from two acquisition systems. Thirdly, we derive an analytic expression for depth resolution of the CSEM inversion with different buried depths of a reservoir. The results of CSEM inversion explain quantitatively and qualitatively the detectability of both the SBL and TSEM systems in different water depth. Then, we build two thin layered 2D models for testing the horizontal resolution of CSEM data inversion, where synthetic data are generated by both of the two acquisition systems. Finally, detectable limitations of SBL and TSEM systems will be compared by analyzing the Occam's inversion results using anomaly transverse resistance ratio. These limitations are for determining the largest target burial depth where the marine CSEM data are able to provide sufficient sensitivity for detection and imaging. We define a reservoir sensitivity index (RSI) for evaluating the sensitivity of marine CSEM data. An evaluation of hydrocarbon reservoir image is given by a transverse resistance ratio and RSI.

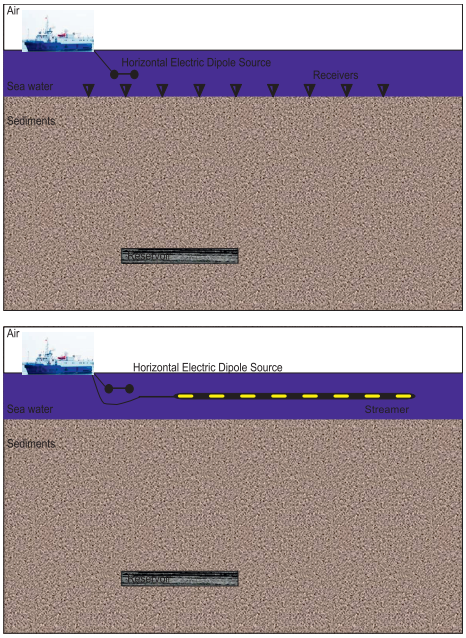

Figure 3.1. *Typical in-line towing configuration of sources and receivers for the SBL system (top). Acquisition geometry for the TSEM system surveys (bottom).*

3.2. Method

3.2.1. Sensitivity

In order to analysis the effect of the water depth, we employed the sensitivity which is defined by Mittet and Morten (2013) given by

$$\left|\frac{\Delta E_x(\boldsymbol{r_r}|\boldsymbol{r_s},\omega)}{\delta E_x(\boldsymbol{r_r}|\boldsymbol{r_s},\omega)}\right|, \tag{3.1}$$

where ΔE_x is scattered field which is difference between the target response and background response; δE_x is the measurement uncertainty; $\boldsymbol{r_r}$ and $\boldsymbol{r_s}$ are the positions of receivers and source, respectively; $\omega = 2\pi f$ is the angular frequency.

The measurement uncertainty is estimated using detailed analysis (Mittet and Morten, 2012; Maaø and Nguyen, 2010) that is a good approximation for offsets which are relevant for this thesis.

$$\boldsymbol{\delta E_x} = \sqrt{(\boldsymbol{\alpha E x_i^{tar}})^2 + \boldsymbol{N^2}}\,, \tag{3.2}$$

Factor $\boldsymbol{\alpha}$ is the relative uncertainty in the electrical field amplitude. In this chapter, $\boldsymbol{\alpha} \approx \mathbf{4}\%$ is given as a constant. $\boldsymbol{Ex_i^{tar}}$ is the ith target response. Noise N is added to the data, both amplitude and phase. The noise distribution is close to random. Noise N is related with frequency and offset.

For the SBL system the noise contribution N varies with depth. Some typical values relevant for normalized amplitude are given by Mittet and Morten (2013), which are used in this chapter for the SBL system and the values of N by Mattson are used for the TSEM system (Mattson *et al*., 2012). In their article, noise reduction techniques tailored for towed streamer CSEM data were presented.

3.2.2. Reservoir sensitivity index (RSI)

Sensitivity is derived as an approximate expression to explain the scattered field from the thin resistor variation with water depth (Mittet and Morten, 2012). Since sensitivity of CSEM varies with frequencies, offsets, amplitude of both resistor model and background model, and noise, it is too complex to evaluate the effect of water depth on the CSEM data. To improve simple detection criteria, the RSI is defined as

$$\mathrm{RSI} = \sqrt{\frac{1}{n}\sum_{i=1}^{n}\left(\frac{|Ex_i^{tar} - Ex_i^{ref}|}{\delta E_{x_i}}\right)^2}, \tag{3.3}$$

where E_x^{tar} is the response of a model containing a high-resistive target, E_x^{ref} is the response of reference model but without the target, δE_{xi} is the uncertainty of the ith datum and n is the number of data points. From equation (3.3), we can see that the RSI is the standard deviation of sensitivity. Compared to sensitivity of CSEM, the RSI is also can be applied for 2D cases.

3.2.3. Occam's inversion

In order to compare data acquired by SBL and TSEM systems, we employ the MARE2DEM code (Key, 2012b, available at http://mare2dem.ucsd.edu/) and Occam inversion algorithm described by Constable *et al.* (1987). Occam's inversion was employed by Key (2009) to solve the regularized problem by searching a smooth model to fit the data. The Occam's inversion has been introduced in the section 2.5. Here we refer to two functions. The first is objective function:

$$\phi = (\phi_d - \phi_d^*) + \lambda\phi_m, \tag{3.4}$$

which ϕ_d is the data misfit, and target misfit is ϕ_d^*. $\phi_m$is the model regularization. The trade-off is Lagrange multiplier λ. The details of ϕ_d and ϕ_m are introduced by equations (2.53) and (2.56), respectively.

The second function is the root mean squared (RMS) misfit as defined in equation (2.64).

$$\mathrm{RMS} = \sqrt{\frac{1}{n}\sum_{i=1}^{n}\left(\frac{d_i - F_i(m(\lambda))}{\delta E_{x_i}}\right)^2}, \tag{3.5}$$

where n is the number of data and δE_{x^i} is the uncertainty of the ith datum.

3.2.4. Transverse Resistance Ratio

Transverse resistance is adjusting the thicknesses and resistivities of a layering model while keeping the transverse resistance unchanged. Baltar and Roth (2013) claimed that transverse resistance is the anomalous transverse resistance (ATR) of the reservoir as the amount of transverse resistance above the value that would exist if no hydrocarbons were present:

$$ATR = \int \Delta R(z)dz, \tag{3.6}$$

where ΔR is the resistivity anomaly due to high resistivity anomaly. The ATR represents the cumulative resistivity contrast over the anomaly zone. Given a 1D resistivity trace extracted from a 2D CSEM inversion model, the transverse resistance equivalence expression is represented as (Baltar and Roth, 2013):

$$\int_{\mathrm{A}} \Delta R_{\mathrm{CSEM}}(z)dz = \int \Delta R(z)dz, \tag{3.7}$$

where A is the CSEM anomaly zone.

Given a relative uniform background resistivity variation over the depth interval of interest defined by the CSEM anomaly in these cases, discretization equation (3.7) can be simplified to

$$ATR_{\mathrm{inv}} = \sum(\Delta R_{\mathrm{CSEM}} * \Delta z) = \int \Delta R_{\mathrm{CSEM}}(z)dz, \tag{3.8}$$

where ATR_{inv} is the ATR of CSEM inversion result, Δz is the actual thickness of the hydrocarbon charged reservoir interval. In this way, we define an ATR ratio as:

$$ATR_{\mathrm{ratio}} = \frac{ATR_{\mathrm{inv}}}{ATR_{\mathrm{true}}} = \frac{\sum(\Delta R_{\mathrm{CSEM}} * \Delta z)}{\Delta R_{\mathrm{log}} * \Delta z_{\mathrm{log}}}, \tag{3.9}$$

where ATR_{true} is the ATR of true model which is used for generating the synthetic data. ΔR_{log} and Δz_{log} are the resistivity anomaly due to hydrocarbons and the actual thickness of the hydrocarbon charged reservoir interval at the well log scale, respectively.

3.3. Examples

In order to make comparison of the two systems, we generated synthetic CSEM data by MARE2DEM code. Eight cases are considered for comparing the sensitivity and resolution of the two acquisition systems. The eight cases are described in table 3.1. For studying the horizontal resolution, a model with one thin reservoir is created to test how small size of reservoir can be detected. A model with two thin reservoirs is built to study the resolution power of the method.

Table 3.1 Cases for sensitivity and resolution comparison.

Cases	Propose	Method
Case 1	Sensitivity with frequencies, offsets	1D modelling
Case 2	Sensitivity with water depth	1D modelling
Case 3	Sensitivity with buried depth	1D modelling
Case 4	RSI with water depth	2D modelling
Case 5	Resolution with water depth	2D inversion
Case 6	Depth resolution	2D inversion
Case 7	Sensitivity VS target dimensions	2D inversion
Case 8	Horizontal resolution	2D inversion

3.4. Results of 1D sensitivity modelling

In order to characterize the sensitivity of marine CSEM method, a resistivity model is built for Case 1, Case 2 and Case 3 for the two acquisition systems (Figure 3.2). The HED source is assumed as a point transmitter in the sea water. The transmitter shooting distance is 200 m for the SBL system. The transmitter is towed 30 m above the seafloor. While the transmitter is towed 10 m below the surface for the TSEM system,

and the shooting distance is 200 m. The streamer with receivers is towed 100 m below the surface in the TSEM system. Measurement frequencies are from 0.05 to 0.75 Hz with 0.05 Hz step for both SBL and TSEM data acquisition systems.

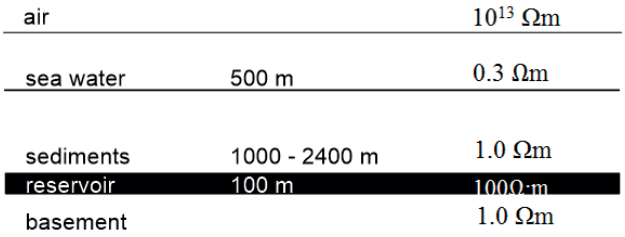

Figure 3.2. *Geometry of a thin resistive layer model for Case 1, Case 2 and Case 3.*

In Figure 3.3, the sensitivity to the target model is shown as square line. Effective and efficient data are selected by the criteria that the anomalous field (circle line) is larger than data uncertainty (cross line), For instance the offset is larger than 1.5 km. The reason is that the EM energy is not lost too much during propagating through the resistive layer. Due to the effects of airwave, the responses of background model is larger than target model resopnse in far offsets area. In this case, the efficient electric field data can be collected by both SBL system and TSEM system in 300 m water depth. Surface towing HED transmitter and streamer has sensitive offset between 2.0 and 4.3 km.

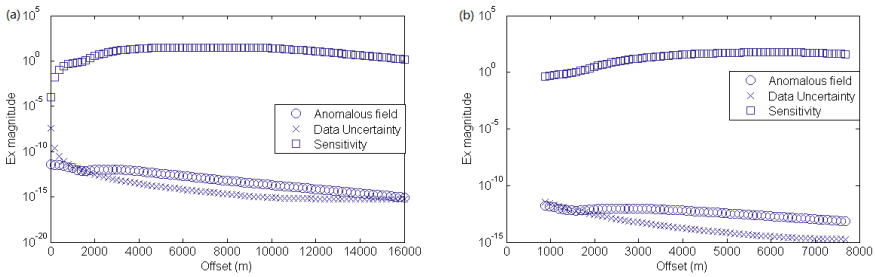

Figure 3.3. *Sensitivities to resistive target are calculated by SBL system (a) and TSEM system (b). The frequency is 0.25 Hz.*

According to equations (3.1) and (3.2), the sensitivity is related with frequency, offsets, and the resistivity of the propagation medium. Firstly, we study the effect of water in 1D model case. Using 1D model described in Figure 3.2, the water depth varies from

200 m to 900 m by 100 m step. Moreover, we give a resistive model with 500 m water depth and 2000 m overburden. Measurement frequencies are from 0.05 to 0.75 Hz with 0.05 step.

3.4.1. Case 1: Effect of frequency and offsets

The sensitivity variation with frequency and offset for the SBL and TSEM systems are shown in Figure 3.4. In this case, the reservoir depth is assumed at 2000 m. Figure 3.4(a) illustrates the sensitivity as function of frequency and offset for the SBL system data acquisition system. Since the hydrocarbon reservoir is buried 2000 m below the seafloor, the receivers can detect the electromagnetic signal from the reservoir at double burial depth. When the offset is smaller than twice as the reservoir depth, the sensitivity is smaller than 2.0 for the field absorption.

The sensitivity of the TSEM system data is shown in Figure 3.4(b). Because of the limitation of the streamer length, the maximum offset is 8000 m for the TSEM system. As mentioned above, the TSEM system has an 800 m long source. The electrode pair receiver antenna bipole length are 200 and 1100 m. It means that accurate modelling of the system requires both a bipole source and bipole receivers in the modelling code (Key *et al*., 2014). In this case, the source and receivers are modeled as horizontal point dipoles. This first order approximation is sufficient for the sensitivity calculations in this study.

Since both the source and streamer receivers are far away from the seafloor in this case with 500 m water depth, the high frequency part of the electromagnetic field decreases by the seawater. Hence, the sensitivity decreases for frequencies larger than 0.4 Hz compared to the seafloor based node system in this relatively deep water case.

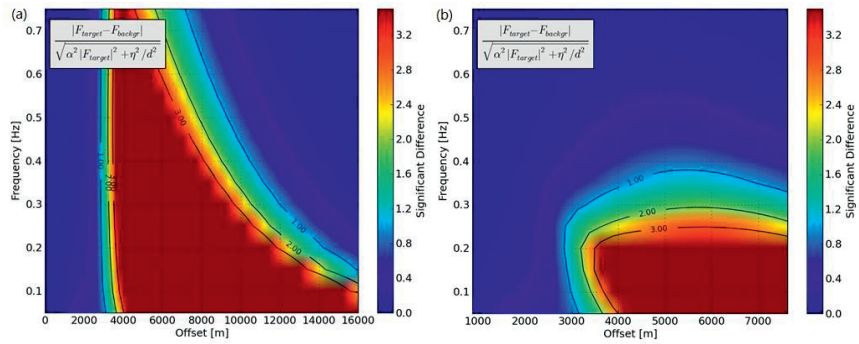

Figure 3.4. *Sensitivity variation with frequency and offset for (a) SBL system and (b) Towed streamer system.*

3.4.2. Case 2: Effect of water depth

In this section, we study the effect of water depth in 1D model case. We employ the resistivity model as given in Figure 3.2. The water depth varies from 200 m to 900 m by 100 m step. The 0.25 Hz frequency is transmitted by both SBL and TSEM systems.

Figure 3.5 illustrates the CSEM sensitivity curve variation with water depth. When the water depth increases, the magnitude value decreases in SBL system. However, in TSEM system, the magnitude value decreases only in near offset. The CSEM data uncertainty are increasing with water depth when the water depth is deeper than 400 m. The main reason is that the EM signal propagated through deep water is lost and the airwave will have a strong response at far offset area.

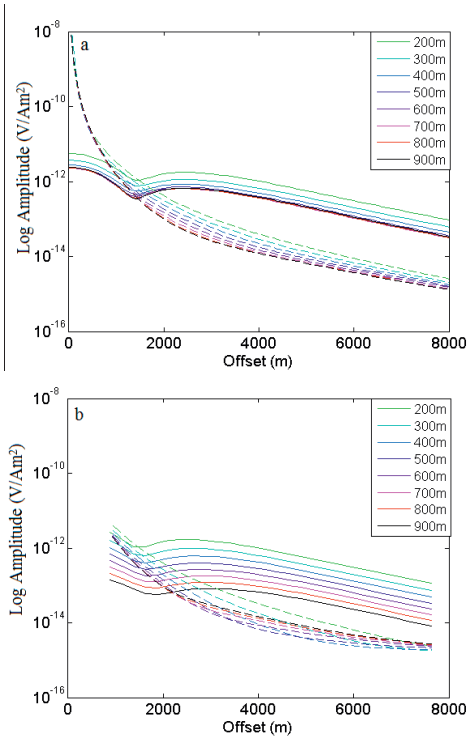

Figure 3.5. *CSEM data anomalous field（solid line） and uncertainty （dashed line） varies in offsets with different water depth collected by SBL system (a) and TSEM (b).*

We have studied the sensitivity range with reservoir burial depth in an intermediate water depth in the previous section. In this section, we consider the effect of the water depth on sensitivity of the two acquisition systems. For comparison, we choose a shallow thin resistive layer model to ensure the sensitivity efficiently. The resistivity model is employed with only range and water depth. The sensitivity to the target is measured by both SBL system and TSEM system.

In this case, the various noise levels are given in different water depth. We will borrow a definition of the term airwave, which refer to any signal arising by interactions with the air-water interface. In the shallow water case, the difference of the target and background model contribution is large due to the airwave and the response for a resistive anomaly increase.

Concerning the sensitivity in SBL system, both deep water and shallow water have an apparently high sensitivity. At shallow water case, airwave and multiple reflections between the air surface and seafloor will increase the anomalous field, so that there is a very high sensitivity. In the case with intermediate water depth, the sensitivity is reduced because the relative contribution of the propagation path through the target is not as strong as in deep water due to the setting in primary airwave. However, in the deep water, all EM signal reaches the receivers propagation path through the subsurface, especially the high resistive layer. The main contribution is the EM energy travelling through the hydrocarbon reservoir.

In Figure 3.6, the reservoir is burial at 1.2 km depth from the seafloor. Figures 3.6(a) and (c) show the sensitivity to the target at frequency 0.25 Hz, 0.75 Hz, respectively. For the shallow water, the increase in background signal amplitude with reduced water depth is accompanied with a corresponding increase in burial resistor scatter field. This increased scatter field leads to an increasing sensitivity with the decreasing water depth. Therefore, the sensitivity is decreasing when the water depth increases from 200 m to 500 m in Figure 3.6(a). The amplitude of the scattered field is almost constant for the water depths larger than 500 m (Mittet and Morten, 2012). But the uncertainty and noise level decrease with raising the water depth when it is deeper than 500 m. The sensitivity grows up when the water is deeper than 500 m.

When it comes to the TSEM system, there is almost no sensitivity at deep waters because the EM signal is extraordinarily attenuated in the conductive seawater. However, a good sensitivity to the target could be obtained at the intermediate water depths. In the shallow water case, high sensitivity can be obtained for the target detection. For the TSEM system, fast and accurate measurements are the advantages which SBL system cannot offer: (1) the depth of both HED source and streamer with receivers could keep nearly constant during the data acquisition, (2) the position of the HED source could be measured by GPS system. Mattsson *et al.* (2012) presented noise reduction techniques to keep the total error below 3%, including the navigation uncertainty, measurement error and noise reduction processing error in addition to the electric field noise.

In Figure 3.6(b), for the shallow water, the sensitivity is growing up with the increasing water depth at 0.25 Hz. At the water depth of 200 m ~ 400 m, the sensitivity has a peak in 0.25 Hz frequency case. The sensitivity decreases sharply when the water depth becomes deeper than 400 m. In other words, the sensitivity to CSEM data has a peak at 400 m water depth for the TSEM system at 0.25 Hz. Figure 3.6(d) describes the sensitivity at 0.75 Hz. The sensitivity decreases with increasing the water depth. When the water depth is larger than 500m, the TSEM system has a low sensitivity to the hydrocarbon reservoir target.

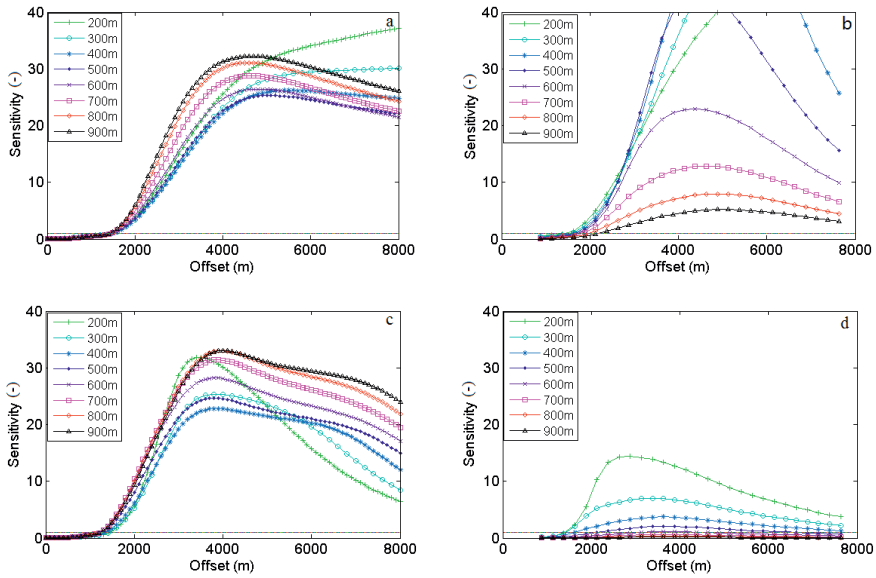

Figure 3.6. *CSEM data sensitivity variation with offsets and water depth collected by SBL system (a), (c) and TSEM (b), (d). Different curve illustrates sensitivity for different water depth. The frequency is 0.25 Hz in (a) and (b), and 0.75 Hz in (c) and (d).*

3.4.3. Case 3: Effect of reservoir burial depth

In studying the relationship between sensitivity and reservoir depth, the same resistivity model in Figure 3.2 is considered but with varying reservoir burial depth. In these cases, the transmitter frequencies are 0.25 and 0.75 Hz. The water-depth-independent contribution to the ambient noise N is chosen as 10^{-15} V/Am^2, 10^{-14} V/Am^2 for uncertainty in the SBL and TSEM systems, respectively. The top of reservoir is buried at depth of 1200, 1600, 2000, and 2400 m, respectively.

We calculate the sensitivity defined by equation (3.1) and the uncertainty model described by equation (3.3) for the burial depths from 1200 m to 2400 m. The results are illustrated in Figures 3.7 and 3.8 at the frequency of 0.25 Hz and 0.75 Hz, respectively. Figure 3.7(a) shows that the sensitivity to the target is good for all reservoir depths for the SBL system. However, the sensitivity to the target buried below 2400 m is difficult to detect as shown in Figure 3.7(b) for the TSEM system. The sensitivity reduces with the increasing reservoir depth.

Figure 3.8 shows the sensitivity to the target at 0.75 Hz. The SBL system can still detect a target at 2000 m but fails to detect the 2400 m case based on the sensitivity attribute being larger than 1 (Figure 3.8(a)). Based on the same criteria, the TSEM can only detect the shallowest target. Figure 3.8(b) illustrates that the sensitivity to the shallow target with 1200 m depth is larger than 1.0 which means the shallow target is detectable. In other words, it is difficult to detect the deep target at a high frequency 0.75 Hz by the TSEM system.

Compared the results shown in Figures 3.7 and 3.8, the TSEM system has an advantage at shallow reservoir detection, while the SBL system apparently has a deeper reservoir detectability. In the low frequency case, a shallow target can be very well detected by both of acquisition systems. But it is difficult to obtain a good sensitivity for deeper target by the TSEM system. For the TSEM system, only 1200 m deep reservoir

shows sensitivity to the target in Figure 3.8(b). In other words, the sensitivity to the target is sharply reduced for the TSEM system.

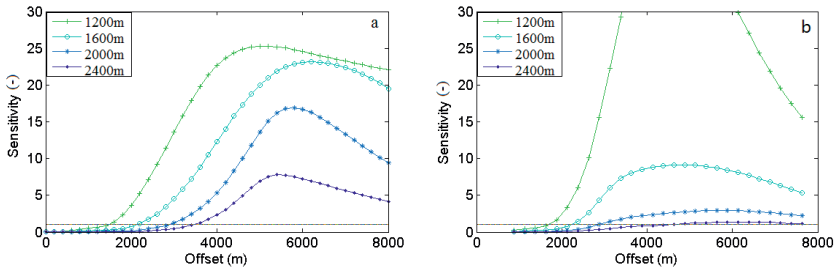

Figure 3.7. *The synthetic data measured by (a) SBL system and (b) TSEM system in different reservoir burial depths at 0.25 Hz.*

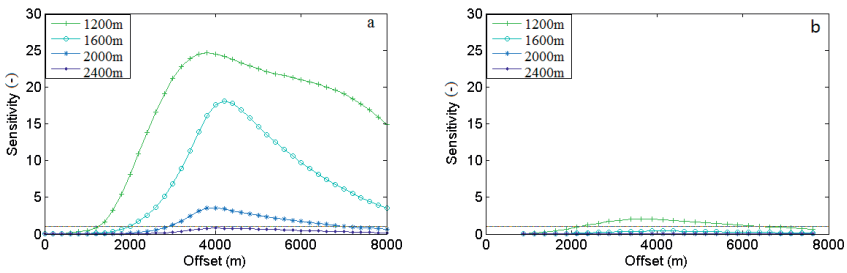

Figure 3.8. *The synthetic data measured by (a) SBL system and (b) TSEM system in different reservoir burial depths at 0.75 Hz.*

3.5. Results of 2D layers models

In this section three cases are considered to study the resolution of the SBL and TSEM systems by using Occam inversion introduced in section 2.5. Regularized smooth inversion is used to analyze the resolution (Constable *et al*., 1987; Key 2009). Case 4 studies the sensitivity with the various water depths by using the RSI; Case 5 and Case 6 study the resolution with various water depths and reservoir buried depths, respectively; Case 7 studies the resolution with various reservoir lengths; and Case 8 studies the resolution with the horizontal distance between two reservoirs. The true resistive model for Cases 4, 5, 6 and 7 is a thin resistive layered (100 Ωm) model embedded in a

conductive medium (1 Ωm) given in Figure 3.9. The resistivity of air and sea water is the same as the 1D model shown in Figure 3.2. The parameters of the two acquisition systems are given in table 3.2. In Figures 3.9 to 3.15 to be shown, the white dots represent the receivers with 1 km interval for the SBL system, and the source locations for the TSEM system with a 250 m interval. The offsets for the TSEM system are ranges from 883 m to 7595 m.

Table 3.2 Model parameters of the CSEM acquisition systems

Parameters	SBL	TSEM
Source distance (m)	200	250
Frequency (Hz)	0.25, 0.75	0.25, 0.75
Noise floor (V/Am^2)	10^{-15}	10^{-14}
Standard error	0.4	0.4
Source length (m)	270	800
Source depth	30 m above the seafloor	10 m below the surface
Receivers position, spacing	On the seafloor & 1 km	100 m below the surface & 160 m

The HED source and streamer are towed from east to west. The first shot starts at 10 km. After 72 shots, the end is located at -7.7 km for all the cases. Because the streamer is 7.7 km long, the last receiver is located at 0 km. In the SBL system, 11 receivers are located between 0 km and 10 km with equal spacing of 1 km. The distance between the transmitter shots is 200 m, which is towed from 20 km to -10 km for data acquisition. Both of the two systems cover the interesting area (Figure 3.9).

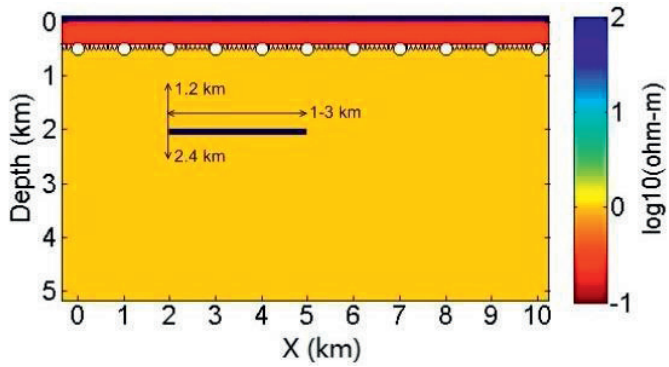

Figure 3.9. *Simple model with a thin resistive layer embedded in a conductive background medium.*

3.5.1. Case 4: Effect of water depth on RSI

In order to study the effect of water depth in 2D thin layer resistivity model, the synthetic data are measured in different water depths. In these cases, we assume that the reservoir is buried 1.2 km below the seafloor in the resistivity model shown in Figure 3.9.

Figure 3.10 shows the RSI measured using each of the two different data acquisition systems. According to equation (3.2), the curves demonstrate that the RSI value varies with a increasing water depth. As a result, the RSI to the target in the SBL system increases with the increasing water depth. Because of the reduction of noise, the RSI has a high value at deep water. However, the RSI in the TSEM system decreases smoothly with increasing water depth. When the water depth increases, the distance between seafloor and receivers streamer is also increasing. EM energy is absorbed by seawater, and then the CSEM data anomalous field decreases. Additionally, the signal to noise ratio is also increasing with water depth.

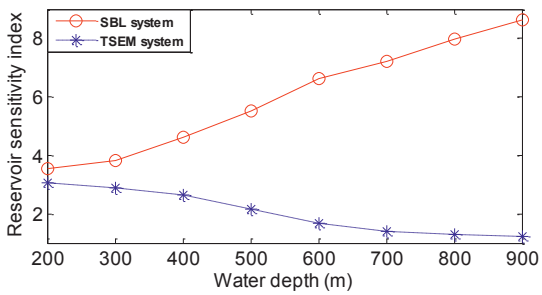

Figure 3.10. *RSI as a function of water depth for the two acquisition systems.*

3.5.2. Case 5: Effect of water depth on depth resolution

To test the effect of water depth in 2D thin layer resistivity model, we also invert the synthetic CSEM data by using Occam inversion (Key, 2009; Key and Ovall, 2011). These synthetic data are simulated by MARE2DEM, and the water depth is setted as 300, 500, 700, and 900 m. The frequencies are 0.25 and 0.75 Hz. The resistivity model is shown in Figure 3.9, where the reservoir is buried 1.2 km below the seafloor. The water depth is 0.3 km for (a) and (b); 0.5 km for (c) and (d); 0.7 km for (e) and (f) and 0.9 km for (g) and (h), respectively.

The inversion results are summarized in Figure 3.11, where the differences between the TSEM system and the SBL system are able to be effectively and efficiently distinguished.

In shallow water both methods are able to provide quality resistive images. With increasing water depth, the qualities of the resistive image of TSEM system deteriorate due to the absorption of the electromagnetic wave in the water. At the same time, the airwave does not attenuate while traveling along the sea surface. In this case, the lower signal to noise ratio results in a poorer image in deep water than in shallow water.

However, the opposite phenomenon is also observed for the SBL system. In the deep water case, the attenuation of a diffusive field in the water caused by a reduction of the airwave signal, and as a consequence the signal to noise ratio increases with increasing water depth. The deeper the water depth is, the better inversion results which cloud be given by the SBL sytem. When the water depth is 900 m, it is difficult for TSEM system to detect the anomaly of reservoir.

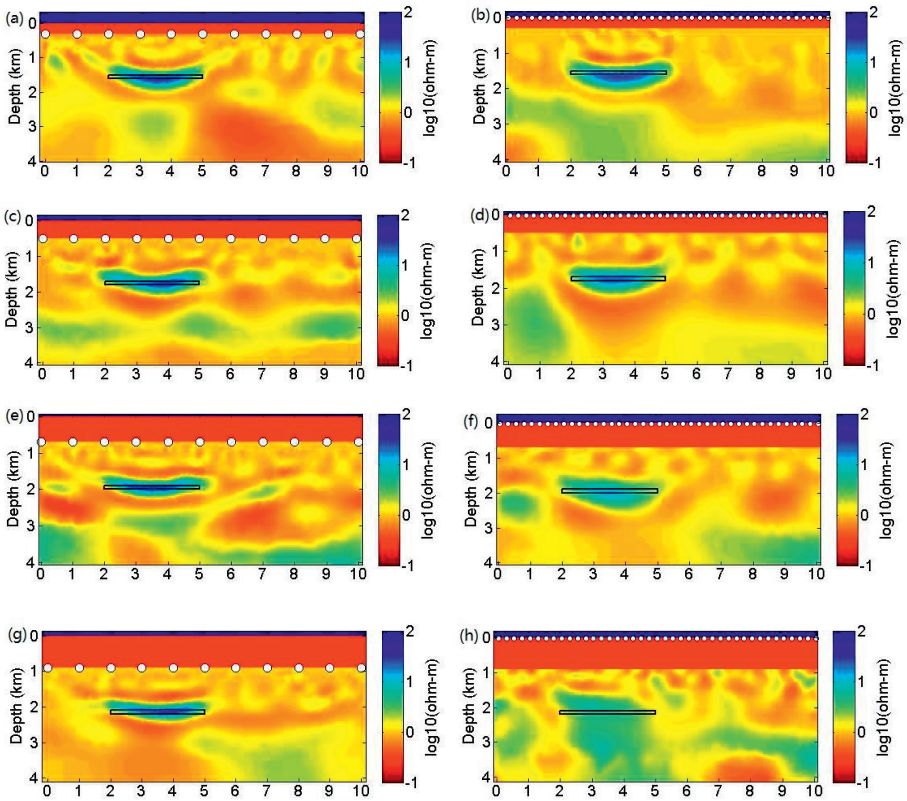

Figure 3.11. *Inversion results of SBL system (left) and TSEM system (right) in various water depth.*

3.5.3. Case 6: Effect of reservoir depth on depth resolution

Case 3 studies Occam's inversion resolution with variation of reservoir depth. The data used for inversion examples are obtained from a simple 2D reservoir model (Figure 3.9). The top of the thin resistive layer lies at a depth of 1.2, 1.6, 2.0 and 2.4 km below the seafloor for testing the resolution with reservoir depth. The parameters for the data measurement are listed in Table 3.2. In order to study the detectability, the fixed water depths at 300, 500 and 700 m are used for the tests. The effects of the water depth are discussed in the previous subsection. So the fixed water depth at 300 m is only given as an example for the tests.

The inversion results give in Figure 3.12 show that none of the data acquisition systems can get good inversion results when the reservoir is buried of 2400 m. The reservoir depth is 1.2 km for 3.12(a) and (b); 1.6 km for 3.12(c) and (d); 2.0 km for 3.12(e) and (f) and 2.4 km for 3.12(g) and (h), respectively. When the reservoir depth increases, the anomaly area by the inversion increases but the value of resistivity parameter becomes small as shown in Figures 3.12(a), 3.12(c), 3.12(e) and 3.12(g) for the SBL system and 3.12(b), 3.12(d), 3.12(e) and 3.12(h) for the TSEM system.

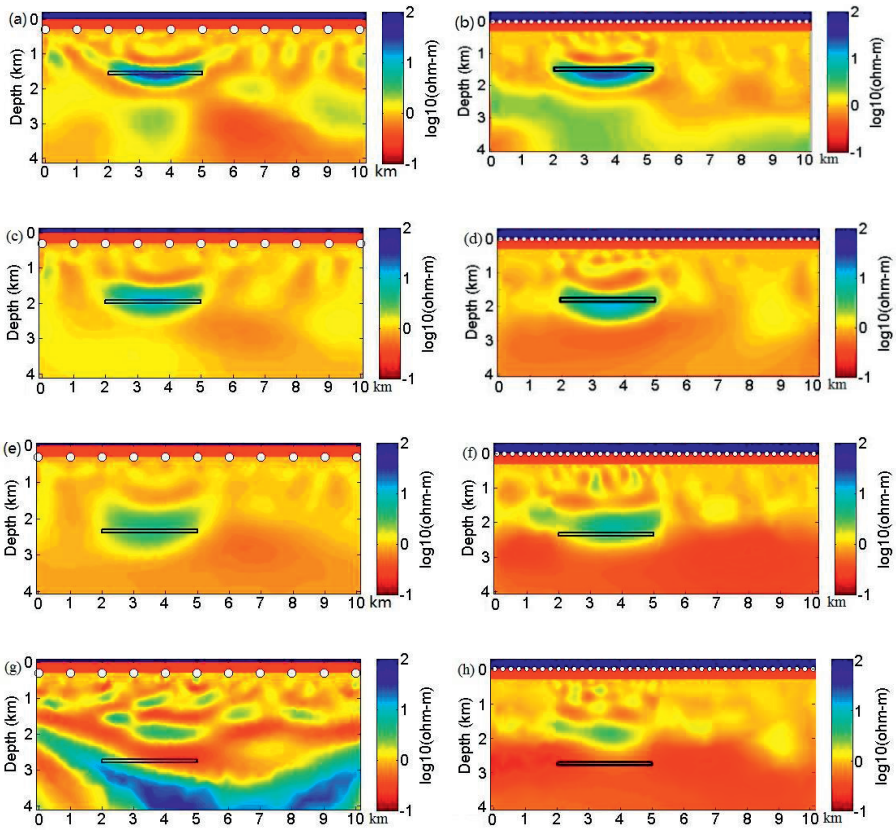

Figure 3.12. *Inversion results from SBL system (left) and TSEM system (right) for 300m water depth.*

3.5.4. Case 7: Effect of target dimensions on sensitivity

In order to study the sensitivity versus target dimensions of two acquisition systems, we tested a simple model with variation reservoir length, 2.0, 1.5, 1.0 km. The

model is shown in Figure 3.9. The water depth is 300 m, and the reservoir is buried 1 km below the seafloor. The acquisition parameters are given in table 3.2.

Figure 3.13 illustrated the Occam inversion results of varying reservoir length model. Left panels present SBL system inversion results, and right panels present results acquired by TSEM system. The reservoir lengths are 2.0 km for Figures 3.13(a) and 3.13(b), 1.5 km for Figures 3.13(c) and 3.13(d) and 1.0 km for Figures 3.13(e) and 3.13(f).

With the reduction of reservoir length, there are fake anomalies in the Occam's inversion results by SBL system. One reason of the artifaces may that we choose wrong parameters for the Occam's inversion. The wrong parameters lead to the RMS misfit is larger than the target misfit. The Occam's inversion has not started to smooth the model, when the Occam's inversion finished. Another reason may be the few data points of the acquisition system. In order to overcome this problem, more inversion examples could be tests in the future, for instance, changing the inversion parameters or giving a higher target misfit to test the smooth model, adding or removing receivers to test the data points.

Comparing the results from SBL system, the inverted resistvity results of the TSEM system have a better horizontal resolution. The reason of the good solution of the inversion may that the distance between the neighbor receivers of the TSEM system is smaller than that of SBL system. In this way, the very dense spatial sampling can be offered by the TSEM system.

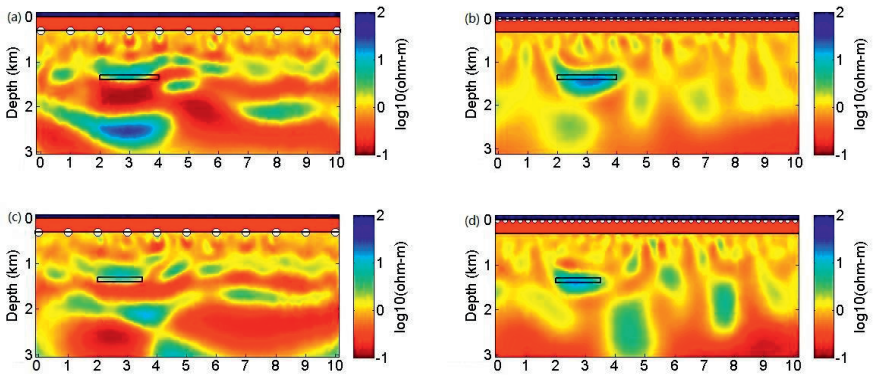

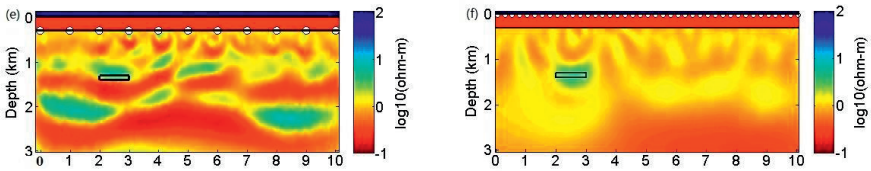

Figure 3.13. *Inversion results from SBL (left) and TSEM (right) system.*

3.5.5. Case 8: Effect of reservoir distance on horizontal resolution

In this section, we test the horizontal resolution for a model with two close reservoirs. A model for Case 8 (Figure 3.14) is built to simulate CSEM synthetic data for this testing. The 2D model consists of two equal sized resistive reservoirs of 2.0 km × 0.1 km along x and z directions, respectively. One reservoir is located between 2km and 4km in x direction with 100 Ωm resistivity and the other has the same resistivity and burial depth. The distances between the two reservoirs are 2 km and 1 km. The parameters in table 3.2 are used for the CSEM data inversion.

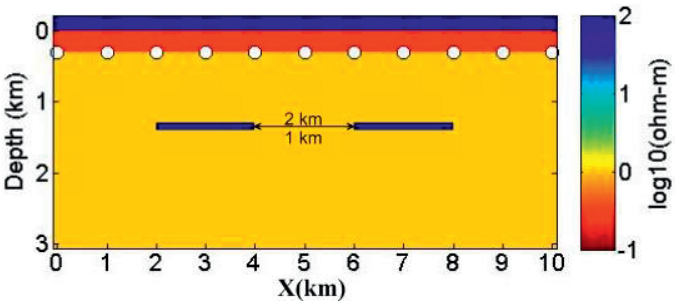

Figure 3.14. *A thin resistive layered model embedded in a conductive background medium for analyzing the horizontal resolution (Case 8).*

Inversion results of the synthetic data generated by the two acquisition systems are illustrated in Figure 3.15. The length of the two reservoirs is 2.0 km and the distance between the two reservoirs is 2.0 km in 3.15(a) and (b); 1.0 km in 3.15(c) and (d). The distance between the two reservoirs is 2 km in the true model. The results show that both of the SBL and TSEM systems are able to detect the two resistive anomalies. The depths of the anomalies detected using the SBL system are a little shallower than that of the true model shown in Figure 3.15(a), while the clear anomalies are located at the right place by the TSEM system shown in Figure 3.15(b).

Figures 3.15(c) and 3.15(d) show the results by Occam inversion when the distance between the two reservoirs is 1 km. The two reservoirs estimated by the SBL system in Figure 3.15(c) are connected as a large anomaly. In contrast, the two anomalies are clearly separated by the TSEM system in Figure 3.15(d).

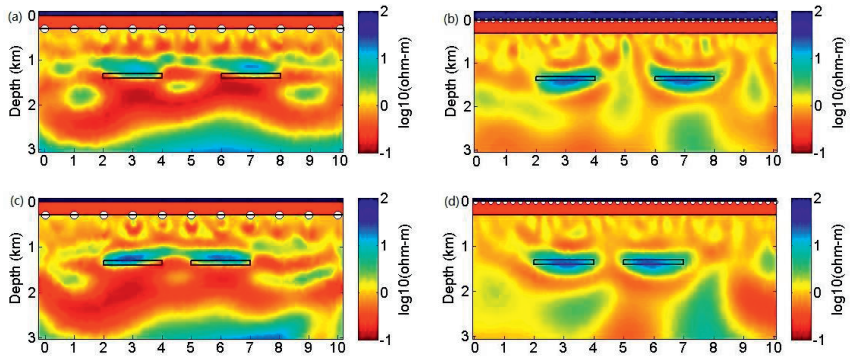

Figure 3.15. *Inversion results from SBL system (left) and TSEM system (right) for 300m water depth.*

3.6. Analysis of ATR ratio

3.6.1. ATR ratio with variation of water depth

Apparently, CSEM inversion results can be evaluated by analysis of resistive image. Additionally, ATR ratio is able to evaluate the resistive image quickly. Using this method, a fast evalution of CSEM sensitivity could be performed before carrying out CSEM inversion work.

The inversion results in Case 5 are used to study ATR ratio. According to equation (3.9), ATR_{ratio} depends on both ATR_{true} and ATR_{inv}. In these cases, ATR_{true} is equal to 9900 Ωm^2. ΔR_{CSEM} refers to the resistivity anomaly owing to hydrocarbons in the CSEM resistivity trace. ΔZ_{CSEM} is the thickness of the CSEM anomaly in the CSEM resistivity trace. ΔR_{CSEM} of 500 m is used for calculation anomaly transverse resistance. A ratio of 0.3 is used as the quality criteria by experience. If the ratio is below 0.3, the resistivity image is accepted for interpretation. For hydrocarbon filled reservoir depth varying, three water depths corresponding to deep water, intermediate water, and shallow water are

considered. When the reservoir depths vary from 1.2 (blue), 1.6 (green) and 2.0 (red), the results are illustrated in Figure 3.16.

Figure 3.16(a) demonstrates transverse resistance ratio variation with water depth collected by the SBL system, and the curve for data acquired by the TSEM system is presented in Figure 3.16(b). From Figure 3.16(a), the trough of low ATR ratio is at 500 m water depth. Especially, when the reservoir depth is 2.0 km, the ATR ratio is lower than 0.3 in the SBL system. Similar results can be given by 1D sensitivity model case. The sensitivity is lowest at 500 m water depth (Figure 3.6(a)), but the ATR ratio has a peak at 400 m water depth by towed streamer. In other words, TSEM system has the best sensitive and resolution at 400 m water depth (Figure 3.6(b)). In the deep water, the ATR ratio of TSEM system is too low to give a quality resistive image of CSEM inversion result. When the reservoir depth increases, the ATR ratio decreases sharply. In both of very shallow water and deep water environments, the ATR ratio is low when the reservoir depth is 2.0 km.

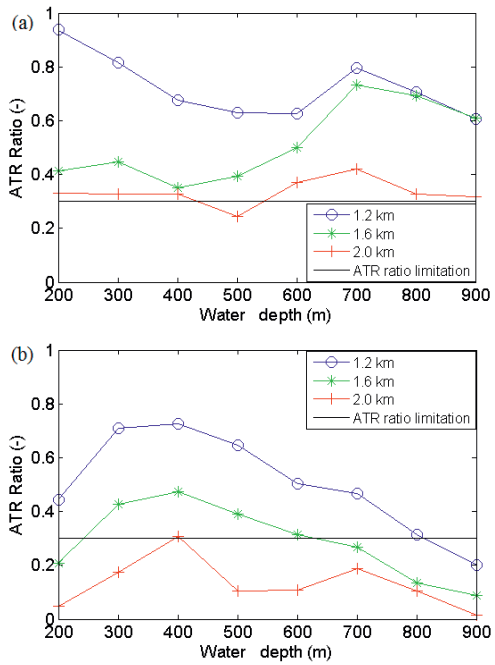

Figure 3.16. *ATR ratio variation with water depth by (a) SBL system and (b) TSEM system for reservoir buiral depths.*

3.6.2. ATR ratio with variation of reservoir depth

The inversion results in Case 6 are used to study Anomaly Transverse Resistance ratio. The ATR ratio is calculated using equations (3.8) and (3.9) and shown in Figure 3.17. The quality criteria is 0.3 by experience, the same as above. If the ratio is below 0.3, the resistivity image is not accepted for interpretation. The ATR ratio varies with reservoir depth illustrated in Figures 3.17(a), (b), (c) and (d) for the water depths of 300, 500, 700, and 900 m, respectively.

As depicted in Figure 3.17(a), ATR ratio of inversion results varies with increasing reservoir depth at shallow water of 300 m depth. The ATR ratio decreases with increasing reservoir depth. Because the airwave affects the response of hydrocarbon reservoir in shallow target case, the ratios in both acquisition systems in 1000 m reservoir depth are lower than that in 1200 m reservoir depth case. The fact that linearly decreasing curve reflects the transverse resistance ratio reduces with reservoir depth indicates that to some extent the detectability of CSEM method is declined. Both of the data acquisition systems are able to provide a qualified resistivity image when the reservoir is buried less than 1800 m below the seafloor.

In the intermediate water 500 m, the ATR ratio of the SBL system is similar to that of the TSEM systemin in Figure 3.17(b). As shown in Figure 3.17(b) the ATR ratio value for the TSEM system declines sharply when the reservoir depth increases from 1600 m to 1800 m. The CSEM inversion result is not able to provide a high resolution image in 1800 m reservoir depth case by the TSEM system. Although the ATR ratio of the SBL system at 1800 m is smaller than 0.3, yet it is larger than that of the TSEM system. Accordingly, the SBL system has an advantage in deep reservoir case with intermediate water depth.

In Figure 3.17(c), it is no doubt that the ATR ratio of the SBL system is higher in deep water 700 m model than in intermediate water 500 m model. Even though the reservoir is buried 2000 m below the seafloor, the inversion result of synthetic data acquired by the SBL system has high resolution.

The detectable limitation of the TSEM system reduces with increasing water depth. When the water depth is 900 m, the ATR ratio is illustrated in Figure 3.17(d). The TSEM system can only have a quality resistivity image for very shallow reservoir.

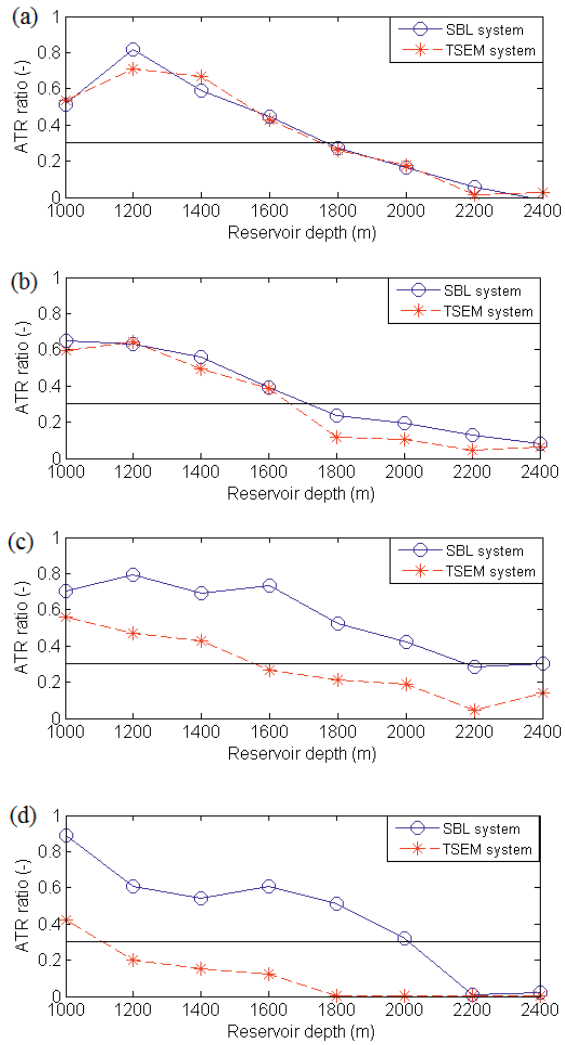

Figure 3.17. *ATR ratio variation with reservoir depth by SBL system (solid line) and TSEM system (dashed line) for water depth of 300 m (a), 500 m (b) 700 m (c) and 900 m (d).*

3.7. Discussion and Conclusion

The marine CSEM method has advantages and disadvantages like other geophysical methods. In order to evalue the CSEM method, the effects of frequency, offset, water depth, target depth, target dimensions and the horizontal resolution in context of sensitivity and resolution have beenstudied for both the SBL and TSEM data acquisition system. Three methods are applied for these investigation, 1D sensitivity modelling, the RSI and Occam's inversion with ATR ratio.

1D sensitivity modelling can provide a fast evaluation of the CSEM data acquisition systems. The responses of 1D modelling show that the sensitivity for the SBL system method is different from TSEM system method in different frequencies and offsets. Both SBL and TSEM systems have good sensitivity for shallow resistive target detection. The detectable limitation of the TSEM system reduces as increasing water depth.

The effects of water depth and target depth on the detectable limitation is studied by 1D sensitivity model and 2D modelling and inversion. The advantage of the SBL system is preferable in deep water environment because of the lower EM energy lost during propagating through the sea water. This study has demonstrated that in shallow water depth of 300 m both acquisition systems are useful for marine CSEM hydrocarbon exploration. In shallow water envoirnments, the TSEM system gives good and qualified responses in terms of sensitivity and inversion as the SBL system.

In 2D cases, the RSI can provide a fast evaluation of the sensitivity to the target. This method has been tested for simple 2D thin layer cases. The RSI curves demonstrate a similar relationship bewteen the detectability and the water depths. But this method cannot show more details information.

To get more information, Occam's inversion is employed for the 2D simple layer case. The inverted resistivity results illustrate that the depth resolution is related to water depth. In shallow water environment, both SBL and TSEM systems have good resolution of CSEM inversion. The signal interacting with the air affects the received fields and can limit sensitivity to sub-seafloor structure. Using RSI, the sensitivity of marine CSEM data

could be evaluated before inverting CSEM data. When the water depth increases, the depth resolution of the SBL data is better than that of the TSEM data.

Because it is difficult to compare the resistivity results from two data acquisition system, an ATR ratio is introduced to evalue these resistive image. By analyzing ATR ratio of resistive image from marine CSEM data inversion, we have considered 0.3 as a criteria to evaluate the inversion results. The detectable limitation of target depth depends on the water depth, geologic setting, frequency and offsets. The exact reservoir detection limitation depth has been tested for water depth of 300, 500, 700 and 900m in both SBL and TSEM systems.

Based on the above methods, the SBL system is preferred in deep water environment, while the TSEM system is better in the shallow water case. In our cases, the SBL system has a disadvantage in 500 m water depth. But in both shallow and deep water environments, the SBL system can provide a high quality data acquisition. Furthermore, the best water depth interval for TSEM system is between 300 m and 600 m. At 400 m water depth, it has an advantage. In deep water, it is not a good environment for TSEM system.

In the target depth case, both two systems lose the resolution of deep target. Concerning the sensitivity of target dimentions and horizontal resolutions, the TSEM system has an advantage. The TSEM system provides a clear resistivity image when revervoir length is 1 km and it is able to distinguish two shallow reservoirs by Occam's inversion when the reservoirs are at 1 km distance.

There are some limitations of these comparison study. Firstly, the model is assumed as a simple isotropic model. And 1D sensitivity modelling and 2D inversion cannot describe a 3D and anisotropic world. The SBL system has an advantage of 3D data acquistion. The boardside data is not considered in these cases either. Secondly, the selection of inverted parameters may lead to different results. More parameters tests may provide better inversion results. Thirdly, for the 1D sensitivity modelling, the lengths of the souce and receivers are not considered. Finally, there are new technologies for two data acquisition system updated. In my studies, I have not considered these new

technologies, for instance the bipole source and bipole receivers for TSEM sytem, the deep towed equipments technology for both systems.

In the future, the studies of the sensitivity and resolution may be tested in 3D domain and anisotropic environment. More Occam's inversion may be tested to figure out the better parameters. The noise can be well estimated for the CSEM modelling.

Although these researches have limitations, they can be used to identify experimental limiting factors and to guide the selection of acquisition systems for hydrocarbon exploration. We believe that the comparison studies are useful for improving acquisition systems.

Chapter 4 Seismic coherence driven sparse CSEM inversion

In the Chapter 3, we discussed the difference of the SBL and TSEM data acquisition systems. We employed the Occam's method to invert the synthetic data for studying the resolutions. Because of the large number of free parameters, the Occam's inversion has a high computational cost. In this chapter, we present an irregular sparse mesh that it can reduce the computational cost while it keeps resolution.

4.1. Introduction

It is common to create 2D or 3D resistivity cubes from controlled-source electromagnetics (CSEM) data by inversion techniques involving modelling and data fitting (Zach and Frenkel, 2009; Brevik *et al*., 2009). These techniques are applied in 2D and 3D large models by inverting the dataset on a mesh with discretized cells (Commer and Newman, 2008; Gabrielsen, 2009). There has been already some work done by using seismic constraints in CSEM inversion (da Silva *et al*., 2012; Brown *et al*., 2012).

The choice of discretization of the inversion model is a critical aspect. An ultra-fine discretized mesh can provide a high resolution resistivity image but at high cost. For the CSEM inverse problem, the mesh or grid does not need such a high precision because of the limited resolution of electromagnetic waves in conductive media compared to a seismic image. Therefore, the optimal solution would be the inversion on a grid or mesh that provides good resolution without increasing the computational cost and physical memory.

The traditional method used to choose the inverse model mesh is to generate a fine discrete mesh (Constable *et al*., 1987). Occam's inversion algorithm was employed by Key (2009) to solve the regularized problem by searching a smooth model to fit the data on these meshes. A staggered grid was introduced to increase resolution of inversion in seismic application (Louis *et al*., 2005; Michelini, 1995). It shows a high resolution image by shifting and merging a number of low resolution images (Vesnaver and Böhm, 2000; Arato *et al*., 2014).). Meanwhile, the staggered grid electrical resistivity tomography method is effective in reducing the formation of artifacts from the inversion procedure,

but using a coarser grid, the time used for inversion is less than the finer grid inversion. In addition, the mesh cannot be too coarse without limitation due to numerical dispersion.

A coarser mesh can be used for the inverse problem, which has the benefit of reducing computational cost. Böhm *et al*. (2000) defined an algorithm for automatic gridding which is based on Delaunay triangulation and Voronoi tessellation. This algorithm can also adapt the tomographic grid to the velocity gradient, by increasing the local resolution where its modulus is larger than a chosen threshold for seismic inversion.

Traditionally, unstructured meshes are generated for Occam's inversion (Constable *et al*., 1987). An unstructured uniform triangle mesh was generated by MARE2DEM code (Key and Ovall, 2011; Key, 2012). Although their unstructured model mesh can readily conform to known complex features, the number of cells needed to describe the shallow part of the model can be significantly reduced by using structural information contained in a seismic image. On one hand, a coarse mesh is efficient to limit the computational cost; on the other hand, an ultra-fine mesh is needed to obtain small-scale details of the model. The main goal of this chapter is to replace the unstructured uniform mesh by an irregular mesh that follows existing geological structures. Seismic images can be used to build an irregular sparse mesh that represents the shape of geological structures. This sparse mesh is composed of two parts: large-scale cells describe regions where the resistivity is expected to be relatively constant, while areas where the resistivity is more variable are represented by small-scale cells. The total number of cells in the irregular sparse mesh is less than that in the fine regular mesh (Böhm *et al*., 2000).

Our approach is to use a seismic image to build irregular meshes. In order to build the irregular mesh we extract segments from the seismic image and nodes from a seismic coherence section to build triangular cells by Delaunay triangulation.

Traditionally, there are several methods to extract nodes directly from seismic information. For instance, a set of properly chosen locations for scattered nodes were used for implementing image-guided sparse full waveform inversion by Ma *et al*. (2012). The nodes are located on the features and between the reflectors. Triangular meshes can be generated by these nodes; however it is computationally very expensive and suboptimal.

In order to improve the edge generated along the faults direction, a coherence section is employed to replace the seismic image.

In our approach, the features are picked from the seismic image as the skeleton of the sparse mesh. The vertices of triangles are extracted from the seismic coherence slice, which was used by Bahorich and Farmer (1995) as an efficient method for seismic data interpretation. The coherence slice shows not only the faults with clarity but also the intensively fractured region to the top. A corner detection approach defined as Harris corner detection (Harris and Stephens, 1988) is employed to extract the nodes from the coherence slice. Then, this skeleton map will be filled by nodes to create the triangle meshes.

In order to generate a quality mesh, the angle of triangle cells should be larger than 25 degrees (Key, 2009). A conforming Delaunay Triangulation (CDT) of a seismic coherence PSLG is a true Delaunay triangulation in which each PSLG segment may be subdivided into several edges by the insertion of additional vertices, called Steiner points (Shewchuk, 2002). Steiner points are generated by two steps. The Steiner points in the first step are generated from the nodes of seismic coherence PSLG, and in the second step, the Steiner points are generated by Delaunay Triangulation. An efficient sparse triangular mesh for CSEM data inversion should include both the structured features exactly and have fewer inversion parameters.

In this chapter, an irregular sparse mesh generation method for CSEM inversion is proposed. The proposed sparse mesh is defined as coherence-based irregular (IC) mesh, which is generated by Delaunay Triangulation method based on the vertices and segments from coherence section.

The details of the IC mesh generation method are given. Two synthetic models are tested to show the inverse resolution and computational cost for different meshes. The results show that the computational cost by using the IC mesh is much reduced without losing resolution.

4.2. Method

The fact that hydrocarbon reservoirs are characterized by high resistivity, but CSEM data lead to models with low spatial resolution. Hence, imposing these constraints is relevant. It is important to get a higher resolution by a fine mesh in this area. This fine mesh is generated by using small scale cells around the faults and reflected horizons.

Coherence artifacts have different types. Some types of the coherence artifacts can lead to the existence of higher or lower density of nodes. The nodes extracted from these artifacts are used to generate the irregular sparse meshes. The resistivity image is sensitive to the CSEM data on the area both seismic coherence artifacts and anomalies. The thorough interpretation of coherence should be done before the mesh generation. In this paper, the impact of artifacts in the inversion result is not investigated, but can potentially introduce a bias in the result.

The IC mesh generation method consists of three major steps: (1) Create the seismic coherence section to detect the structured features of interest. (2) Extract corner nodes and horizons as vertices and segments for triangle mesh generation. (3) Create sparse meshes based on these vertices and segments by using MARE2DEM. The mesh of the starting model of CSEM inversion includes geological features such as horizons and faults which are represented as sides of triangles in 2D meshes.

Step (1) is explained below. Based on the method of the location structure tensors introduced by Tchon *et al*. (2006), we employed the seismic coherence to generate the sparse mesh. Figure 4.1 illustrates the difference of faults from the seismic image (a) and coherence section (b). The skeleton of the sparse mesh, horizons and faults are picked from seismic image. Then, this skeleton map is filled by special nodes extracted from the seismic coherence to create the triangle meshes. Based on the skeleton, a coarse irregular triangle meshes are created by Delaunay Triangulation.

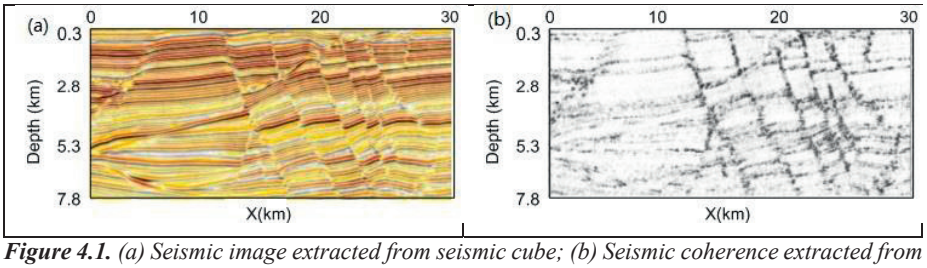

Figure 4.1. *(a) Seismic image extracted from seismic cube; (b) Seismic coherence extracted from coherence section.*

In step (2) nodes are extracted by Harris corner detection method (Harris and Stephens, 1988) based on the seismic coherence section shown in Figure 4.1(b). Seismic coherence PSLG is used for sparse mesh generation, which includes both structure features and corner points from the seismic coherence map. Since the vertices are extracted based on the seismic coherence, a number of small size triangular meshes are generated automatically near the faults. The distance of two neighbor vertices is limited by the size of triangle cells of fine mesh.

In Figure 4.2, the red nodes are picked as vertices for mesh generation based on Figure 4.1(b).

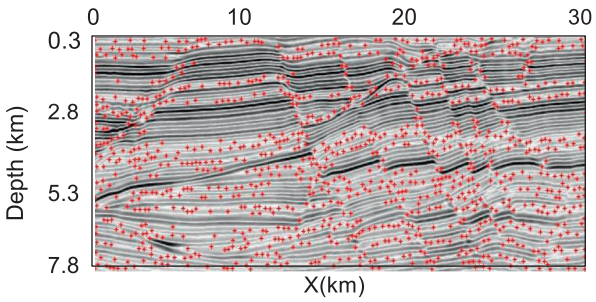

Figure 4.2. *Harris corner detection results on seismic gray image. Red star is the location of the nodes, which are sited as vertices of the triangles in the meshing generation. The nodes are detected from seismic coherence.*

In step (3) the sparse mesh is generated based on the vertices shown in Figure 4.2. The IC mesh (Figure 4.3) is created by MARE2DEM code.

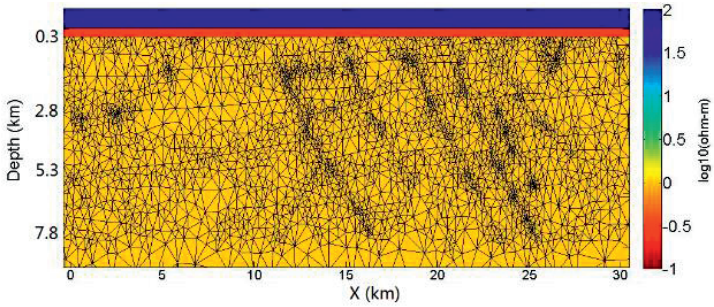

Figure 4.3. *Coherence-based structured mesh generated by MARE2DEM code.*

MARE2DEM code and Occam's inversion algorithm described by Constable *et al.* (1987). Although the starting model is simulated with a coarse mesh, a goal-oriented adaptive finite element method designs sufficiently dense mesh around sources and receivers to obtain sufficient accuracy for each forward modelling (Key and Ovall, 2011). Occam's inversion was employed by Key (2009) to solve the regularized problem by searching a smooth model to fit the data. The details of the Occam's inversion are introduced in section 2.5.

$$\phi = (\phi_d - \phi_d^*) + \lambda\phi_m, \tag{4.1}$$

which consists of two terms: the misfit of the model's forward response to the data, and a norm of the model roughness. ϕ_d is the data misfit and ϕ_d^* is target misfit. ϕ_m is the minimization of the model difference between the predicted model $\boldsymbol{m}$ and the priori preference model $\boldsymbol{m_0}$. To seek a best fitting model, the model misfit should be updated to reach the target misfit. In Occam's inversion, the RMS misfit varies with iteration including two phases. For Occam phase 1, the algorithm is sweeping through λ and finding the best fitting model, iteration will stop until the target misfit is obtained. Once the target misfit is obtained, the iteration will work as Occam phase 2. It will find the largest λ for that misfit. In this chapter, we mainly consider the reduction in computational cost for phase 1.

For the model updated, giving an initial model $\boldsymbol{m}_k$, the equation for the next model in the sequence $\boldsymbol{m}_{k+1}$ is given as equation (2.60)

$$\boldsymbol{m_{k+1}} = [\lambda(\boldsymbol{\partial}^T\boldsymbol{\partial} + \boldsymbol{PP}) + (\boldsymbol{W}\mathbf{J}_{\boldsymbol{k}})^T\boldsymbol{W}\mathbf{J}_{\boldsymbol{k}}]^{-1}[(\boldsymbol{W}\mathbf{J}_{\boldsymbol{k}})^T\boldsymbol{W}\widehat{\boldsymbol{d}} + \lambda\boldsymbol{P}\boldsymbol{m}_{\boldsymbol{ref}}], \tag{4.2}$$

where

$$\hat{\mathbf{d}} = \boldsymbol{d} - \boldsymbol{F}(\boldsymbol{m_k}) + \boldsymbol{J_k}\boldsymbol{m_k}\ , \tag{4.3}$$

$\boldsymbol{W}$ is the model weight matrix. The operator $\boldsymbol{F}$ is called the forward operator. $\boldsymbol{J_k}$ is the Jacobian matrix, or the linearized model response gradient. **P** is a diagonal matrix of prejudice weights.

$$\boldsymbol{J_k} = \nabla_m F(\boldsymbol{m_k}), \tag{4.4}$$

where, the elements of the Jacobian matrix

$$J_{ij} = \frac{\partial F_i(m_k)}{\partial log_{10}\sigma_j}\ , \tag{4.5}$$

where $i=1, 2, \ldots, n$, $j=1, 2, \ldots, m$, and n is the number of data and m is the number of model parameters which are the conductivities σ. in each element $\boldsymbol{m}$ is a vector of $log_{10}\sigma$. $\boldsymbol{J_k}$ is the kth iteration of Jacobian matrix $\boldsymbol{J}$ containing the derivative of each field component with respect to $\log_{10}\sigma$ in each parameter. A method given by key (2009) is adopted in this chapter for efficiently computing $\boldsymbol{J}$ for 1D CSEM.

We define the root mean squared (RMS) misfit to be the criteria of the inversion.

$$\text{RMS} = \sqrt{\frac{1}{n}\sum_{i=1}^{n}\left(\frac{d_i - F_i(m(\lambda))}{\delta E_{x_i}}\right)^2}\ , \tag{4.6}$$

where n is the number of data and δE_{x_i} is the uncertainty of the ith datum.

As shown in equations (4.2) and (4.3), the computational cost in Occam phase 1 is the sum of the Jacobian matrix calculations, model updates, and forward modelling calls.

4.3. Synthetic marine CSEM survey examples

A synthetic inversion example from a marine environment is used and the synthetic data are generated from a 2D isotropic resistivity model illustrated in Figure 4.4. The skeleton of the model comes from the same structural model shown in Figures 4.1(a) and (b). The model contains a resistive reservoir (100 Ωm) with length 4.4 km and thickness 0.1 km (the black area in Figure 4.4). The same geological features as the

seismic image illustrated in Figure 4.1(a) are applied to build the resistive background. The reservoir is embedded in a homogeneous and isotropic conductive background. All the parameters in the test model are given in Table 4.1. The top of the thin resistive layer lies at a depth of z = 1500 m below the sea surface (z = 0 m). The background has a complex geology with several faults. Synthetic electric field data for two frequencies 0.25 and 0.75 Hz are generated by MARE2DEM (Li and Key, 2007; Key and Ovall, 2011). 3% Gaussian noise is added to the data and data below a noise floor of 10^{-15} V/Am^2 are removed. The receivers recording the inline electric field are spaced 1 km along the line; the distance between the transmitter shots is 200 m.

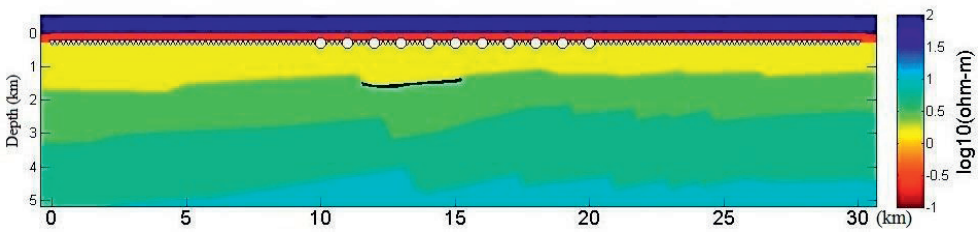

Figure 4.4. *True resistivity model for CSEM inversion test. The rectangle is the interesting area. White spots represent receivers' location. White triangles are the locations where the sources transmit electromagnetic waves.*

Table 4.1 Resistivity in test model

Layer	Resistivity (Ωm)
Sea water	0.3
Sediment layer 1	1.0
Sediment layer 2	3.0
Sediment layer 3	5.0
Base	10.0
Hydrocarbon reservoir	100.0

Normally, a regular dense (RD) mesh is generated as shown in Figure 4.5(a). If the size of triangles is small enough, this mesh can describe complex features. In order to reduce the computational cost, a regular sparse (RS) mesh is given in Figure 4.5(b). If we know the geological features, we can generate a horizon-based irregular dense (IH) mesh

as shown in Figure 4.5(c). The IH mesh is constrained by the features from the seismic image. Finally, we build an IC sparse mesh using the proposed method, which is illustrated in Figure 4.5(d). To study the resolution and computational cost of the IC sparse mesh, we invert the synthetic CSEM data by using these four meshes.

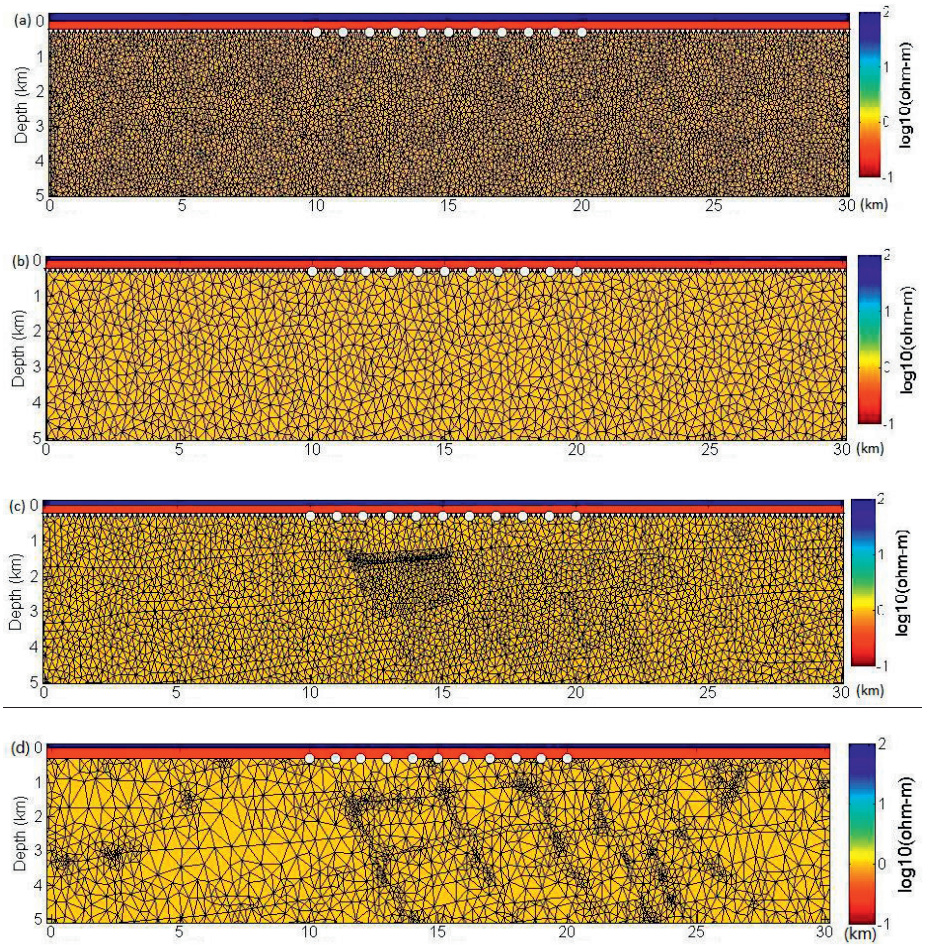

Figure 4.5. *Building meshes of the starting model for Occam inversion by MARE2DEM. (a), RD mesh with 14600 cells. (b), RS mesh with 6700 cells. (c), IH mesh with 12900 cells. (d), IC mesh with 5900 cells.*

We invert the synthetic dataset using four different meshes. For comparison, the 10th iteration inverse results for the four different meshes are used, where the RMS misfit

is slightly above the target misfit. Occam's inversion results are calculated by MARE2DEM code, and the results are shown in Figure 4.6 together with the exact resistivity model.

Although we invert CSEM data from a 14600 parameters RD mesh, the resistivity image shown in Figure 4.6(a) does not provide the same quality as the seismic image. The resistive anomaly thickness estimated is around 300 m (the true value is 100 m). However, this image is good enough for interpretation.

When the number of parameters is reduced to 6700 for a RS mesh, the sizes of the triangle cells are larger than that of the RD mesh. Since the model is described by fewer parameters, the Occam's inversion reduces computational cost per iteration. But the resolution of the inversion result using the RS mesh (Figure 4.6(b)) is not as good as the one using the RD mesh (Figure 4.6(a)).

The IH mesh has slightly fewer free parameters for inversion than the RD mesh. The high resistive anomaly of the IH mesh image shown in Figure 4.6(c) is stronger than that from the RD mesh (Figure 4.6(a)).

Unlike the image with the RS mesh, the resistive image using the IC mesh shown in Figure 4.6(d) has good resolution for interpretation, although the number of parameters is less than for the RS mesh. The 5900 parameters IC mesh has less than half of the RD mesh. However, the resistive model with the IC mesh provides an image as good as the RD mesh. Moreover, the image from the inversion with the IC mesh has good resolution in the area below the anomaly where the image with the RD mesh produces an artificial anomaly (Figure 4.6(a)). As a result, CSEM inversion from the IC mesh provides better resolution than the RD mesh.

Compared with the RS mesh, the IC mesh has similar number of parameters, but the resistive image with IC mesh provides better result with fewer parameters. The anomaly of the reservoir is stronger than shown in Figure 4.6(b). The IC mesh can also predict the faulted area below the hydrocarbon anomaly.

The inversion with the IH mesh has the best resolution among these meshes. The image with the IC mesh does not have as good resolution as the IH mesh. However,

compared to the true model shown in Figure 4.6(e), the resistive image with the IC mesh has a similar layer structure. The thin layer resistive anomaly and the basement anomaly can be interpreted.

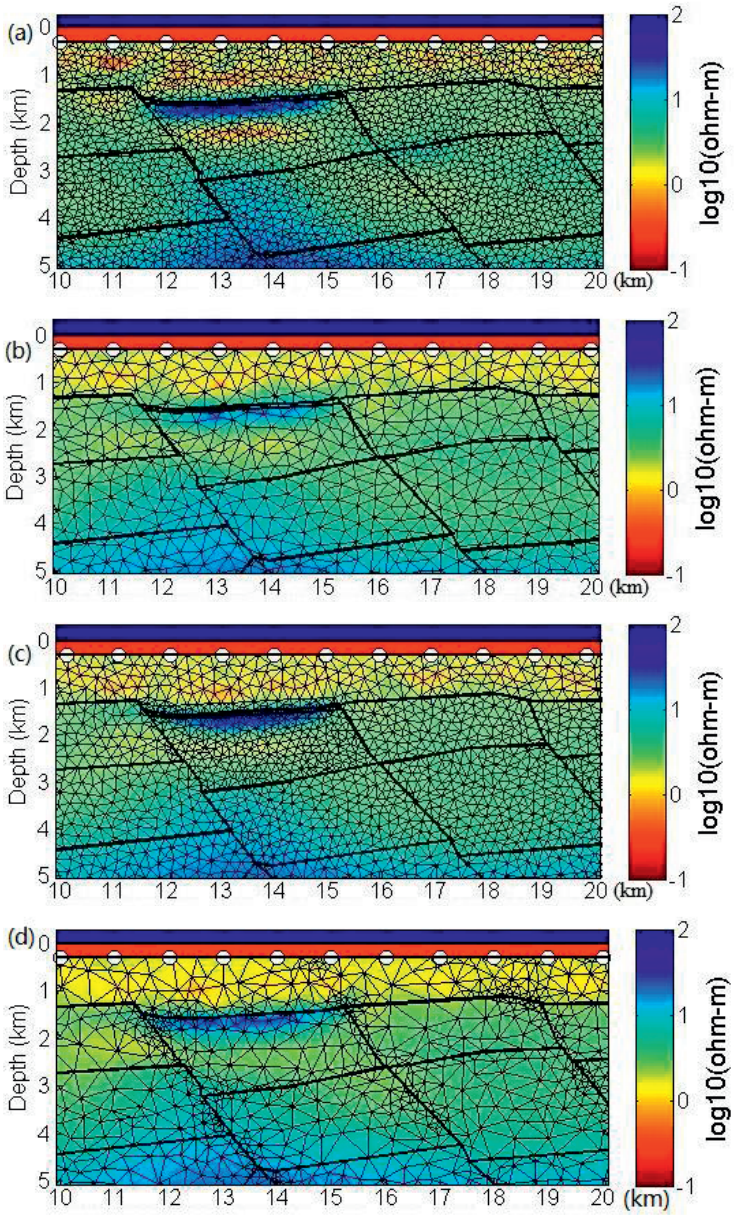

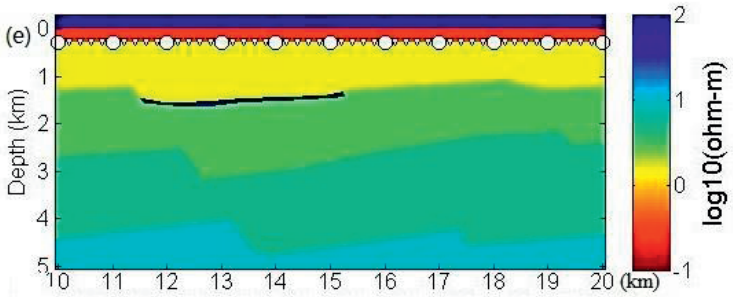

Figure 4.6. *CSEM inversion result by using (a) RD mesh, (b) RS mesh, (c) IH mesh, and (d) IC mesh. The final RMS is 1.22 for (a), (b) and (d) respectively, and 1.23 for (c). (e) True resistivity model for synthetic data.*

The RMS misfit variation with iteration number for phase 1 is given in Figure 4.7 and the target misfit is 1.20. Due to the small difference of the RMS misfits per iteration, it is difficult to determine which method converges faster. The computational cost of IC mesh allows for the same rate of convergence as the RD mesh. However, the inversion on the IC mesh is at a smaller computational cost. Therefore, it is necessary to analyze the time used in different parts in the Occam's inversion for different meshes.

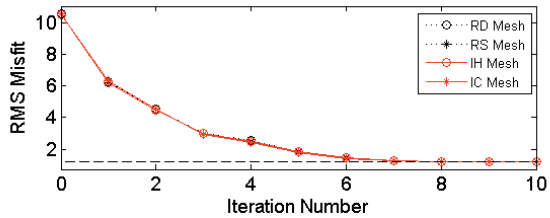

Figure 4.7. *RMS misfit variation with iterations using different meshes. Dashed lines for regular meshes and solid lines for irregular meshes.*

The total accumulated computational time is illustrated in Figure 4.8. It increases with iteration number and is related to the number of triangles in the meshes. So the sparse meshes save computational time and physical memory. Because of optimization of the nodes position by this approach, the inverse problem is allowed for a reduction in the dimension and for this reason it accelerates execution speed. Furthermore, there is little difference between the cost of inversion with the IC mesh and the RS mesh.

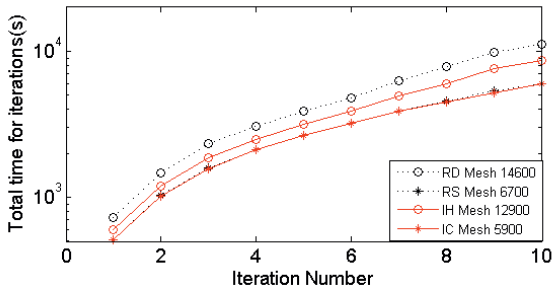

Figure 4.8. *The total time cost with CSEM data inversion iterations. Dashed lines for regular meshes and solid lines for irregular meshes.*

The cost of Occam's inversion in each iteration includes three parts: Jacobian matrix calculation, matrix operation for model updates, and forward modelling calls. The computational time for each part in each iteration is plotted in Figure 4.9 in logarithmic scale. The four different meshes cost approximately the same for Jacobian calculation shown in Figure 4.9(a). But the cost of model updates increases with the number of triangle cells. As shown in Figure 4.9(b), the IC mesh has an advantage on this part. In addition, the sparse meshes also save time on forward modelling as illustrated in Figure 4.9(c). The cost of the forward modelling is also a cumulative time for all the iterations. If the number of forward modelling calls is the same per iteration, the accumulated computational cost is a linear function of the iteration numbers.

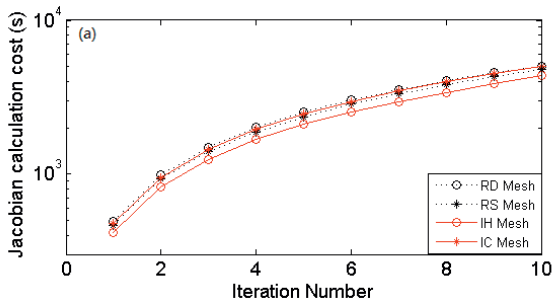

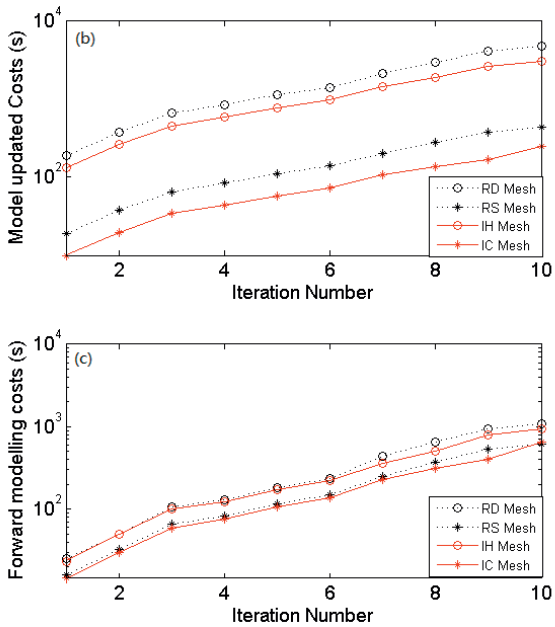

Figure 4.9. *The total time for (a) Jacobian calculation; (b) Model update; (c) forward modelling.*

The time used in each part is shown in Figure 4.10. The cost of Jacobian matrix calculation is similar for the four different meshes. The forward modelling spends no more than 1000 s for the sum of 10 iterations. Compared with the dense meshes the RD and the IH, sparse meshes the RS and the IC save little time on the Jacobian matrix calculation. Apparently, sparse meshes reduce the computational cost due to reduction of the matrix dimension during model updates. However, the computational time is not only dependent on the Jacobian matrix calculation, matrix operation, and forward modelling calculation but also the number of forward modelling calls and iterations.

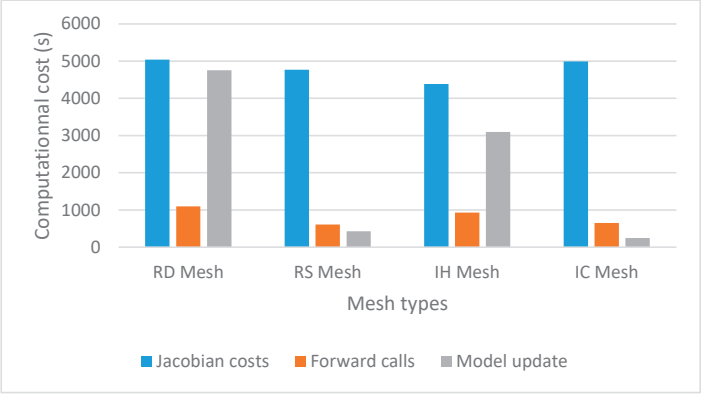

Figure 4.10. *Main computational cost for the different meshes.*

If we only consider the computational time of phase 1, the sparse mesh has an advantage on saving computational cost and physical memory.

However, the total time for Occam's inversion also depends on the computational time of phase 2. In phase 2, the inversion method tries to find a smooth model fitting the data, and the forward modelling is called to regularize the model. Because the mesh has an influence on the regularization and smoothing, the computational time in phase 2 is unpredictable for the different methods.

The reduction of inversion parameters is necessary to save computational cost. The question is if it is possible to have comparable inversion result in terms of data misfit and quality of the inverted model. The number of elements of the IC sparse mesh is determined by the vertices extracted from the coherence section. In order to answer the question, we have tested three different models, where the numbers of vertices are 500, 750, and 1000 for the generation of starting meshes. The numbers of the parameters for inversion are 3100, 3800 and 5400, respectively. Inversion results with the IC mesh 500, the IC mesh 750, and the IC mesh 1000 are shown in Figure 4.11.

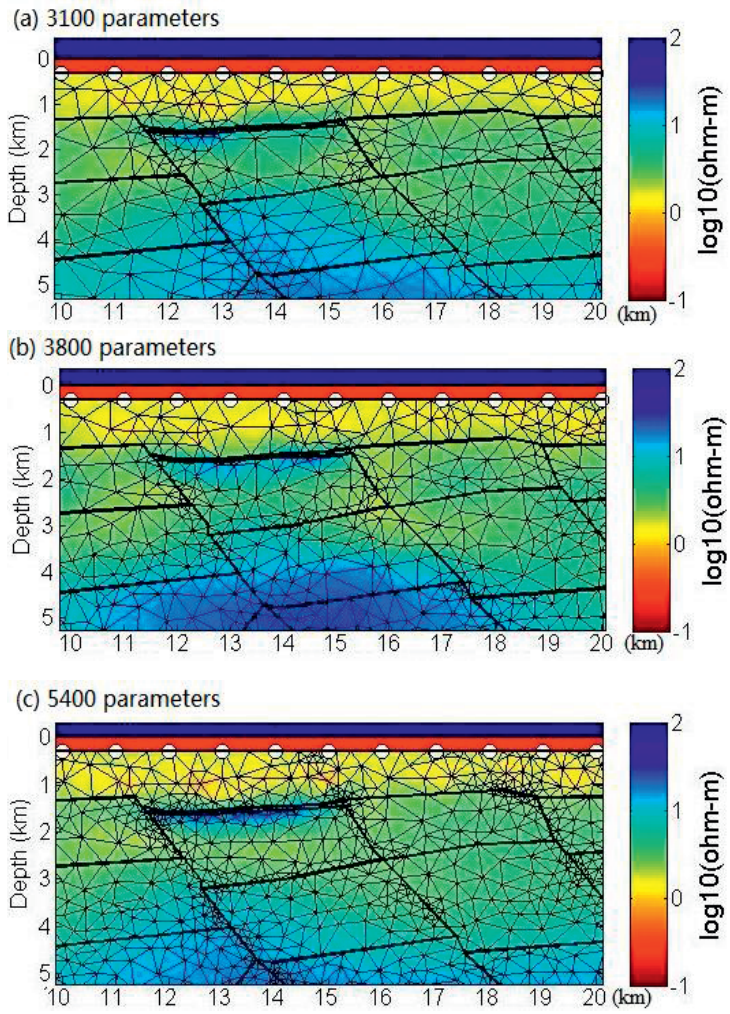

Figure 4.11. *CSEM inversion result by using IC sparse mesh, but with a different number of parameters. All the final RMS misfit of inversion is approximately 1.22. IC mesh is generated starting from (a) 750 vertices, (b) 500 vertices and (c) 1000 vertices.*

The resolution of the resistive image with IC mesh 500 is low, because of the weak reservoir anomaly. The underlying basement is strongly shown in the resistive image with the IC mesh 750. However, the estimated reservoir layer anomaly is too thick which is due to the large size of the cells. When the sparse mesh is too coarse, the resistive image loses the details of the anomaly. For computational cost comparison, the total time of

Occam's inversion for different meshes is illustrated in Figure 4.12. Apparently, the total time does not decrease too much with fewer parameters. The reason is that the computational time of the RS and the IC meshes is similar as illustrated in Figure 4.10. For the RS and the IC meshes, the cost is mainly for Jacobian matrix calculation. The sparse mesh reduces the cost by providing a fast model update. Therefore, the decreasing number of parameters does not reduce the computational cost a lot when both forward modelling and model updates have a small proportion of the total cost. The IC mesh 1000 has the similar cost as the IC mesh 750 and IC mesh 500.

The IC mesh is not able to reduce the Jacobian Matrix calculation cost. It will be indispensable to combine another method, for instance, the low-rank approximation (Amaya *et al.,* 2014), to reduce both the number of forward modellings and the memory requirements associated with storage of the Jacobian.

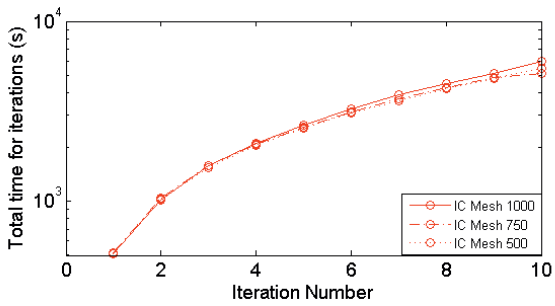

Figure 4.12. *The total time cost with CSEM data inversion iterations with the IC mesh 1000, 750, and 500.*

In order to test the horizontal resolution of the CSEM inversion by IC mesh, a model with two resistive reservoirs is used for generating synthetic data with a marine geophysical structure shown in Figure 4.1(a). The 2D resistive true model is shown in Figure 4.13(e). The 2D model consists of two resistive reservoirs (100 Ωm). The shallow reservoir is located between 11.5 km and 15.5 km in the *x* direction, and buried 1.5 km below the seafloor with 100 m thickness. The deep reservoir is located between 16 km and 19.5 km in the *x* direction, and buried approximate 2 km below the seafloor with 200 m thickness. The target is embedded into a homogeneous and isotropic conductive

layered background (1, 3, 5, 10 Ωm). The meshes for the inversion are the same as given in Figure 4.5. The inversion results of different triangle meshes are shown in Figure 4.13.

In all the Occam's inversion results, the anomalies consist of two different reservoirs. However, the horizontal resolution of Occam's inversion results by the IC mesh is not as high as the resistivity image by the RD mesh. The results from regular meshes have two low resistive artifacts below the reservoir anomaly. It is due to the shadowing of the overlying high-resistive anomaly. Both the shallow and deep anomalies are well recovered on the RD mesh. Since the anomalies are well recovered on the dense mesh, it is crucial to have a finer mesh in the vicinity of heterogeneity and coarser where the medium is more homogeneous for inversion. The coherence cube determines how the nodes are distributed in the space based on the imposed constraints. Compared with regular mesh and horizons constrained mesh, the IC mesh provides a smooth resistivity image, where the anomalies are constrained well by the structure.

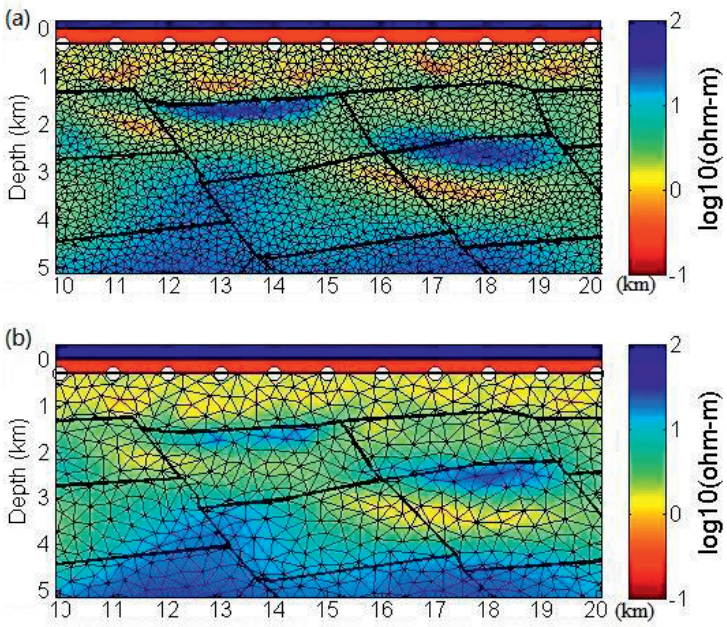

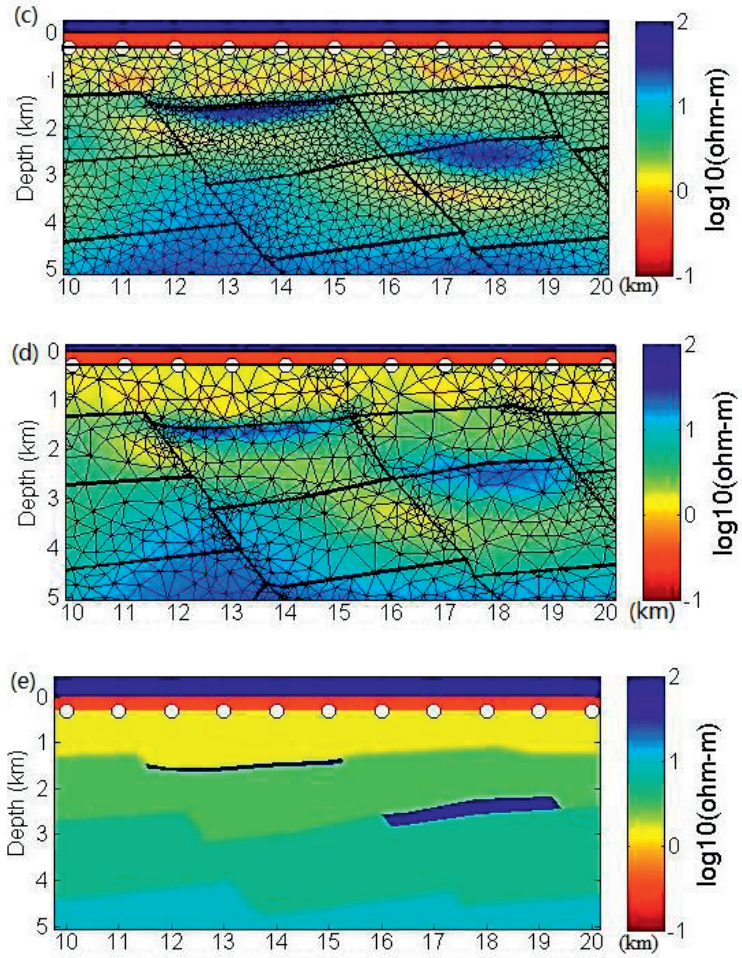

Figure 4.13. *CSEM inversion result by using (a) RD mesh, (b) RS mesh, (c) IH mesh, and (d) IC mesh. The final RMS is 1.14 for (b), 1.14 for (c), 1.15 for (d) and 1.14. (e) A true model of two reservoirs.*

The target RMS misfit is 1.20. The RMS misfits of Occam's inversion in different meshes are given for Figure 4.14. The RMS misfit is smaller than target misfit at the 8th iteration. All the RMS misfits of Occam's inversions reach the target misfit.

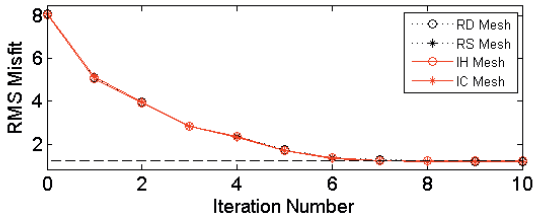

Figure 0.14. *RMS misfit varies with iterations in two resistors model with the RD, RS, IH, and IC mesh.*

The performances of the different mesh methods are listed in Table 4.2 for comparison.

Table 4.2 Comparison of the different meshes

Mesh	Resolution	Cost
RD	High	High
RS	Low	Low
IH	High	High
IC	High	Low

4.4. Discussion and Conclusion

Using synthetic data examples, we have tested the Occam's inversion on the four different meshes. The IC sparse mesh provides resolution as good as the RD mesh. Compared to the RS mesh, the IC sparse mesh shows a higher model resolution. However, the resolution is not as good as for the seismic approaches. This is due to the weakness of the electromagnetic exploration approach.

IC sparse mesh can reduce the computational cost while it keeps resolution as good as a fine regular mesh. Inversion using the IC sparse mesh provides a resistive image with good resolution at a much lower computational cost. This method can save time on model updates.

The total inversion time reduces by decreasing the number of unknown parameters. The IC sparse mesh reduces the computational cost of matrix operation for model updates. When the computational cost for model updates is a small proportion of the total time,

the total time tends to a constant when Jacobian matrix is the dominant proportion of the total cost, which is almost the same for the different IC sparse meshes.

The cost of the forward modelling is dependent on the number of nodes of the grid and the solution method of the forward problem. In this chapter, we use the same solver on the four different meshes. The main contribution to the difference of computational cost is the number of nodes.

The inverse resolution is dependent on the number of vertices extracted from the seismic coherence slice. This number is determined empirically and may be improved in further studies.

We have also shown that IC sparse mesh can support a good horizontal resolution for Occam's inversion. It can identify close resistors anomalies by Occam's inversion as good as the regular dense mesh.

We have demonstrated by synthetic examples that the resolution and computational cost for the IC sparse mesh offers a good compromise between spatial resolutions of the final solution and the computational cost. We have demonstrated that the IC sparse mesh is applicable to EM inversion. The use of this sparse mesh method to reduce the computational cost while keeping good resolution has been shown. The results show that the high computational cost of large-scale CSEM inverse problem can be significantly reduced by an IC sparse mesh.

Chapter 5 Image-guided regularized marine EM inversion

We introduce the generation of the irregular sparse mesh to reduce the computational cost. Based on this sparse mesh, we propose a regularization approach to enhance Occam's inversion. This regularization approach incorporates seismic constraints into EM inversion by using a non-Euclidean distance defined from the metric tensor field. The metric tensor field is computed not only from the seismic image but also from the stratigraphy image.

5.1. Introduction

During the past fifteen years, solutions to marine electromagnetic (EM) inverse problems have been rapidly and reliably developed for offshore exploration, as discussed in recent reviews (Constable, 2010; Key, 2012a). CSEM data have high sensitivity to resistive hydrocarbon fluids embedded in saline pore fluids. The inverse problem of finding a 3D model describing subsurface resistivity variations from CSEM data measured at surface is unfortunately ill-posed (McOwen, 1966). To stabilize the problem, regularization methods have been applied for various EM geophysics applications (Constable *et al*., 1987; Newman and Alumbaugh, 2000; Zhdanov *et al*., 2007; Abubakar *et al*., 2008, and Newman *et al*., 2010).

Regularization, in mathematics and statistics and particularly in the field of inverse problems, involves introducing additional information in order to solve the ill-posed problem or to prevent overfitting. A classic regularization example is the roughness penalty applied by Occam's inversion (Constable *et al*., 1987), which favors smooth models. Sometimes sharper and more focused models are preferred. Such models can be obtained by using norms other than L2 for penalizing the model gradients (de Groot-Hedlin and Constable, 2004; Hoversten *et al*., 2006; Hansen and Mittet, 2009).

The marine magnetotelluric (MT) method is applied for mapping the subsurface resistivity image by using naturally occurring low-frequency plane waves. The basis for MT method is found by Tikhonov (1950) and Cagniard (1953). The first equipment suitable for deep seafloor MT and CSEM soundings has developed by Charles Cox and Jean Filloux since the early 1960s (Constable and Cox, 1996). Although the marine MT

sounding has been developed by the academic since 1970s (the reviews by Constable, 1990; Baba, 2005), the marine MT method was first commercialized as a tool for mapping subsurface resistivity to complement the seismic method (Constable *et al*., 1998). The history of marine MT technique has been reviewed several times (Baba, 2005; Constable, 2010; Key, 2012a),

The EM data have a high sensitivity to highly resistive target, such as hydrocarbon reservoirs, embedded in low resistivity backgrounds. Moreover, the inverse resistivity image suffers from lower resolution than many seismic methods. Still, the ability to distinguish resistive targets from conductive surroundings makes the EM method an important tool for offshore exploration.

Combining the advantages of both EM and seismic data can improve interpretation based on each method alone. Based on the same geological structures of both seismic and EM models, joint inversion can be used to invert the data. But the joint inversion method normally has high computational cost.

Brown *et al*., (2012) proposed an alternative approach to joint inversion by boosting the vertical resolution of EM inversion algorithm using the better resolution of full waveform inversion (FWI). In their paper, Occam's inversion of EM data is constrained through the use of seismic velocity regularization weights. Similarly, Wiik *et al*., (2015) presented a Tikhonov type structural smoothing regularization approach that the marine CSEM inversion discretization conforms to the seismic information. Similarly, to incorporate a priori information, Bayesian methods have been applied in CSEM inversion (Ray and Key, 2012; Ray *et al*., 2014).

In image-guided interpolation, Hale (2009a, 2009b) provided a method to compute the tensor field and coherence from structure tensors of seismic image. He extracted the tensor for each pixel of the seismic image. These tensors present the amplitude and direction of the pixel. This approach has been applied for full waveform inversion of seismic data (Ma *et al*., 2012), where structural information was used to impose structural constraints in the inverse problem. The question is how this high resolution seismic image can effectively be incorporated into an EM inversion.

Zhou *et al*. (2014a, 2014b) inverted the electrical resistivity data by using image-guided Gauss-Newton inversion method. This approach extracted the structural information from the guiding image (GPR section) and incorporated to the direct current (DC) resistivity data. In Zhou *et al*. (2014a, 2014b), the structural information is assumed to be perfectly known. Stochastic image-guided structure-constrained inversion approach was developed by Zhou *et al*. (2016), in which the structural information could be updated by Markov-chain Monte Carlo (MCMC) sampler and the adaptive metropolis algorithm (AMA).

We have employed the tensors for mesh generation for the EM inversion. A coherence-based irregular sparse mesh has been generated for EM inversion based on vertices and segments from seismic coherence (Guo and Dong, 2015; Guo *et al*., 2016). Therefore, the coherence-based irregular sparse mesh can support a high horizontal resolution for Occam's inversion. It can identify close resistive anomalies by Occam's inversion as good as the regular dense mesh. The regularization is still of a smoothing nature, but it can be improved by incorporating structural information from seismic data.

In this chapter, we develop an approach to improve the results for the structural sparse mesh by a structural smoothing regularization. The structural sparse mesh is generated by using a coherence-guided irregular method. This regularization approach incorporates seismic constraints into EM inversion by using a non-Euclidean distance defined from the metric tensor field. The metric tensor field is computed not only from the seismic image but also from the stratigraphy image. Due to the uncertainty in seismic interpretation, the impact of seismically derived structure in the inversion result was not investigated, which can potentially introduce a bias in the result. In this way, some of the low vertical and horizontal resolution of EM data can be improved by this constraint. In order to do this, the non-Euclidean distance replaces the space distance between the neighbor parameters. The parameters do not vary much along the geological features; however, it allows a large difference between the neighbor parameters across the features. When the spatial distance is replaced by the smaller value non-Euclidean distance, the new model weight is larger than the old model weight. Therefore, the regularization will smooth the model along the features. For each cell, neighbor cell along the features supports a large model weight.

We develop both the coherence-based irregular sparse mesh and image-guided regularization methods. These methods are applied on synthetic datasets of both marine CSEM and magnetotelluric (MT) cases and real datasets of marine CSEM in the Troll area (Gabrielsen *et al*., 2009). For the marine CSEM and MT synthetic datasets cases, the inversions are tested not only separately but also jointly. The image-guided regularization method presented in this thesis is an easy tool that can be used to the existing inversion methods.

5.2. Regularization inverse problem

We introduce the image guided regularization concept by showing the application in CSEM Occam's inversion algorithm. Occam's inversion searches the minimization of the following unconstrained regularized objective function, which is given in Equation (2.52). This objective function includes two terms. The first term is called data misfit, where the expression is given by equation (2.53); the second term is the regularization term given by equation (2.56).

$$\phi_m = \|\boldsymbol{Rm}\|^2 + \left\|\boldsymbol{P}(\boldsymbol{m} - \boldsymbol{m_{ref}})\right\|^2, \tag{5.1}$$

The first term, model roughness, is computed by applying an operator $\boldsymbol{R}$ to the elements of the model vector $\boldsymbol{m}$. Concerning models here, $\boldsymbol{m}$ is a vector of the logarithm to the base 10 of the conductivity for each parameter, and $\boldsymbol{R}$ is chosen to be a matrix calculated by the model differences between parameter cell and the neighboring cells which have the same edges or nodes. The second term is a measure of the difference of **m** from a priori preference model $\boldsymbol{m_{ref}}$. The diagonal matrix $\boldsymbol{P}$ contains scaling parameters that determine the relative weighting between the preference and the model roughness.

The normal model roughness regularization $\|\boldsymbol{Rm}\|^2$ in Occam's inversion is dependent on the finite parameter area, and the spatial distance between the given parameter and the surrounding parameters. In the discrete problem, the roughness penalty is given as following:

$$\|\boldsymbol{Rm}\|^2 = \sum_{i=1}^{np}\sum_{j=1}^{nb}\frac{A_j}{A_{sum}}\left(\frac{\Delta m_{ij}}{\Delta r_{ij}}\right)^2, \tag{5.2}$$

where *np* is the number of free parameters; *nb* is the number of neighbor cells; A_j is the area of the neighboring cell; A_{sum} is the sum of areas of the neighboring cells; Δr_{ij} is the distance between the centroid of a center cell and the centroid of adjacent cells; and Δm_{ij} is the parameter difference of the center cell with the adjacent cell.

However, in many cases the smooth inversion models are insufficient for interpretation of marine CSEM data when the geological structure is expected to vary sharply. From the seismic image, a non-Euclidean distance can be defined by a metric tensor field.

5.3. Image-guided regularization inversion

In this section, we present the methodology of the image-guided regularization of Occam's inversion. Firstly, we introduce the structure tensor and metric tensor fields from a guiding image. Then, we build an irregular mesh by using coherence-based sparse mesh method as the mesh of the starting model of EM inversion. Finally, we modify the smooth regularization term by using the non-Euclidean distance.

5.3.1. The structure tensor fields and the metric tensor fields

The structure tensors can be computed from an image for instance given the grey map (Guo and Dong, 2015). Each pixel in the grey image ranges from 0 for white to 1 for black. This tensor has been developed in the image processing (Weickert, 1999; Köthe, 2003; Fehmers and Höcker, 2003; Baghaie and Yu, 2015). Given an image I(x; z), the structure tensor is based on the gradient of I, which is usually defined as:

$$S_\sigma = \begin{bmatrix} I_x^2 * G_\sigma & I_x I_y * G_\sigma \\ I_y I_x * G_\sigma & I_y^2 * G_\sigma \end{bmatrix} = \begin{bmatrix} S_{xx} & S_{xy} \\ S_{xy} & S_{yy} \end{bmatrix}, \tag{5.3}$$

where $*$ denotes convolution; G_σ is a Gaussian function with standard deviation σ as shown in equation (5.4), and $I_x$and I_y are horizontal and vertical components of gradient vector at each pixel respectively.

$$G_\sigma(x, y) = \frac{1}{2\pi\sigma^2} e^{-\frac{x^2+y^2}{2\sigma^2}}, \tag{5.4}$$

The orientations of the image features are provided by the eigenvalue and eigenvector decompositions of the structure tensor. The eigenvalue and eigenvector decompositions are given by Fehmers and Höcker (2003),

$$S_\sigma = \lambda_1 \boldsymbol{u}\boldsymbol{u}^T + \lambda_2 \boldsymbol{v}\boldsymbol{v}^T, \tag{5.5}$$

where $\lambda_1$and λ_2 denote the eigenvalues; $\boldsymbol{u}$ and $\boldsymbol{v}$ denote the corresponding eigenvectors of the symmetric and positive semi-definite matrix S_σ. $d_1 = \lambda_1^{-2}$; $d_2 = \lambda_2^{-2}$; d_1 and d_2 are the "semi-minor" and "semi-major" axes of the ellipse. Vectors e_1 and e_2 represent the prescribed directions of the tensor. The two eigenvectors are calculated as:

$$\lambda_1 = \frac{1}{2}(S_{yy} + S_{xx} - \sqrt{(S_{yy} - S_{xx})^2 + 4S_{xy}^2}), \tag{5.6}$$

$$\lambda_2 = \frac{1}{2}(S_{yy} + S_{xx} + \sqrt{(S_{yy} - S_{xx})^2 + 4S_{xy}^2}), \tag{5.7}$$

Obviously, the eigenvalue λ_1 is smaller than λ_2. The tensor geometry is shown by Figure 5.1.

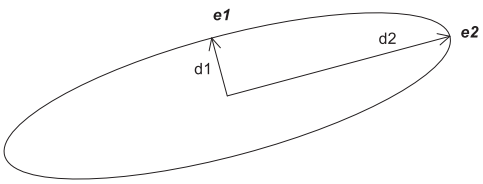

Figure 5.1. *Geometric interpretation of a structure tensor.*

Three types of areas in the image can be defined from the eigenvalues, which are calculated from location structure tensors (Tchon *et al.*, 2006). These are flat regions ($\lambda_2 \approx \lambda_1 \approx 0$), edges ($\lambda_2 \gg \lambda_1 \approx 0$) and corners ($\lambda_2 \approx \lambda_1 \gg 0$).

The relative difference between the two eigenvalues of S_σ is an indicator of the degree of gradient anisotropy, which shows how strongly it is biased to a particular direction. This attribute can be quantified by the coherence defined as:

$$c = \frac{(\lambda_1 - \lambda_2)^2}{(\lambda_1 + \lambda_2)^2}. \tag{5.8}$$

A simple example of structure tensors field and metric tensors field is given in Figure 5.2.

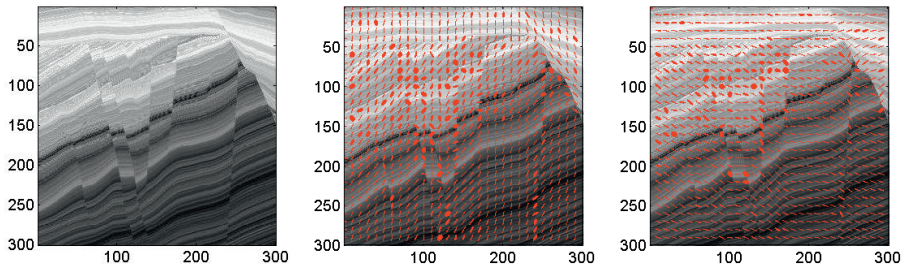

Figure 5.2. *Seismic image (left), structure tensors field (middle), and metric tensors field (right). Red ellipses represent tensors.*

5.3.2. Coherence-based sparse mesh

The seismic coherence section can improve the vertical resolution of the seismic image. Seismic coherence has been applied to build irregular sparse mesh for EM inversion (Guo and Dong, 2015). This sparse grid is generated by Delaunay Triangulation based on the nodes and segments. The nodes are extracted by Harris corner detection method (Harris and Stephens, 1988) based on seismic coherence section. The segments, horizons and faults, are picked from the seismic image.

5.3.3. Image-guided regularization

The non-Euclidean distance $\hat{r}$ is given by the equation:

$$\nabla\hat{r}(x) \cdot D(x)\nabla\hat{r}(x) = r_{ij}^2, \tag{5.9}$$

where $\hat{r}(x)$ means the minimum non-Euclidean distance from centroid of a center element to centroid of neighboring cells; $D(x)$ is a metric tensor field from a seismic image (Hale, 2009a); and the spatial distance r_{ij} is between centroid of a center element and centroid of adjacent cells.

The metric tensor field $D(x)$ is computed by the structure tensor $S(x)$ and the coherence $c(x)$ as given below (Hale, 2009a):

$$D(x) = \frac{S^{-1}(x)}{1-c(x)}, \tag{5.10}$$

where $0 \leq c(x) < 1$ and is calculated from equation (5.8). In this function, the eigenvalues of the metric tensors are the reciprocal of the structure tensors. The eigenvectors of the metric tensors are the same as the structure tensors. This means that the eigenvectors parallel to the structure exhibit big eigenvalues, whereas those perpendicular to the reflections are small. This encourages diffusion of the seismic amplitude in the direction along the reflection, because diffusion in the direction perpendicular to the reflection would destroy the reflections.

We now modify the regularizing term $\|\boldsymbol{Rm}\|^2$. We replace the spatial distance in equation (5.2) by the non-Euclidean distance $\hat{r}_{ij}$ from equation (5.9). Then, the roughness penalty is given as:

$$\|\boldsymbol{Rm}\|^2 = \sum_{i=1}^{np} \sum_{j=1}^{nb} \frac{A_j}{A_{sum}} \left(\frac{\Delta m_{ij}}{\Delta \hat{r}_{ij}} \right)^2, \tag{5.11}$$

where $\Delta \hat{r}_{ij}$ is the non-Euclidean distance from adjacent cell j to the center cell i.

It is important to find the centroid of the cell at the pixel in the seismic image. The centroid of the cell has the same metric tensor as this pixel. In order to modify the regularization rapidly and efficiently, we find the interfaces of the stratigraphy, which are the horizons and faults in the irregular sparse mesh. Then the cells with the vertices on the interfaces should have different non-Euclidean distance to the neighbors, if they belong to different layers. At the end, we modify the smooth regularization by using this non-Euclidean distance.

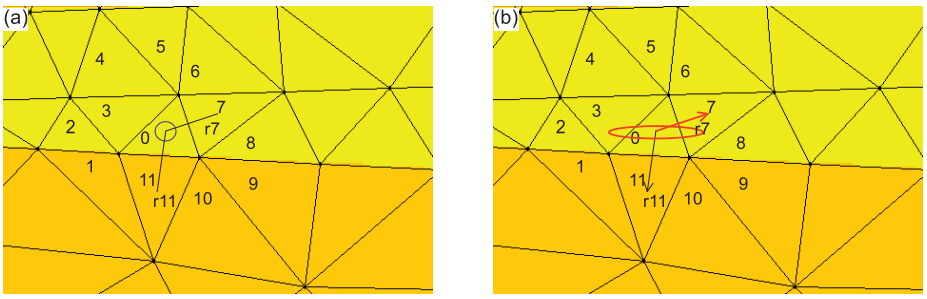

Figure 5.3. *Roughness calculated by (a) spatial distance; (b) non-Euclidean distance. "arrow" represents the non-Euclidean distance with the direction of the metric tensor (ellipse).*

The advantage of the non-Euclidean distance is that it is related to the tensor field which contains the direction of the feature. The difference of spatial distance and non-Euclidean distance is shown in Figure 5.3. In Figure 5.3(b), the cell '0' is much closer to cell '7' than cell '11'. In Figure 5.3(a), the spatial distance of r_7 is almost the same to r_{11}.

5.4. Results

In this section, we demonstrate the performance of image-guided regularization with resistivity synthetic model studies that are illustrative of offshore hydrocarbon exploration problems. The resistivity model is the same as in Key (2012b), which is shown in Figure 5.4. The resistivity values in each layer are given in Table 5.1. The isotropic model consists of sloping seafloor, conductive sediments, and a thick tabular resistor representing a salt layer, a thin resistive hydrocarbon reservoir and an underlying resistive basement.

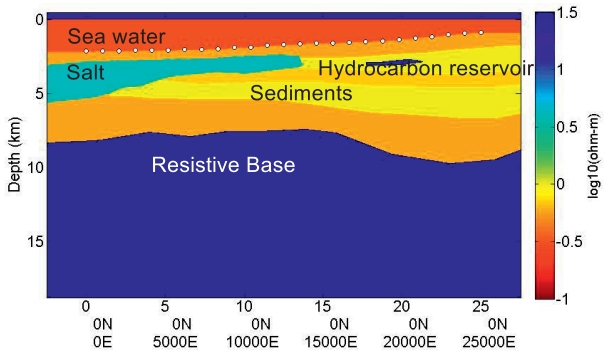

Figure 5.4. *Reproduced from (Key, 2012b). The synthetic model consisting of sloping seafloor bathymetry, conductive sediments, and a thick tabular resistor representing a salt layer, a thin resistive hydrocarbon reservoir and an underlying resistive basement. The white dots are the receivers' locations with 1.32 km spacing.*

Table 5.1 Model parameters for the synthetic model.

layer	R(Ωm)
Air	10^{13}
Sea water	0.3
Salt	4

Sediment (brown)	0.6
Sediment (yellow)	1
Basement	100
Reservoir	50

2D synthetic inline electric field CSEM data were measured for 50 horizontal electric dipole (HED) source and 20 receivers at both 0.25 and 0.75 Hz by applying 4% Gaussian noise. The data were removed below a 10^{-15}V/Am^2 noise floor. Moreover, 2D synthetic inline MT data were calculated at 20 receivers for 21 frequencies from 0.001 to 1 Hz, with a noise floor at 10^{-15}V/Am^2 and 4% Gaussian noise added to the synthetic data.

It is assumed that the seismic model and resistivity model have the same geological features. We compare results of regularized inversion performed with the following meshes. The inversion mesh is generated by MARE2DEM code (Key, 2012). The finite element meshes are generated and refined by using the Delaunay triangulations method (Shewchuk, 1996). Inversion models are constructed by Matlab graphical model design tools, which can import topographic interfaces and other known surfaces. The starting model has a constant value of 1 Ωm below the seafloor. The mesh of starting model is generated by MARE2DEM code. These EM data inversion tests are run on 5 nodes with 16 cores each of the Intel Sandy Bridge E5-2670 (2.6GHz) cluster.

In order to present the improvement of the image-guided regularization inversion, some experiments are introduced in the following, which are given in Table 5.2. All the inversions fit to a root mean squared (rms) misfit of 1.0.

Table 5.2. Cases for the different meshes and regularizations

Synthetic examples	Mesh	Regularization
Case 1(Figure 5.5)	Regular dense mesh	Normal regularization
Case 2(Figure 5.7)	Regular sparse mesh	Normal regularization
Case 3(Figure 5.9)	Irregular sparse mesh	Normal regularization
Case 4(Figure 5.11)	Irregular sparse mesh	Image-guided regularization
Case 5(Figure 5.13)	Irregular dense mesh	Image-guided regularization

5.4.1. Case in normal regularization and normal mesh

In this case, we present Occam's inversion results of marine EM data using the traditional method. The marine CSEM and MT synthetic data are simulated by the

MARE2DEM code with the true model shown in Figure 5.4. The mesh of the starting model is generated as an unstructured isotropic dense mesh shown in Figure 5.5(a). In order to clearly illustrate the results, logarithmic color scale from -1 to 1.5 was used for only plotting purpose.

Figure 5.5(b) illustrates Occam's inversion results with fine regular mesh and traditional smooth regularization from the CSEM data. The final RMS misfit is 0.90 smaller than the target misfit 1.0 (Figure 5.6). The resistive model is smoothed in both horizontal and vertical directions. It can image a thick tabular resistor anomaly as salt layer. There is also a strong anomaly representing the shallow resistive hydrocarbon reservoir.

Marine MT image has good resolution for the deep targets. Figure 5.5(c) shows the inversion result traditional regularization with a fine regular mesh in Figure 5.5(a). In the shallow area, the hydrocarbon reservoir is undetectable, and only a weak anomaly is shown as the thick anomaly of salt layer. The strong anomaly of underlying resistive basement is shown as a flat layer.

The results of joint inversion of CSEM and MT data have high resolution in both shallow and deep area compared to both CSEM and MT methods. Figure 5.5(d) shows the normal smooth regularization inversion result with fine regular dense mesh. In Figure 5.5(d), the inverted resistivity results have high resolution at both the shallow and deep area. The resistive reservoir and thick layer of salt layer at the shallow area are interpretable. The underlying resistive basement can be detected by the joint inversion.

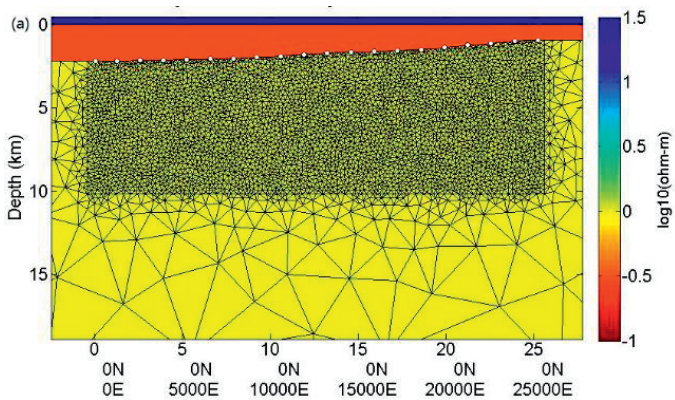

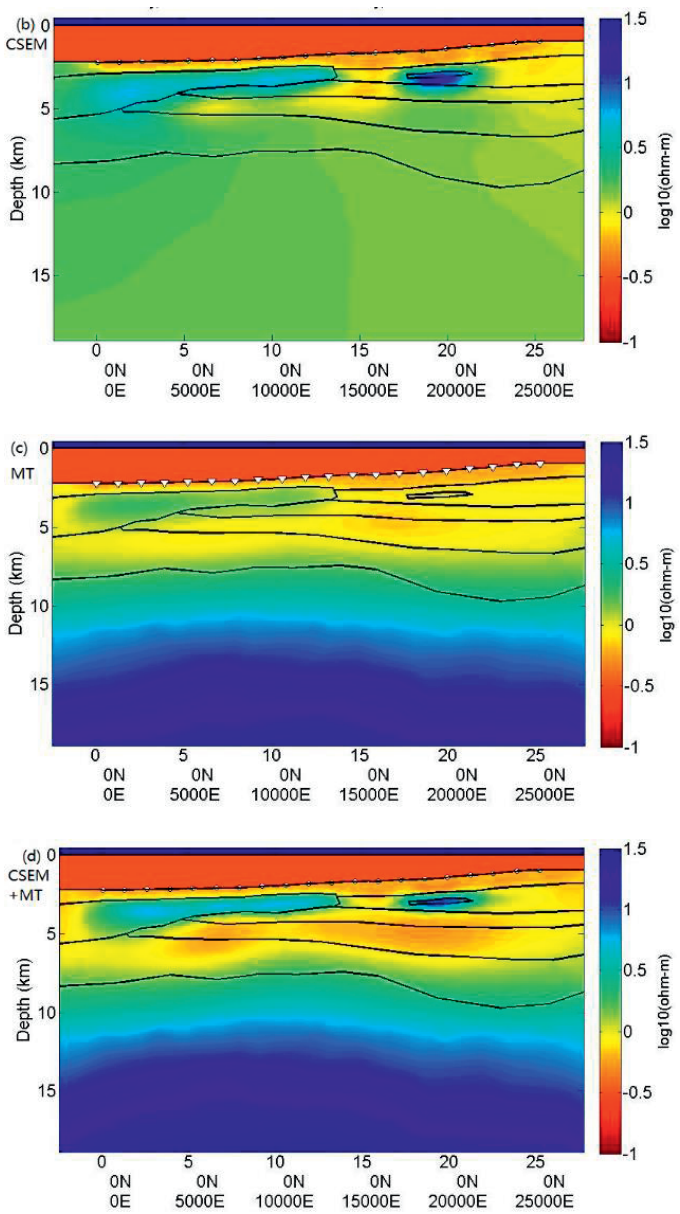

Figure 5.5. *(a). Fine regular dense mesh consists of 8500 free parameters for Occam's inversion. The results are the inversion of (b) CSEM data, (c) MT data and (d) joint inversion of CSEM and MT data.*

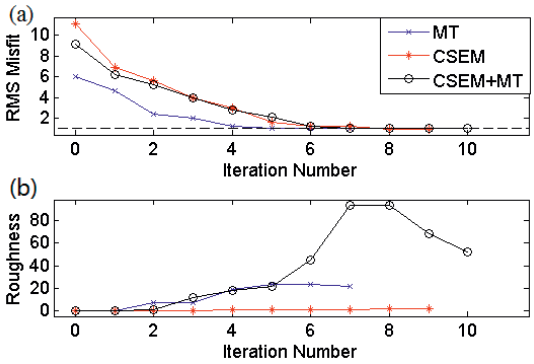

Figure 5.6. *The (a) rms misfit and (b) roughness with iterations for the inversion with regular dense mesh and smooth regularization.*

5.4.2. Case in normal regularization and sparse mesh

In order to reduce the computational cost and physical memory, a sparse mesh is used to reduce the number of parameters. We give an example where the number of parameters is 1700 and the regular isotropic sparse mesh is shown in Figure 5.7(a). The true resistivity model employed for this test is shown in Figure 5.4. The inversion results with fewer parameters describe the model shown in Figures 5.7(b), 5.7(c), and 5.7(d) for CSEM data, MT data and joint inversion of both CSEM and MT data, respectively.

The results shown in Figure 5.7 are not as quantitative as those shown in Figure 5.5. The rms misfit and roughness are shown in Figure 5.8.

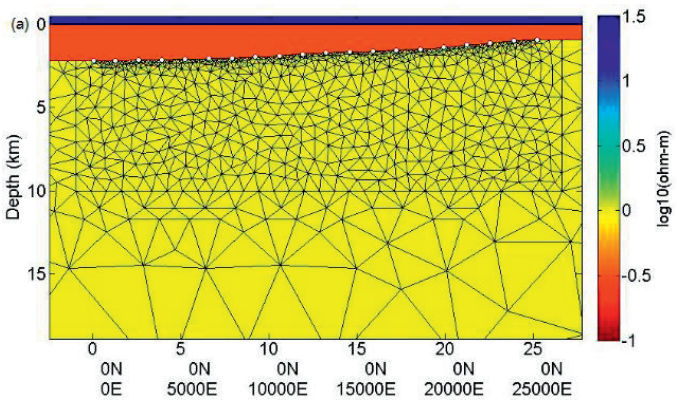

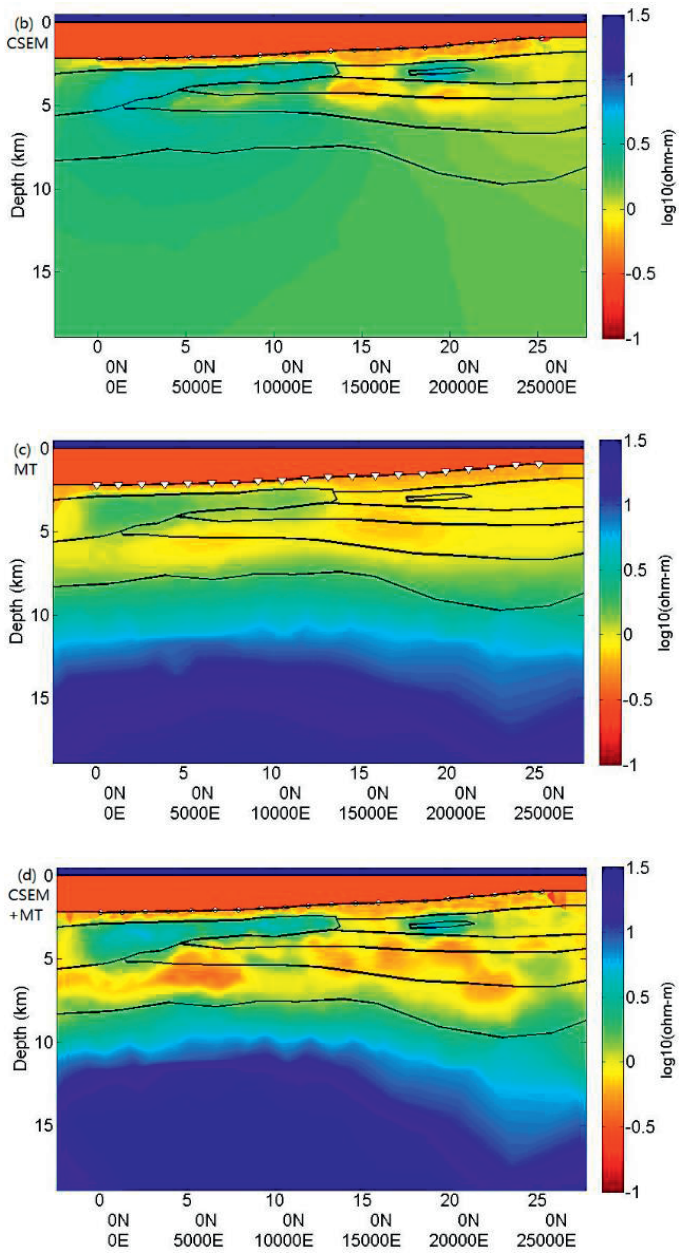

Figure 5.7. *(a). Regular sparse mesh for Occam's inversion. The results are the inversion of (b) CSEM data, (c) MT data and (d) joint inversion of CSEM and MT data.*

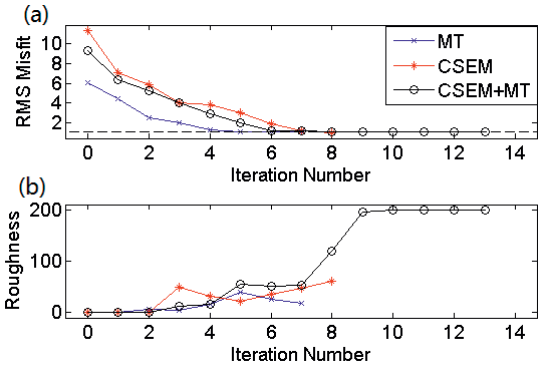

Figure 5.8. *The (a) rms misfit and (b) roughness with iterations for the inversion with regular sparse mesh and smooth regularization.*

In order to improve the qualified resistivity image with a sparse mesh, the coherence-based irregular sparse mesh is applied to invert the marine EM data. The results are shown in Figure 5.9.

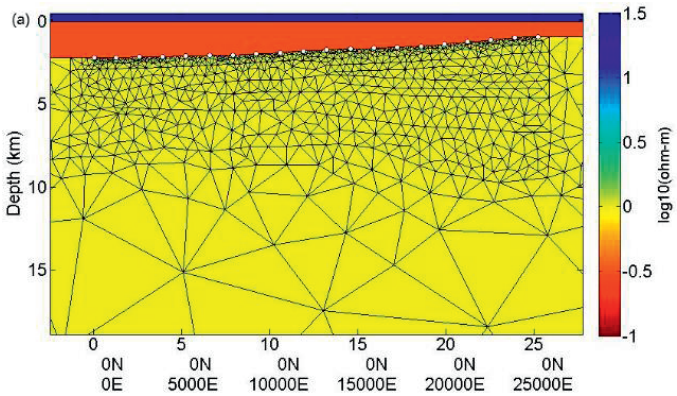

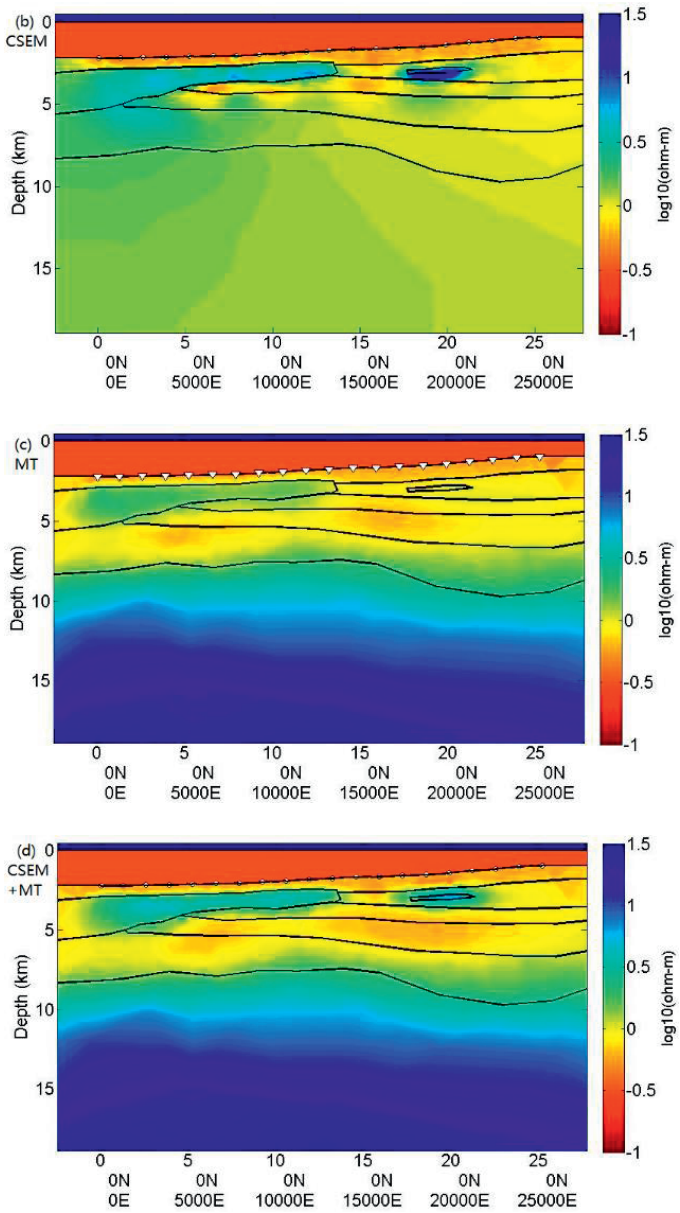

Figure 5.9. *(a). Irregular sparse mesh for Occam's inversion. The results are the inversion of (b) CSEM data, (c) MT data and (d) joint inversion of CSEM and MT data.*

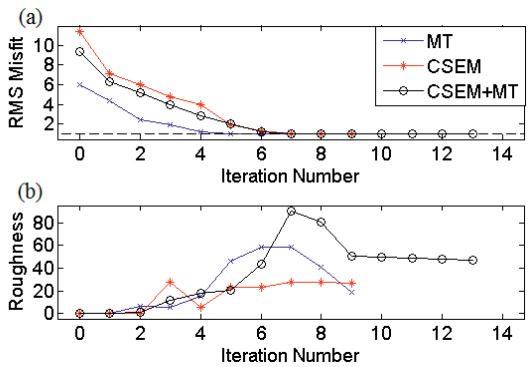

Figure 5.10. *The (a) rms misfit and (b) roughness with iterations for the inversion with irregular sparse mesh and smooth regularization.*

Compared to the traditional regular dense mesh, the inversion with irregular sparse mesh can provide a similar resistivity image with fewer parameters (Figure 5.9). In Figure 5.9(b), the resistivity image of marine CSEM inversion has a more clearly delineated boundary of the salt layer.

Figures 5.9(c) and 5.9(d) illustrate the CSEM data inversion results with the same sparse starting model for MT data inversion and joint inversion of CSEM and MT data. The conductive layer below the salt layer is clearly shown. Compared to Figure 5.7(c), the anomaly of underlying resistive basement has been improved in Figure 5.9(c).

5.4.3. Case in image-guided regularization and irregular mesh

The coherence-based irregular sparse mesh incorporates seismic structure into the EM inversion. However, the EM inversion can still be improved by image-guided regularization. Using the image-guided regularized inversion, the result is shown in Figure 5.11. The true model employed is the same as above in Figure 5.4. The mesh of the starting model is the same as the irregular sparse mesh (Figure 5.9(a)). The rms misfit and roughness are shown in Figure 5.12.

Figure 5.11(b) shows image-guided regularized inversion result of CSEM data. Both Figures 5.9(b) and 5.11(b) provide a strong anomaly of hydrocarbon reservoir. But the resistivity image from the image-guided regularized inversion has a strong thick anomaly of the salt layer in Figure 5.11(b). The boundary of the thick anomaly is much

clearer than shown in Figure 5.9(b). The bottom of the salt layer is constrained by the image-guided regularization in Figure 5.11(b). The conductive layer is also detected below the salt layer anomaly, where the amplitude of the anomaly is more correct than the result from the traditional smooth regularization. The image-guided regularization method provides an apparent boundary of the salt layer anomaly.

Compared the traditional smooth regularized inversion, the improvements do not only come from the irregular mesh but also the image-guided regularization. Figure 5.11(b) provides a resistivity image which is similar to the resistivity image inverted with the irregular mesh shown in Figure 5.9(b). The reason is that the mesh of the starting model in Figure 5.11(b) includes the geological features and the model is smoothed following the feature direction by the image-guided regularization. The difference between the salt layer and sediment layer is stronger in Figure 5.11(b). The image-guided regularized inversion provide a larger roughness for the salt anomaly boundary.

In Figure 5.11(c), the resistivity image is from the MT data inversion. A conductive sediment layer is located at 4 km depth below the surface, which is accordance to the true model shown in Figure 5.4. A weak anomaly of hydrocarbon reservoir is also detected by MT data. Moreover, the anomalies of the salt layer and the underlying resistive basement are clear and irregular following the horizons in Figure 5.11(c).

Apparently, the image-guided regularization provides a smooth model in horizontal direction. The joint inversion results combine the advantages of both CSEM and MT data, which have good resolution in both shallow and deep areas in Figure 5.11(d).

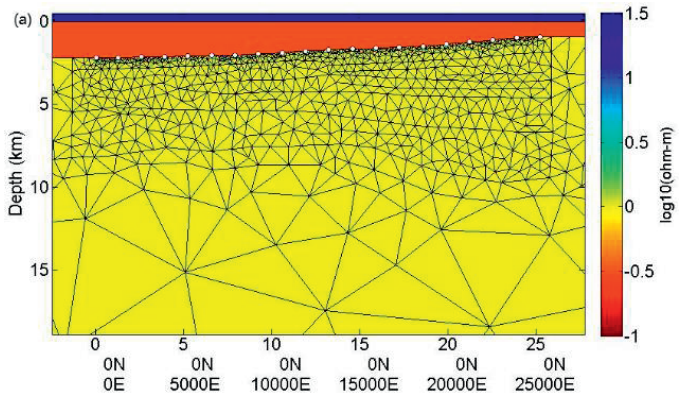

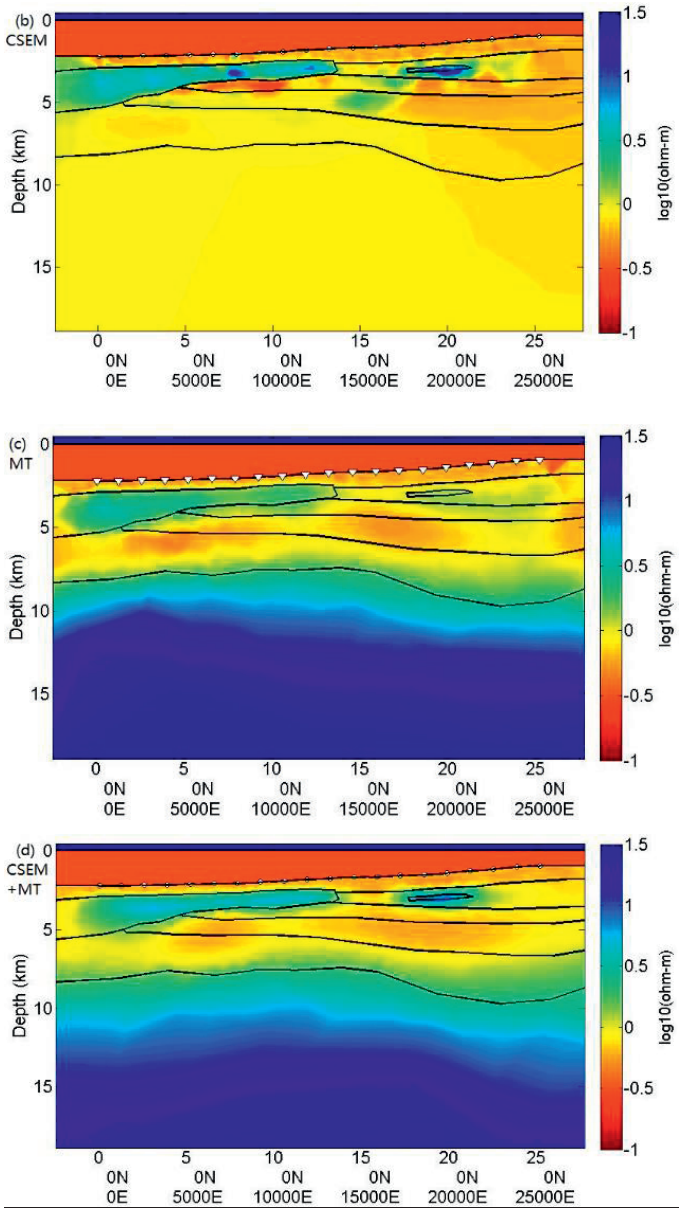

Figure 5.11. *(a). Irregular sparse mesh for image-guided regularized inversion. The results are the image-guided regularized inversion of (b) CSEM data, (c) MT data and (d) joint inversion of CSEM and MT data.*

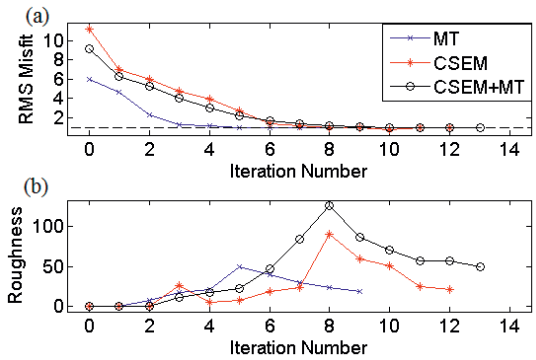

Figure 5.12. *The (a) rms misfit and (b) roughness with iterations for the inversion with irregular sparse mesh and image-guided regularization.*

Compared these three cases, the image-guided regularization algorithm promotes the resolution of the EM data inversion. In summary, there are two different aspects to incorporate this high resolution seismic image into an EM inversion. The mesh of the starting model is generated by coherence-based irregular sparse mesh method. On the other hand, the model parameters are penalized by seismic image-guided regularization algorithm. In order to figure out how the image-guided regularization inversion method works, we test one more model with the dense starting mesh.

The true model is the same as above. Figure 5.13 shows both of the traditional and image-guided regularization with the same mesh. A synthetic test for MT data inversion is performed with these two regularization method. The starting model employs an irregular dense mesh as shown in Figure 5.13(a). Figure 5.13(b) illustrates the Occam's inversion result with traditional regularization. Although the resistivity map can illustrate the underlying resistive basement, the anomaly is not as good as it shown in Figure 5.13(c).

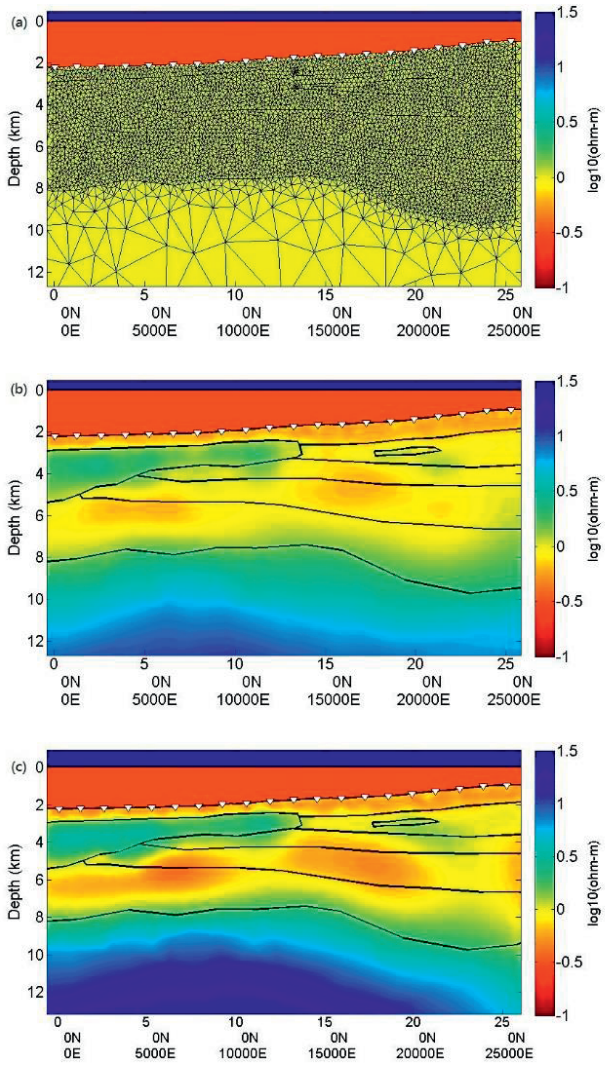

Figure 5.13. *(a) Irregular dense mesh for MT data inversion. The result of MT data inversion with (b) traditional regularization and (c) image-guided regularization.*

5.4.4. Real data example

The real data set was measured over the Troll West Oil Province (TWOP) in 2008 in the Norwegian North Sea (Gabrielsen *et al*. 2009; Morten *et al*. 2012). The map view of the TWOP is shown in Figure 2 in Morten *et al*. (2012). These inline data were inverted on the frequencies of 0.25, 0.75, 1.25 and 1.75 Hz. The horizons are used to make the

geometry image to constrain the inversion. The initial anisotropic half-space model shown in Figure 5.14 with the main geological. Both the horizontal and vertical resistivities of the half-space are set as 1 Ωm.

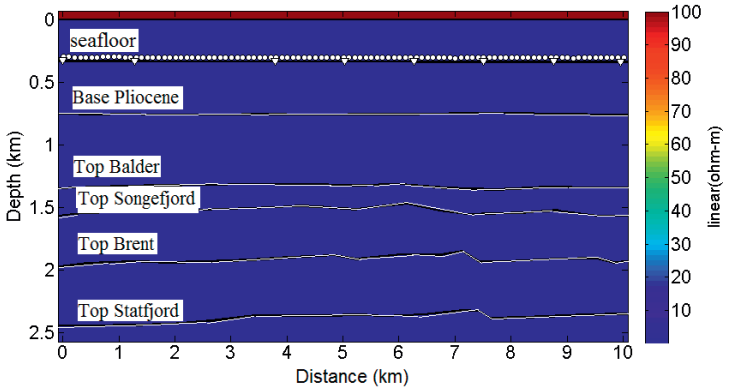

Figure 5.14. *Initial model for the 2008 Troll data set with the horizons. The triangles located on the sea floor indicate the receiver locations.*

Figures 5.15 and 5.16 show the inversion results with the normal smooth regularization and image-guided regularization using inline CSEM data, respectively. Figure 5.15(a) and 5.15(b) are the vertical and horizontal resistivity images, respectively. Apparently, we observe two clear anomalies between approximately 1300 m and 1500 m depth in the vertical resistivity image. These anomalies locate between 2 km and 3 km (left), 4 km and 5 km (right), respectively. The left anomaly is stronger than the right. Both of the two anomalies are cross the top Balder horizon.

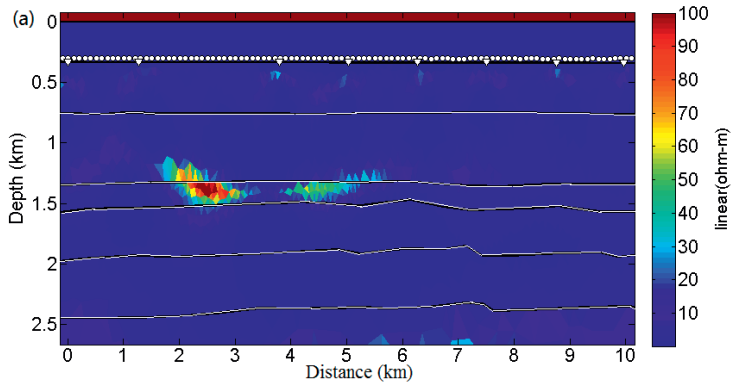

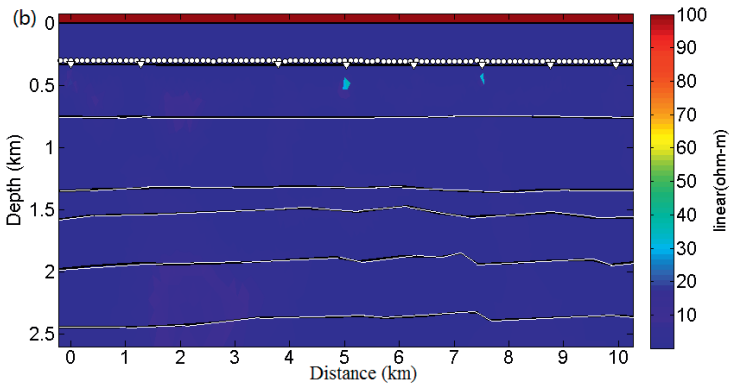

Figure 5.15. *Inversion results using normal smooth regularization for the 2008 Troll data set. Triangles denote the receiver positions; white notes are the shots of transmitters. (a) Vertical resistivity, (b) Horizontal resistivity.*

Similarly, Figures 5.16(a) and 5.16(b) are the vertical and horizontal resistivity image, respectively. We observe two clear anomalies between the top Balder and top Songefjord horizons. The depths are approximately between 1300 m and 1500 m. In Figure 5.16, both anomalies are stronger than those shown in Figure 5.15. Obviously, the inverted resistivity image follows the geometry dictated by the seismic horizons. By comparing Figures 5.15(a) and 5.16(a), the results of image-guided regularization have some changes.

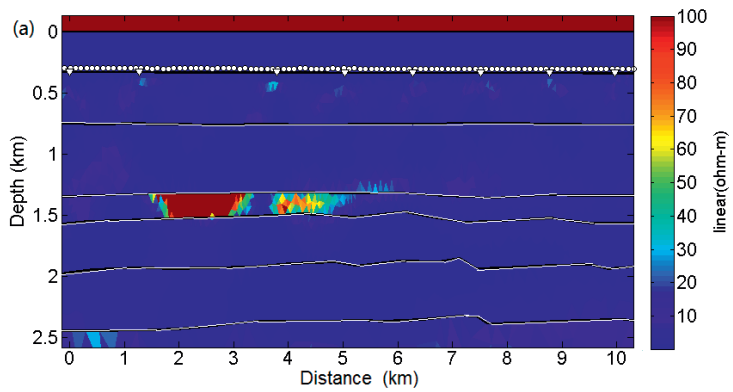

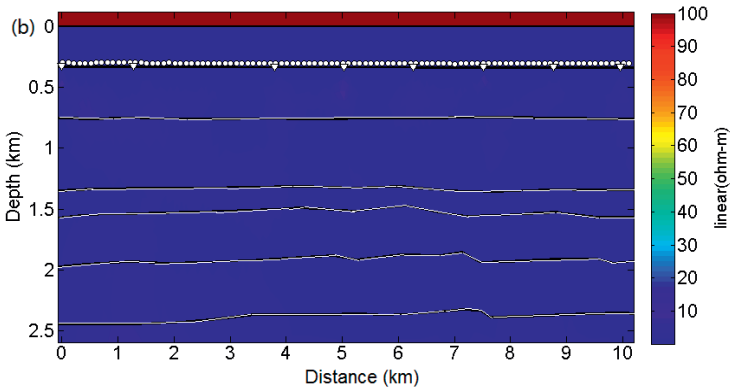

Figure 5.16. *Inversion results using image-guided regularization for the 2008 Troll data set. Triangles denote the receiver positions; white notes are the shots of transmitters. (a) Vertical resistivity, (b) Horizontal resistivity.*

The RMS misfit and roughness for the different regularization inversions are shown in Figure 5.17. The convergence for the two regularization inversions has similar rate. The image-guided regularization has an increasing roughness.

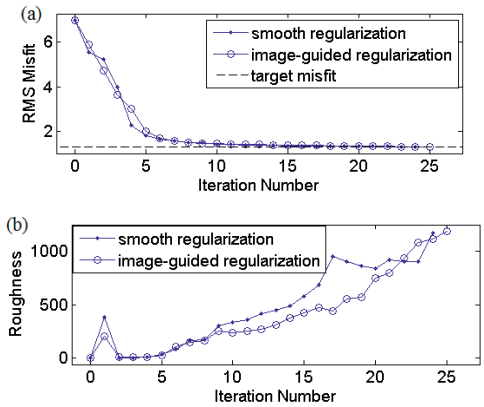

Figure 0.17. *(a) RMS misfit and (b) Roughness for the two different regularizations inversions.*

5.5. Discussion

We have demonstrated that the image-guided regularization method is applicable to Occam's inversion. It works on both the CSEM and MT data inversion. We use the non-Euclidean distance to replace the space distance. Therefore, the model weight is

changing with the features. This method has considered regularization operators that penalize the L2 norm of the spatial derivatives, smoothing models with sharply and focused varying features.

We improve Occam's inversion in two steps. Firstly, we replace the regular mesh by irregular sparse mesh. This irregular sparse mesh can reduce the computational cost. Secondly, we regularize the irregular mesh by using an image-guided regularization method. The results show that the image-guided regularization can provide an approach to constrain the EM inversion by geological features. It can be applied to salt layer boundary detection.

Compared with the seismic regularization method to incorporate seismic velocity into EM inversion (Brown *et al.,* 2012), the major advantage of image-guided regularization method can be applied to 2D or 3D modelling. The seismic regularization provides a method for incorporating seismic structure into EM inversion but avoids the joint inversion method.

Image-guided inversion of electrical resistivity data is developed for DC resistivity data by Zhou *et al. (2014).* The image-guided interpolation approach is applied to focus a smooth resistivity image along four-direction smoothing matrix by model weights. Since the method is applied in a rectangle mesh, the four-direction is following 0, 45, 90, and 135 degrees directions of the neighboring cells. However, the image-guided regularization method in this thesis may consider any directions.

This method also has some limitation and it assumes that the seismic data and EM data have the same structural features. It is difficult to find the boundary of the fine-scale layering using this method due to the low sensitivity. It works best for the situations where the boundaries of resistivity and image features change at the same depth.

5.6. Conclusion

In this chapter, we have developed a simple method for combining structural constraints into EM inversion by using image-guided regularization weights. The image-guided regularization scheme was tested on 2D inline synthetic marine CSEM and MT data to demonstrate how the results fit with the geological structures. The complex model

for these tests is 2D isotropic, with both conductive and resistive features. This approach is an alternative to traditional regularization, where models that are structurally conformed to geological features or seismic data can be found. The inverted resistivity model follows the features more closely. The anomalies are not across the interfaces. The amplitude of the anomaly is closer to the true model than the traditional regularized inversion. This will aid the interpreters when dealing with results from marine EM inversion.

We have also applied the image-guided regularization method on the marine CSEM inversion for the real data set (TWOP). Though the seismic image is not available for this study, we inverted the TWOP CSEM data constrained by seismic horizons. The resistive anomaly is constrained by the horizons well in the vertical resistivity image.

Use of geological features to form the regularization weights for Occam's inversion is just one example of a more general application. If any priori high resolution data set, such as seismic image, is assumed to be structurally correlated with the EM resistivity model, the regularization can be derived from this high resolution information. This regularization can be applied not only to Occam's inversion but also to Gauss-Newton or others inversion methods.

In this chapter the metric tensor field was calculated from a geological image. It can also be constructed from other high resolution information such as a section of seismic velocity. The regularization scheme favors models that follow the seismic structure. But the electrical parameters are not always following the seismic structures. Therefore, the image-guided regularization method should be carefully applied to real data. The structured resistivity model should be interpreted with the structural information. In the future, this method may be tested for 3D EM inversion.

Chapter 6 Conclusion

This thesis investigates the detectability of marine CSEM technique for hydrocarbon offshore exploration. Our contributions on the marine CSEM technique consist of comparison between SBL and TSEM acquisition systems, coherence-based irregular sparse mesh, and image-guided regularized inversion of marine EM data.

Comparing the SBL system and the TSEM system by the sensitivity and resolution analysis, we have studied the dependency of sensitivity and resolution on frequency, offset, water depth, target dimensions and reservoir burial depth by the simulation using MARE2DEM code.

In this thesis, we define the shallow water depth ≤ 300 m, intermediate water depth between 300 and 700 m, and deep water depth ≥ 700 m. In shallow water depth of 300 m both data acquisition systems are useful for marine CSEM shallow hydrocarbon exploration. In shallow water environment, the TSEM system gives good and qualified responses in terms of sensitivity and inversion as the SBL system does. In the deep water environment, the SBL system has an advantage in exploration due to lower EM energy lost during propagating through the sea water.

On the depth resolution, the resistivity images from CSEM inversion illustrate the relationship between the resolution and the water depth. Both the SBL and TSEM systems have goode resolution of CSEM inversion in shallow water. But at the deep water envoirnment, the depth resolution of the SBL system is superior to the TSEM system.

On the horizontal resolution, the TSEM system has an advantage. The TSEM system provides a clear resistivity image even though the revervoir length is 1 km. It also distinguish two shallow reservoirs by Occam's inversion when the distance between the two reservoirs are 1 km.

We define a criterion for evaluation of CSEM inversion results. We defined an ATR ratio to analyze the resistive image from marine CSEM data inversion. The detectability of the CSEM data acquisition systems varies with water depth and burial depth of the target. Based on these results, the SBL system is preferred in deep water environment, while the TSEM system is better in the shallow water case.

In order to reduce the computational cost of CSEM inversion, we developed a seismic coherence-based irregular sparse mesh. This irregular sparse mesh reduced the computational cost and physical memory by using fewer parameters. The nodes of this mesh are extracted from seismic coherence and follow the geophysical features.

In this thesis, we have developed a simple method for combining structure constraints into EM inversion by using image-guided regularization weights. The image-guided regularization scheme uses the seismic coherence to provide the model smooth direction. This regularization is tested on 2D inline synthetic marine CSEM and MT data to demonstrate how the results fit the geological structures. The regularizing assumption is that the resistivity parameters have a similar structure to the geological features or seismic image. The resistive anomalies are not across the interfaces, and the amplitude of the anomaly is closer to the true model than the traditional regularized inversion. In this way, the resistivity image from image-guided regularized image is valuable for interpretation.

We have also applied the image-guided regularization method on the marine CSEM Troll area field data set. Even though we inverted the TWOP CSEM data constrained by seismic horizons, the image-guided regularization works well on the CSEM inversion. The resistive anomaly is constrained by the horizons well in the vertical resistivity image.

There are still some limitations in this thesis. First of all, the studies on the sensitivity and resolution of two data acquisition systems are based on the assumption of isotropic environment. Secondly, the IC sparse mesh is only tested in 2D isotropic model. Finally, the image-guided regularization is not tested in real data with the seismic image.

In the future, we shall study the sensitivity and resolution of two system in 3D and anisotropic environment. The IC sparse mesh and image-guided regularization method will be tested on the marine CSEM field data with seismic image.

Our analysis and the results can be used to identify experimental limiting factors and to guide the acquisition method selection for hydrocarbon exploration. We believe that the comparison of data acquisition systems is useful for designing or interpreting a marine EM survey. The coherence-based irregular sparse mesh reduces the computational

cost whereas keep a fine resolution. The image-guided regularization method improve the resolution of resistivity image following the geological stucture.

These studies are useful for the geologists and geophysicists to design or interpret a marine EM survey for hydrocarbon exploration.

BIBLIOGRAPHY

Abubakar, A., T. M. Habashy, V. L. Druskin, L. Knizhnerman, and D. Alumbaugh, 2008. 2.5 D forward and inverse modeling for interpreting low-frequency electromagnetic measurements, *Geophysics*, **73(**4), F165-F177.

Amaya. M, Morten. JP, and Boman.L, 2014. Efficient computation of approximate low-rank hessian for 3D CSEM inversion*, 2014 SEG Annual Meeting*, 722-726.

Amundsen, L., L. Løseth, R. Mittet, S. Ellingsrud, and B. Ursin, 2006. Decomposition of electromagnetic fields into upgoing and downgoing components, *Geophysics*, **71**(5), G211–G223.

Anderson, C., and J. Mattsson, 2010. An integrated approach to marine electromagnetic surveying using a towed streamer and source, *Frist Break*, **28**(5), 71-75.

Ando. S, 2000. Image field categorization and edge/corner detection from gradient covariance, Pattern Analysis and Machine Intelligence, *IEEE Transactions on*, **22**(2), 179-190.

Arato, A., A. Godio, and L. Sambuelli, 2014. Staggered grid inversion of cross hole 2-D resistivity tomography, *Journal of Applied Geophysics*, **107**(60-70).

Baba, K., 2005. Electrical structure in marine tectonic settings, *Surveys in Geophysics*, **26**(6), 701-731.

Baghaie, A. and Yu, Z., 2015. Structure tensor based image interpolation method. *AEU-International Journal of Electronics and Communications*, **69**(2), pp.515-522.

Bahorich. M and Farmer. S, 1995. 3-D seismic discontinuity for faults and stratigraphic features: The coherence cube, *The leading edge*, **14**(10), 1053-1058.

Baltar, D. and Roth, F., 2013. Reserves estimation methods for prospect evaluation with 3D CSEM data, *First Break*, **31**(6), 103-111.

Bannister, P. R., 1968. Determination of the electrical conductivity of the sea bed in shallow waters, *Geophysics*, **33** (6), 995-1003.

Brevik, I., P. T. Gabrielsen, and J. P. Morten, 2009. The role of EM rock physics and seismic data in integrated 3D CSEM data analysis, *SEG Technical Program Expanded Abstracts*, **28**, 835–839; doi: 10.1190/1.3255881. 48

Brown, V., K. Key and S. Singh, 2012. Seismically regularized controlled-source electromagnetic inversion, *Geophysics,* **77**(1), P. E57-E65. Doi: 10.1190/GEO2011-0081.1.

Böhm, G., Galuppo, P., Vesnaver, A., 2000. 3D adaptive tomography using Delaunay triangles and Voronoi polygons, *Geophysical Prospecting*. **48**, 723-744.

Cagniard L., 1953. Basic theory of the magnetotelluric method of geophysical prospecting, *Geophysics,* **18**, 605–635.

Chave, A. D., 2009. On the electromagnetic fields produced by marine frequency domain controlled sources, *Geophysical Journal International*, **179** (3), 1429-1457.

Chen, J. and D. L. Alumbaugh. 2011. Three methods for mitigating airwaves in shallow water marine controlled-source electromagnetic data, *Geophysics*, **76**, no. 2, F89–F99.

Commer, M. and Newman, G.A., 2008. New advances in three-dimensional controlled-source electromagnetic inversion, *Geophysical Journal International*, **172**(2), 513-535.

Constable, S. C., 1990. Marine electromagnetic induction studies, *Surveys in Geophysics*, **11**, no. 2–3, 303–327, doi: 10.1007/BF01901663.

Constable. S, 2010. Ten years of marine CSEM for hydrocarbon exploration, *Geophysics*, **75**(5), 75A67-75A81.

Constable, S., and C. S. Cox, 1996. Marine controlled source electromagnetic sounding 2: The PEGASUS experiment, *Journal of Geophysical Research*, **101**, B3 5519–5530, doi: 10.1029/95JB03738.

Constable, S., A.Orange, G. M. Hoversten, and H. F. Morrison, 1998. Marine magnetotellurics for petroleum exploration: Part 1 —A sea-floor equipment system, *Geophysics*, **63**, 816–825, doi: 10.1190/1.1444393.

Constable, S. C., R. L. Parker, and C. G. Constable, 1987. Occam's inversion — a practical algorithm for generating smooth models from electromagnetic sounding data, *Geophysics*, **52**, 289–300.

Constable, S. and Srnka, L. J. 2007. An introduction to marine controlled-source electromagnetic methods for hydrocarbon exploration, *Geophysics*, **72**(2), WA3-WA12.

da Silva, NV., Morgan, J., Warner, M., Umpleby, A., Ivan Stekl, I., 2012. 3D constrained inversion of CSEM data with acoustic velocity using full waveform inversion, *SEG expanded abstracts*.

de Groot-Hedlin, C, Constable S, 2004. Inversion of magnetotelluric data for 2D structure with sharp resistivity contrasts, *Geophysics*, **69**, 78-86, Doi: 10.1190/1.1649377.

Edwards, N., 2005. Marine controlled source electromagnetics: principles, methodologies, future commercial applications, *Surveys in Geophysics*, **26**(6), 675-700.

Eidesmo. T, S. Ellingsrud, S. E. Johansen, and R. Mittet, 2005. Seabed logging heads advances in long-offset electromagnetic surveying, *Oil and Gas Journal*, **103(**41), 34-41.

Eidesmo. T, S. Ellingsrud, L. M. MacGregor, S. Constable, M. C. Sinha, H. Westerdahl, and F. N. Kong, 2002. Remote detection of hydrocarbon filled layers using marine controlled source electromagnetic sounding, in *paper submitted to EAGE 64th Conference and Exhibition, Florence, Italy, 2002*.

Eidesmo, T., S. Ellingsrud, L. MacGregor, S. Constable, M. Sinha, S. Johansen, F. Kong, and H. Westerdahl, 2002. Sea bed logging (SBL), a new method for remote and direct identification of hydrocarbon filled layers in deep water areas, *First Break*, **20**, 144-152.

Ellingsrud. S, T. Eidesmo, S. Johansen, M. C. Sinha, L. M. MacGregor, and S. Constable, 2002. Remote sensing of hydrocarbon layers by seabed logging (SBL): Results from a cruise offshore Angola, *The Leading Edge*, **21(**10), 972-982.

Fehmers, G.C., C.F.W. Höcker, 2003. Fast structural interpretations with structure-oriented filtering, *Geophysics*, **68**, 1286-1293.

Folke, E., J. Mattsson, and J. Linfoot, 2012. Efficient marine CSEM with a towed acquisition system, *Extended Abstract, 21st EM Induction Workshop. Darwin, Australia, July 25-31, 2012*.

Gabrielsen, P.T., Brevik, I., Mittet, R. and Løseth, L.O., 2009. Investigating the exploration potential for 3D CSEM using a calibration survey over the Troll Field, *First Break*, **27**, 67-75.

Gallardo, L., and M. Meju, 2003. Characterization of heterogeneous near-surface materials by joint 2D inversion of DC resistivity and seismic data, *Geophysical Research Letters*, **30**, 1658, doi: 10.1029/2003GL017370.

Grayver A. V., R. Streich and O. Ritter, 2013. Three-dimensional parallel distributed inversion of CSEM data using a direct forward solver, *Geophysical Journal International,* **193**, 1432-1446.

Gribenko, A. and Zhdanov, M., 2007. Rigorous 3D inversion of marine CSEM data based on the integral equation method, *Geophysics*, **72**(2), WA73-WA84.

Guo, Z., and H. Dong, 2015. Seismic Coherence Driven Sparse Mesh for CSEM Inversion, *8th Congress of the Balkan Geophysical Society*, DOI: 10.3997/2214-4609.201414204.

Guo, Z., Dong, H. and Kristensen, Å., 2016. Sparse CSEM inversion driven by seismic coherence, *Journal of Geophysics and Engineering*, **13**(6), 858-867.

Hale, D. 2009a. Image-guided blended neighbor interpolation, *CWP Report*, **634**(634).

Hale, D. 2009b. Structure-oriented smoothing and semblance, *CWP Report*, **635**(635).

Hansen, K.R. and Mittet, R., 2009. Incorporating seismic horizons in inversion of CSEM data, *In 2009 SEG Annual Meeting. Society of Exploration Geophysicists*.

Harris. C and Stephens. M, 1988. A combined corner and edge detector, *Proceedings of the 4th Alvey Vision Conference*. 147–151.

Holten, T., E. G. Flekkøy, B. Singer, E. M. Blixt, A. Hanssen, and K. J. Måløy, 2009a. Vertical source, vertical receiver, electromagnetic technique for offshore hydrocarbon exploration, *first break*, **27**(5).

Holten, T, E. G. Flekkøy, K. J. Måløy, B. Singer, and others, 2009b. Vertical source and receiver CSEM method in time-domain, *in 2009 SEG Annual Meeting, Society of Exploration Geophysicists.*

Hoversten, G.M., Cassassuce, F., Gasperikova, E., Newman, G.A., Chen, J., Rubin, Y., Hou, Z. and Vasco, D., 2006. Direct reservoir parameter estimation using joint inversion of marine seismic AVA and CSEM data, *Geophysics*, **71**(3), pp.C1-C13.

Hu, W., Abubakar, A. and Habashy, T.M., 2009. Joint electromagnetic and seismic inversion using structural constraints, *Geophysics*, **74**(6), pp.R99-R109.

Jean-Louis Chardac, Mario Petricola, Scott Jacobsen and Bob Dennis. In Search of Saturation. 1996. Middle East Well Evaluation Review.

Johansen, S.E, H. E. F. Amundsen, T. R_sten, S. Ellingsrud, T. Eidesmo, and A. H. Bhuiyan, 2005. Subsurface hydrocarbons detected by electromagnetic sounding, *First Break*, **23(**3).

Key. K, 2009. 1D inversion of multicomponent, multi-frequency marine CSEM data: Methodology and synthetic studies for resolving thin resistive layers, *Geophysic*s, **74**(2), F9-F20.

Key, K., 2012a. Marine electromagnetic studies of seafloor resources and tectonics, *Surveys in geophysics*, **33**(1), 135-167.

Key, K., 2012b, Marine EM inversion using unstructured grids: a 2D parallel adaptive finite element algorithm, *SEG Las Vegas 2012 Annual Meeting,* 1-5. Doi: http://dx.doi.org/10.1190/segam2012-1294.1

Key. K and Ovall. J, 2011. A parallel goal-oriented adaptive finite element method for 2.5-D electromagnetic modelling, *Geophysical Journal International*, **186** (1). 137-154.

Key, K., Du, Z., Mattsson, J., McKay, A. and Midgley, J., 2014. Anisotropic 2.5 D inversion of Towed Streamer EM data from three North Sea fields using parallel adaptive finite elements, *In 76th EAGE Conference and Exhibition 2014.*

Köthe, U., 2003. Edge and junction detection with an improved structure tensor. In Pattern Recognition (pp. 25-32). Springer Berlin Heidelberg.

Li. Y and Key. K, 2007. 2D marine controlled-source electromagnetic modeling: Part1_An adaptive finite-element algorithm, *Geophysics*, **72** (2), WA51-WA62.

Linfoot, J., J. Mattsson, D. Price, and others, 2011a. Case Study of a Towed Streamer EM Survey Over the Troll Field, North Sea, in *2011 SEG Annual Meeting, Society of Exploration Geophysicists, 2011*. 594-598.

Linfoot J. P., C. Clarke, J. Mattsson, and D. Price. 2011b. Modeling and analysis of towed EM data – An Example from a North Sea field trial, *Presented at the 73rd Annual International Conference and Exhibition, EAGE.*

Løseth, L.O., 2007. Modelling of controlled source electromagnetic data, PhD Thesis, Norwegian University of Science and Technology.

Ma. Y, Dave. H, Gong. B, and Meng. Z, 2012. Image-guided sparse-model full waveform inversion, *Geophysics,* **77**(4), R189-R198.

Maaø, F., and A. K. Nguyen. 2010. Enhanced subsurface response for marine CSEM surveying, *Geophysics*, **75**(3), A7–A10, doi: 10.1190/1 .3377054.

MacGregor, L. and M. Sinha, 2000. Use of marine controlled-source electromagnetic sounding for sub-basalt exploration, *Geophysical Prospecting*, **48**(6), 1091-1106.

MacGregor, L., and J. Tomlinson, 2014. Marine controlled-source electromagnetic methods in the hydrocarbon industry: A tutorial on method and practice, *Interpretation*, **2**(3), SH13-SH32. doi: 10.1190/INT-2013-0163.1

McOwen R. 1996. *Partial Differential Equations: Methods and Applications*. Prentice-Hall.

Mastrangelo, E., 2005. Overview of US Legislation and Regulations Affecting Offshore Natural Gas and Oil Activity, *Energy Information Administration, Office of Oil and Gas*, HYPERLINK:http://www.eia.gov/pub/oil_gas/natural_gas/feature_articles/2005/offshore/offshore.pdf, September, 2005.

Mattsson. J, Lindqvist. P Juhasz. R, and Erik. B, 2012. Noise reduction annd error analysis for a towed EM system, *SEG Las Vegas 2012 Annual Meeting*. P. 1-5.

Mittet, R., 2010. High-order finite-difference simulations of marine CSEM surveys using a correspondence principle for wave and diffusion fields, Geophysics, **75**(1), F33-F50.

Mittet, R., 2008. Normalized amplitude ratios for frequency-domain CSEM in very shallow water, *First break*, **26**, P47-54;

Mittet, R., and J. P. Morten, 2012. Detection and imaging sensitivity of the marine CSEM method, *Geophysics*, **77**(6), E411-E425.

Mittet, R., and J. P. Morten, 2013. The marine controlled-source electromagnetic method in shallow water, *Geophysics*, **78**(2), P. E67–E77, 11 FIGS.

Mittet. R and Tor Schaug-Pettersen, 2008. Shaping optimal transmitter waveforms for mmarinne CSEM surveys, *Geophysics.* **73**(3), F97-F104.

Michelini, A., 1995. An adaptive-grid formalism for travel-time tomography, *Geophys J. Int.*121, 489-510.

Morten, J.P., Roth, F., Karlsen, S.A., Timko, D., Pacurar, C., Olsen, P.A., Nguyen, A.K. and Gjengedal, J., 2012. Field appraisal and accurate resource estimation from 3D quantitative interpretation of seismic and CSEM data, *The Leading Edge*, **31**, 447-456.

Newman, G.A. and Alumbaugh, D.L., 2000. Three-dimensional magnetotelluric inversion using non-linear conjugate gradients, *Geophysics*. **140**(2), 410–424.

Newman G.A., CommerM. and Carazzone J.J, 2010. Imaging CSEM data in the presence of electrical anisotropy, *Geophysics*, **75**, F51–F61.

Parker, R.L., 1980. The inverse problem of electromagnetic induction: existence and construction of solutions based on incomplete data, *Journal of Geophysical Research, Solid Earth* (1978-2012), **85**(B8), 4421-4428.

Parker, R.L., Geophysical inverse theory. Princeton university press, 1994.

Plessix, R. E., M. Darnet, and W. A. Mulder, 2007. An approach for 3D multi-source, multi-frequency CSEM modelling, *Geophysics*, **72(**5), SM177-SM184.

Ray, A. and Key, K., 2012. Bayesian inversion of marine CSEM data with a trans-dimensional self-parametrizing algorithm, *Geophysical Journal International*, **191**, 1135-1151.

Ray, A., Key, K., Bodin, T., Myer, D. and Constable, S., 2014. Bayesian inversion of marine CSEM data from the Scarborough gas field using a transdimensional 2-D parametrization, *Geophysical Journal International*, **199**, 1847-1860.

Rodi W. And R. L. Mackie, 2001. Nonlinear conjugate gradients algorithm for 2-D magnetotelluric inversion, *Geophysics*, **66**(1), 174-187.

Shantsev. D. V, Roth. F, amd Ramsfjell.H., 2012. Surface towing versus deep towing in marine CSEM, *SEG Technical Program Expanded Abstracts 2012*: pp. 1-5.

Shantsev, D. V., F. Roth, C. Twarz, A.Frisvoll, and A. Nguyen, 2010. Shallow water CSEM using a surface-towed source, *72nd Annual International Conference and Exhibition, EAGE, Extended Abstracts*, C018.

Shewchuk, J. R., 1996. Triangle: Engineering a 2D quality mesh generator and Delaunay triangulator: Applied Computational Geometry, *Towards Geometric Engineering*, **1148**, 203–222.

Shewchuk. J. R, 2002. What Is a Good Linear Element? Interpolation, Conditioning, and Quality Measures, Eleventh International Meshing Roundtable (Ithaca, New York), pages 115–126, Sandia National Laboratories, September 2002.

Tchon. K, Dompierre. J, Vallet. M, Guibault. F, and Camarero. R, 2006. Two-dimensional metric tensor visualization using pseudo-meshes, *Engineering with Computers*, **22**(2), 121-131.

Tikhnov AN., 1950. The determination of the electrical properties of deep layers of the earth's crust, *Dokl Acad Nauk SSR*, **73**, 295–297.

Tikhonov, A. N., and Arsenin, V. Y. Solutions of Ill-Posed Problems. Wiley, 1977.

Weiss, C. J., and S. Constable, 2006. Mapping thin resistors and hydrocarbon with marine EM methods: Insights from 1D modelling, *Geophysics,* **71**(2), G43-G51.

Wiik, T., Nordskag, J.I., Dischler, E.Ø. and Nguyen, A.K., 2015. Inversion of inline and broadside marine controlled - source electromagnetic data with constraints derived from seismic data. *Geophysical Prospecting*, **63**(6), 371-1382.

Zach. J.J, and Frenkel. M.A, 2009. 3D inversion-based interpretation of marine CSEM data, *Offshore Technology Conference,* OTC 20289, 1-13.

Zhdanov, M. S, 2012. The first practical 3D inversion of towed streamer EM data from the Troll field trial. *SEG Las Vegas 2012 Annual Meeting.*

Zhdanov, M. S., Geophysical inverse theory and regularization problems, **36**. Elsevier, 2002.

Zhdanov, M.S., Gribenko, A. and Cuma, M., 2007. January. Regularized focusing inversion of marine CSEM data using minimum vertical support stabilizer, *In 2007 SEG Annual Meeting, Society of Exploration Geophysicists.*

Zhou, J., Revil, A., Karaoulis, M., Hale, D., 2014a. Image-guided inversion of electrical resistivity data, *84th Annual International Meeting, SEG, Expanded Abstract*, 2148-2152, doi: 10.1190/segam2014-1662.1

Zhou, J., Revil, A., Karaoulis, M., Hale, D., Doetsch, J. and Cuttler, S., 2014b. Image-guided inversion of electrical resistivity data, *Geophysical Journal International*, **197**, 292-309.

Zhou, J., Revil, A. and Jardani, A., 2016. Stochastic structure-constrained image-guided inversion of geophysical data, *Geophysics*, **81**, E89-E101.

Ziolkowski, A., R. Parr, D. Wright, V. Nockles, C. Limond, E. Morris, and J. Linfoot, 2010. Multi-transient electromagnetic repeatability experiment over the North Sea Harding field, *Geophysical Prospecting*, **58**(6), 1159-1176.

Zonge, K.L., and Hughes L.J., 1991. Controlled source audio frequency magnetotellurics. In Nabighian, M.N. (ed.), *Electromagnetic Methods in Applied Geophysics.* Tulsa, OK: Society of Exploration Geophysicists, 713-810.

Appendix: Publications during PhD study

1. Guo, Z. (Norwegian University of Science and Technology, Norway); Hu, X.; Dong, H. 2013. Model based interpolation for magnetic field anomaly analysis. *75th European Association of Geoscientists and Engineers Conference and Exhibition, EAGE Expanded Abstracts*, p 3129-3133, DOI: 10.3997/2214-4609.20130957.
2. Guo, Z. and Dong, H., 2015. Seismic Coherence Driven Sparse Mesh for CSEM Inversion. *8th Congress of Balkan Geophysical Society in Chania, Crete, Greece, 4-8 October 2015. Expanded Abstracts.* DOI: 10.3997/2214-4609.201414204.
3. Guo, Z., Dong, H. and Kristensen, Å., 2015. Compared detectable limitations of hydrocarbon exploration by different marine CSEM methods in shallow water. *In 14th EAGE International Conference on Geoinformatics-Theoretical and Applied Aspects. Expanded Abstracts,* 36-40. DOI: 10.3997/2214-4609.201412425.
4. Guo, Z., Dong, H. and Kristensen, Å., 2015. Comparison of marine CSEM data acquisition system by Occam inversion: analysis the effect of water depth, *The 6th International Geosciences Student Conference (IGSC), Expanded Abstracts*.
5. Guo, Z.W., Dong, H.F. and Xiao, J.P., 2015. Detection of Permafrost Subgrade Using GPR: A Case Examination on Qinghai-Tibet Plateau. *Journal of Geoscience and Environment Protection*, **3**, 35-47.
6. Guo, Z., Dong, H. and Kristensen, Å., 2016. Image-guided Regularized Marine Controlled Source Electromagnetic Inversion: *78th EAGE Conference and Technical Exhibition, EAGE Expanded Abstracts.* DOI: 10.3997/2214-4609.201600943.
7. Guo, Z., Dong, H, and Liu, J., 2016. Comparison of marine CSEM data acquisition system by Reservoir Sensitivity Index: analysis the effect of water depth: *ACTA Oceanologica sinica*, **35**(11).
8. Guo, Z., Dong, H. and Kristensen, Å. 2016. Image-guided regularization of marine electromagnetic inversion, *Geophysics*, Accepted.
9. Guo, Z., Dong, H. and Kristensen, Å. 2016. Sparse CSEM inversion driven by seismic coherence, *Journal of Geophysics and Engineering*, **13**(6), 858-867.
10. Guo, Z., Dong, H. and Kristensen, Å. 2016. . Comparison of two Marine CSEM data acquisition systems in offshore hydrocarbon explorations, *Geophysical Prospecting*, Submitted.

11. Liu, J., Guo, Z., X., Tong, and Q., Liu, 2011. Application of the Ground High-Precision Magnetic Method to Magnetite Survey in the Hami Area, Xinjiang, (in Chinese) *Geology and prospecting*, **47**(3), 432-438.